

©[2009]

Young Jai Choi

ALL RIGHTS RESERVED

Multiferroicity and Magnetoelectric Effect in Novel Complex Oxides

by

Young Jai Choi

A Dissertation submitted to the
Graduate School-New Brunswick
Rutgers, The State University of New Jersey
in partial fulfillment of the requirements

for the degree of

Doctor of Philosophy

Graduate Program in Physics

written under the direction of

Professor Sang-Wook Cheong

and approved by

New Brunswick, New Jersey

May, 2009

Abstract of the Dissertation

Multiferroicity and Magnetoelectric Effect in Novel Complex Oxides

by

Young Jai Choi

Dissertation Director:

Sang-Wook Cheong

Multiferroic materials, in which ferroelectric and magnetic ordering are simultaneously present, exhibit unprecedented physical properties due to the coupling between electric and magnetic order parameters. The significant cross-coupling effects in the newly found materials have invigorated research in multiferroics as they offer a new route toward fundamental understanding of how spin and lattice degrees of freedom interact and produce macroscopic phenomena. Furthermore, the emergence of multiple functional properties in such materials has stimulated the application in future generations of novel devices in which polarization can be controlled by a magnetic field or vice versa. Recently, the search for an enhanced coupling between dual order parameters has led to discoveries of new class of materials called magnetism-driven ferroelectrics. In such materials, ferroelectricity is induced by a fundamental new mechanism, by which magnetic orders with broken inversion symmetry result in ferroelectric distortions through exchange striction. The magnetic origin of their ferroelectricity engenders highly sensible ferroelectric properties to applied magnetic fields. Herein, we present discoveries of new multiferroics which reveal intriguing interplays between ferroelectricity and magnetism: (1) Thermal and magnetic reversal of electric polarization in the conical spiral multiferroic,

CoCr_2O_4 , (2) Collinear-magnetism-induced ferroelectricity of the Ising chain magnet $\text{Ca}_3\text{CoMnO}_6$, and (3) Multiferroicity in the square-lattice antiferromagnet of $\text{Ba}_2\text{CoGe}_2\text{O}_7$. The rich physical phenomena among these new materials unveil a fascinating nature of multiferroicity.

Acknowledgements

“ Your word is a lamp to my feet and a light for my path.”

(Psalm 119:105)

First of all, I confess that by the grace of God I can stand here and he always leads me with enormous goodness and mercy. I would like to express my sincere gratitude to my adviser Professor Sang-Wook Cheong for his care and guidance during my research work. His passion for physics has invigorated me into enjoying my research and it has been a great pleasure to work in one of the most productive and enthusiastic groups. I express special thanks to my committee members for their helpful comments and advice which have stimulated my work: Valery Kiryukhin, Emil Yuzbashian, Tao Zhou, and Douglas Bergman. My appreciation also goes to Professor Weida Wu and Seongshik Oh for useful discussions. I also would like to thank my current and former group members for their substantial support and assistance, making my research successful. These special thanks go to Soonyong Park, Hee Taek Yi, Taekjib Choi, Seongsu Lee, Yoichi Horibe, Zhen Qin, Steven Rodan for providing much needed breaks on the more stressful days, and valuable insights for my work. And to Toshihiro Asada, Chenglin Zhang, Sunmog Yeo, Sungbaek Kim, Han-Jin Noh, and Namjung Hur for giving me generous advice whenever I needed. I am also grateful to our undergraduate students who are enthusiastic for research: Daniel Kwok, Andrew Hogan, Sean Fackler, Matthew Vannucci, and Abdullah Sandhu. I want to acknowledge Professor Thomas A. Kaplan in Michigan state university for his theoretical support in CoCr_2O_4 work. I owe him for his significant contribution for Chapter II, and Appendices I - III.

Finally, I give special gratefulness to my parents and parents-in-law who always pray for me with great love and also show appreciation to my sister and sister-in-law for their caring. And most of all, my sincerest gratitude towards my wonderful, loving wife, Nara Lee, who provides me with the love and support of a family member, and valuable insights as a fellow colleague. This thesis would not have been possible without her by my side every step of the way.

Table of Contents

Abstract of the Dissertation.....	ii
Acknowledgements.....	iv
I. Introduction to Recent Progress in Multiferroics.....	1
1. Multiferroics.....	2
2. Proper and Improper Ferroelectrics.....	4
3. Spiral-magnetism-induced Ferroelectricity.....	9
4. Collinear-magnetism-induced Ferroelectricity.....	17
5. REFERENCES.....	23
II. Thermally or Magnetically Induced Polarization Reversal in the Multiferroic CoCr ₂ O ₄	25
1. Introduction.....	26
2. Experimental Method.....	29
3. Result and Discussion.....	30
4. REFERENCES.....	50
III. Ferroelectricity in an Ising Chain Magnet.....	52
1. Introduction.....	53
2. Experimental Method.....	56
3. Result and Discussion.....	58
4. REFERENCES.....	71
IV. Multiferroicity in the square-lattice antiferromagnet of Ba ₂ CoGe ₂ O ₇	73
1. Introduction.....	74

2. Experimental Method.....	76
3. Result and Discussion.....	76
4. REFERENCES.....	84
V. Conclusion.....	86
1. Summary.....	87
2. A New Dimension of Multiferroics Research.....	88
3. REFERENCES.....	96
Appendix I : Spin Rotation and Domain Walls.....	97
Appendix II : Magnetic X-ray Scattering from Complex Spin Structures.....	104
Appendix III : Handedness vs. Chirality.....	107
Appendix IV : Ferroelectricity in an $S=1/2$ Chain Cuprate (<i>Phys. Rev. Lett.</i> ,2007).....	113
Appendix V : Ferroelectricity in an Ising Chain Magnet (<i>Phys. Rev. Lett.</i> ,2008)....	117
Appendix VI : Multiferroicity in the Square-lattice Antiferromagnet of $\text{Ba}_2\text{CoGe}_2\text{O}_7$ (<i>Appl. Phys. Lett.</i> , 2008).....	121
Appendix VII : Thermally or Magnetically Induced Polarization Reversal in the Multiferroic CoCr_2O_4 (<i>Phys. Rev. Lett.</i> , 2009).....	124
Appendix VIII : Switchable Ferroelectric Diode and Photovoltaic Effect in BiFeO_3 (<i>Science</i> , 2009).....	128
Appendix IX : Giant Magnetic Coercivity and Ionic Superlattice Nanodomains in $\text{Fe}_{0.25}\text{TaS}_2$ (Submitted to <i>Europhys. Lett.</i> , 2009).....	132
Curriculum Vitae.....	148

Chapter I

Introduction to Recent Progress in Multiferroics

1. Multiferroics

The ordering of spins comes into play in magnetic materials, and ferroelectricity is the electric version of magnetism, associated with the polar arrangement of charges. Magnetism and ferroelectricity are known to coexist in a special class of materials termed multiferroics [1-6]. Large cross-coupling effects between magnetism and ferroelectricity in multiferroics have been the primary drive of multiferroics research. The search for strongly coupled magnetism and ferroelectricity recently led to a series of discoveries of new materials, called frustrated magnets, such as RMnO_3 , RMn_2O_5 (R: rare earth), $\text{Ni}_3\text{V}_2\text{O}_8$, delafossite CuFeO_2 and ACrO_2 (A=Cu, Ag), MnWO_4 , hexagonal ferrite $(\text{Ba,Sr})_2\text{Zn}_2\text{Fe}_{12}\text{O}_{22}$, spinel CoCr_2O_4 , LiCu_2O_2 , $\text{Ca}_3(\text{Co,Mn})\text{O}_6$, CuO , and FeVO_4 [7-22]. In spite of weak magnetoelectric coupling or small magnitude of electric polarization (two to four orders smaller in magnitude than typical ferroelectrics), such materials are unique in that electric properties are highly sensitive to external magnetic fields. The reason for the susceptible dielectric properties is significantly due to their ferroelectricity, which is originated from complex spin structures in frustrated magnets [23-25]. Recently, high tunability of dielectric properties by applied magnetic fields, such as reversibly flipping ferroelectric polarization [5, 8] (FIG. I. 1(a)) or a drastic change of dielectric constant with applied magnetic fields [5, 10] (FIG. I. 1(b)), has been found in magnetically-driven ferroelectrics where magnetic orders with broken inversion symmetry accompany the occurrence of ferroelectric polarization.

There are two microscopic mechanisms proposed to explain this effect. One involves lattice relaxation through exchange striction in the magnetically ordered states. In cases when ferroelectricity is induced by spiral magnetic order, the ionic

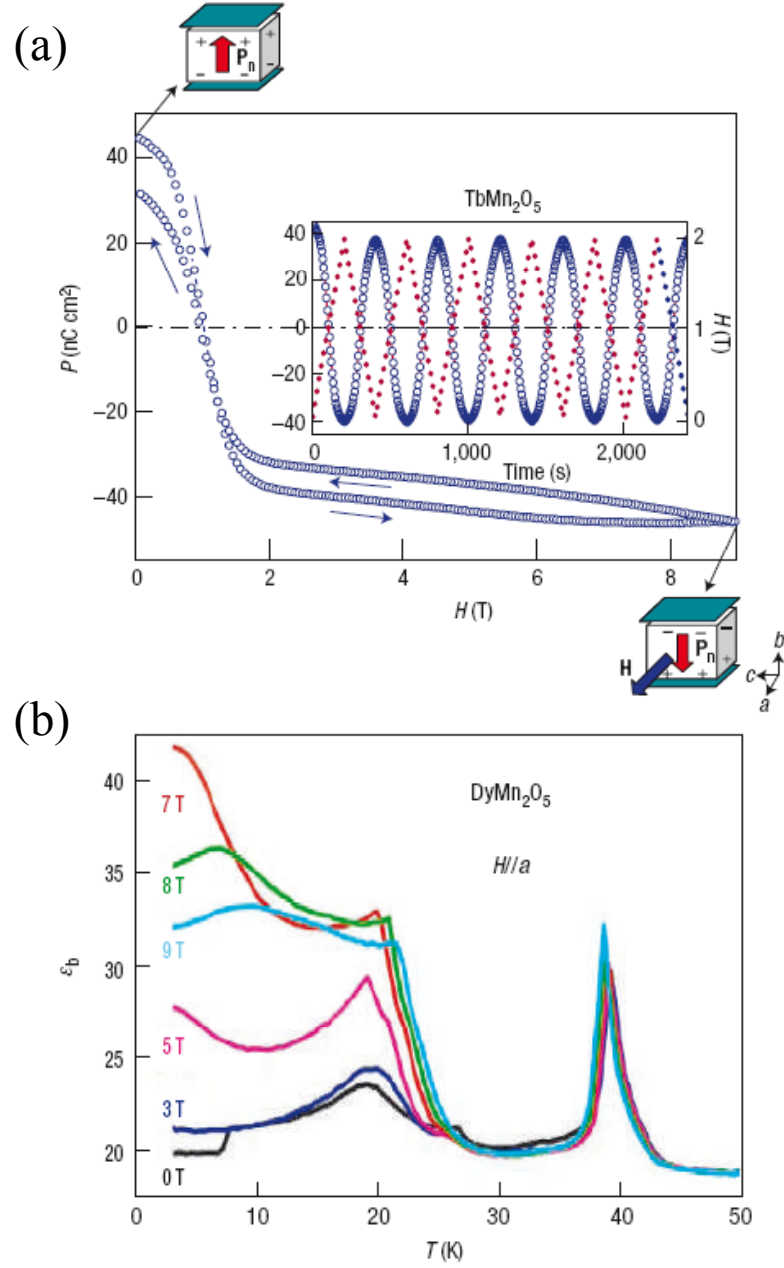


FIG. I. 1. High magnetic tenability of magnetic ferroelectrics (a) Highly reversible polarization switching along the b axis, activated by magnetic fields along the a axis in TbMn_2O_5 . (b) Temperature dependence of dielectric constant along the b axis in DyMn_2O_5 . The step-like increase in dielectric constant below ~ 25 K strongly depends on applied magnetic fields along the a axis. [5, 8, 10]

displacements are due to the antisymmetric exchange known as the Dzyaloshinski-Moriya (DM) interaction, although in some cases, the symmetric exchange is relevant [23]. The other mechanism involves electric charge distortions due to the relative coupling of electrons, with the spin-orbit interaction that occurs without lattice relaxation as the primary driving force [25]. The relative importance of these quite distinct mechanisms remains to be determined.

2. Proper and Improper Ferroelectrics

In proper ferroelectrics, structural instability associated with the change in chemical bonding is a primary driver for ferroelectricity. Such materials have been mostly found in transition metal oxides having perovskite structure, ABO_3 , as shown in FIG. I. 2. The large cations in A sites occupy the corners in the cubic unit cell and the small cation in B site lies at the center of an octahedron formed by oxygen anions. A classic example of ferroelectric perovskite, BaTiO_3 has Ti^{4+} ions in the B site with no electrons in the $3d$ shell, and they tend to form strong covalent bonds with neighboring O^{2-} ions. As a result, the hybridization between the Ti $3d$ states and the oxygen $2p$ states softens the Ti-O repulsion and allows ferroelectric instability [26].

Dissimilar from the ferroelectricity in transition metal oxides where transition ions have empty d shells, magnetism requires transition metal ions with partially filled d shells because the long-range magnetic ordering results from the exchange interaction between the uncompensated magnetic spins of different ions. In spite of the mutual exclusiveness of these two properties, some proper ferroelectrics such as BiMnO_3 or BiFeO_3 contain magnetism arising from Mn^{3+} and Fe^{3+} ions. Ferroelectricity results from

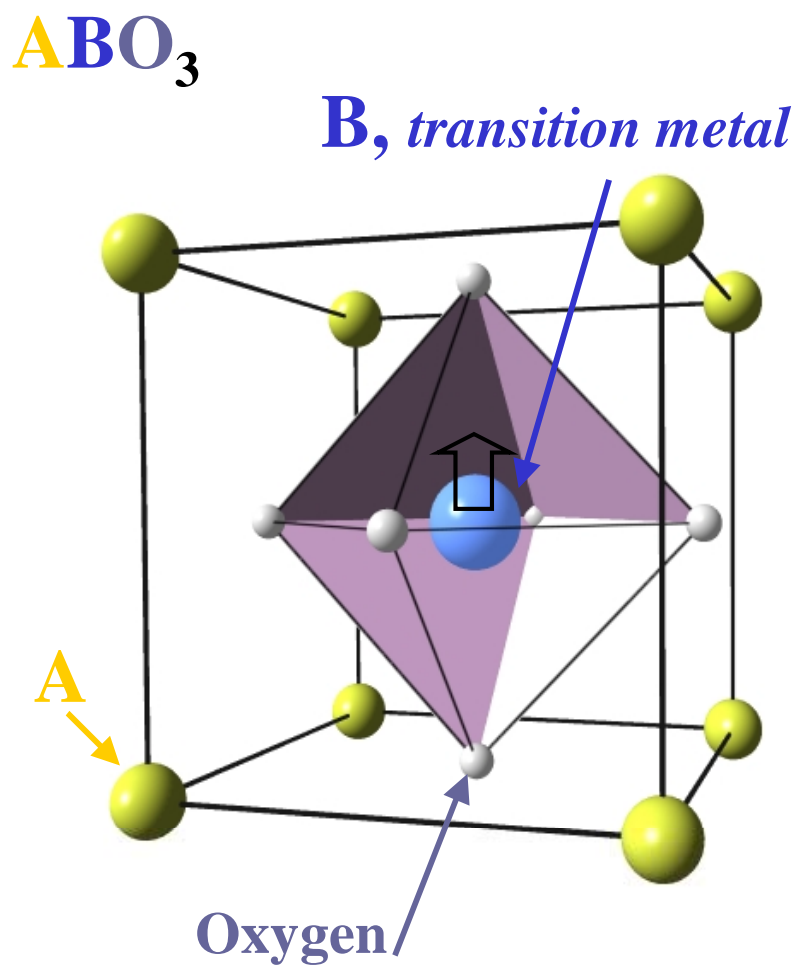


FIG. I. 2. Cubic perovskite ABO_3 structure (high temperature phase): The large cation in A site (yellow balls) occupy the corners in the cubic unit cell. The small cation in B site (a blue ball) lies at the center of an octahedron formed by oxygen anions (silver balls). For BaTiO_3 , the arrow indicates the relative displacement of a Ti ion to O ions when ferroelectric and tetragonal structure transitions occur at 393 K.

off-centered Bi^{3+} ions with two electrons on the 6s orbital, enclosed by neighboring O^{2-} ions [27]. In BiMnO_3 ferroelectricity sets in below ~ 800 K and ferromagnetic spin order appears at ~ 110 K, below which two properties coexist [28]. However, because of different origins for ferroelectricity and ferromagnetism, and large gap in transition temperatures between two properties, the expected cross-coupling effects between them would not be strong although this material shows particularly large magnetization and polarization. For instance, the change in dielectric constant appears insensitive to applied magnetic fields and does not exceed 0.7 % around the magnetic transition in 9 T (FIG. I. 3) [28].

Unlike the proper ferroelectrics discussed so far, in improper ferroelectrics polarization is just a part of a more complex lattice distortion or an accidental by-product of some other ordering [29]. An example is the rare earth hexagonal manganite (RMnO_3 , $\text{R}=\text{Ho-Lu}$ and Y), where the hexagonal structure arises from the smallness of the ionic radii of the rare-earth ions and the presence of covalent Mn-O bonds (note that RMnO_3 with larger R ions such as La-Dy forms into orthorhombic perovskite structure). Recently, it has been confirmed that the ferroelectricity in YMnO_3 results from a buckling of the MnO_5 polyhedra, combined with unusual Y coordination and the triangular and layered MnO_5 network (FIG. I. 4) [30, 31]. Another mechanism towards polar arrangement of charges is to utilize charge ordering in a non-symmetric manner. In many narrow band metals with strong electronic correlations, charge carriers become localized at low temperatures and form periodic superstructures. An example has recently been suggested in manganite $\text{Pr}_{1-x}\text{Ca}_x\text{MnO}_3$ [32]. The possible coexistence of site-centered and bond-centered charge distribution lacks inversion symmetry and leads to a

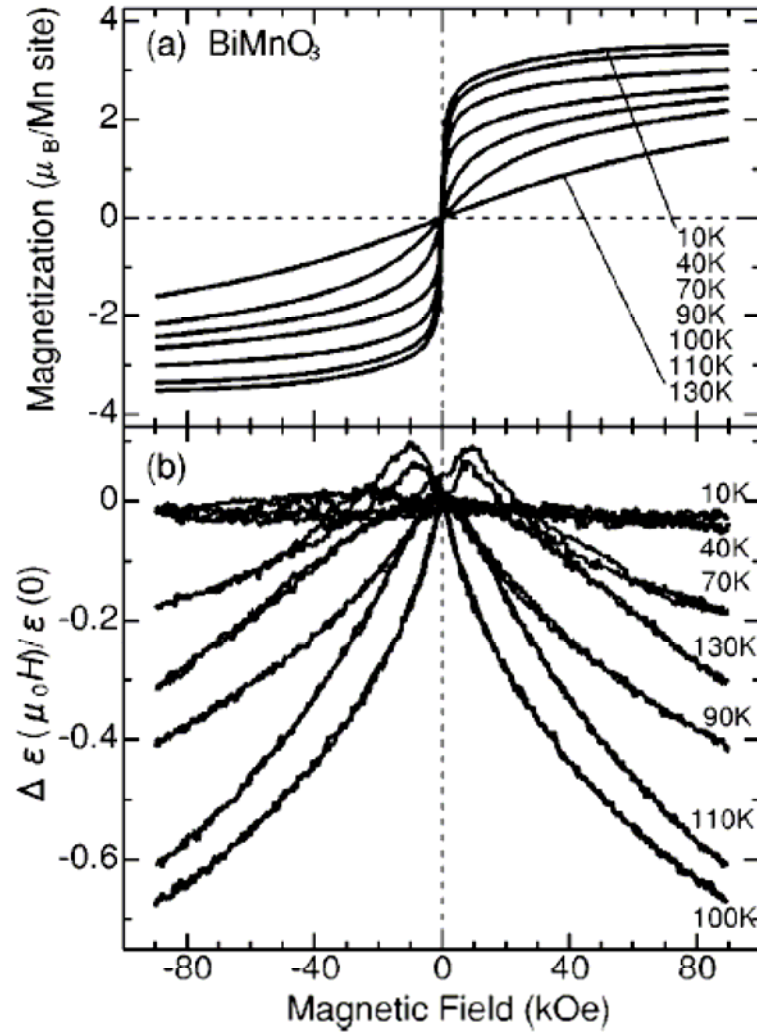


FIG. I. 3. (a) Isothermal magnetization and (b) field-induced change in dielectric constant as a function of a magnetic field at various temperatures of BiMnO_3 [28].

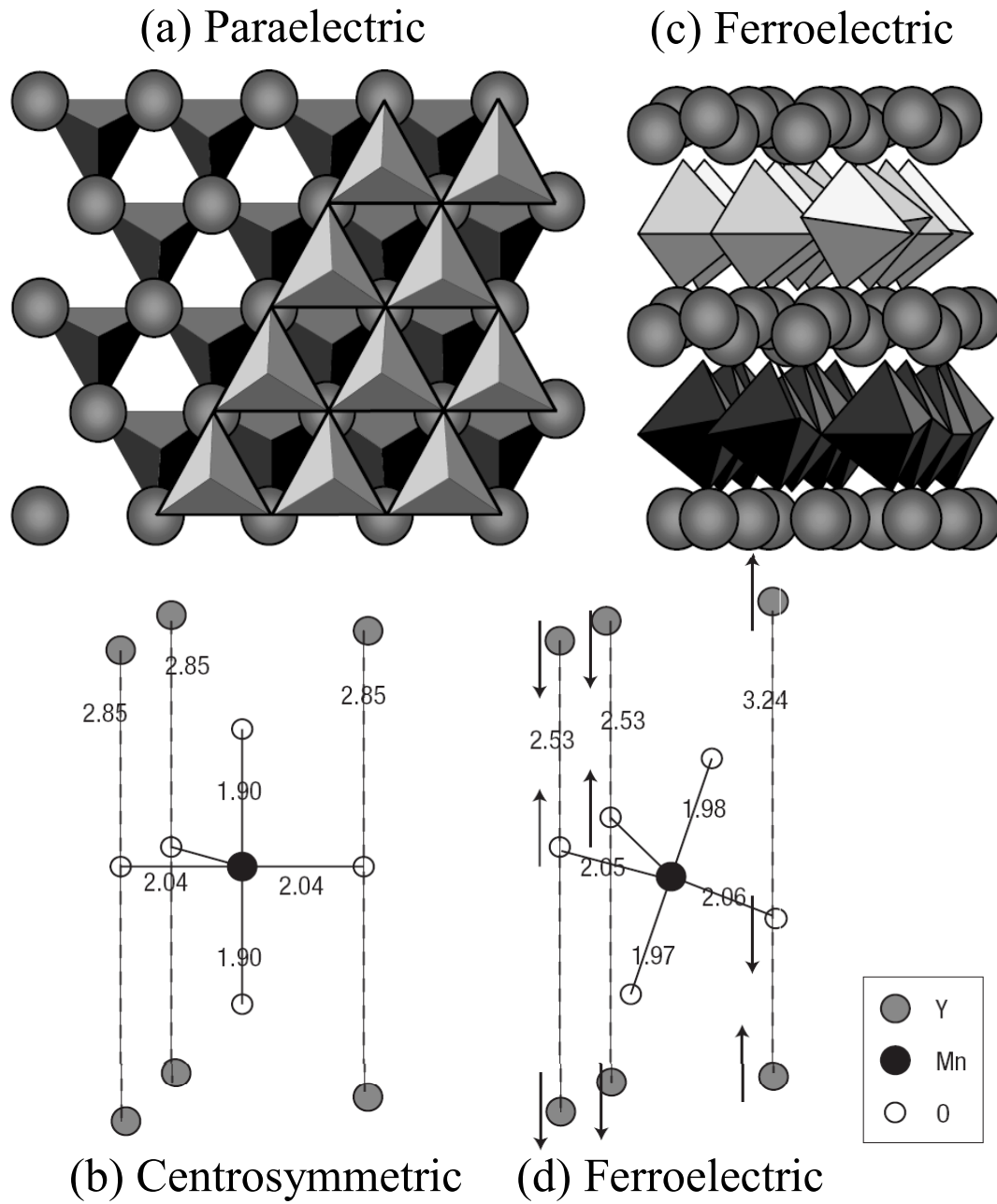


FIG. I. 4. The crystallographic structure of YMnO_3 [30]. (a) Top view of paraelectric phase, showing hexagonal in-plane structure. (b) Calculated atomic positions of the centrosymmetric structure (c) A view of the ferroelectric phase from perpendicular to the c axis, showing the layered nature of YMnO_3 . (d) Ferroelectric structure. The arrows indicate atomic displacements with respect to centrosymmetric structure.

net polarization (FIG. I. 5(a)). It has also been reported that the charge ordering in LuFe_2O_4 , while crystallizing in alternate stacking of triangular lattices with mixed valence of Fe ions, induces electric polarization [33]. The average valence of Fe ions in LuFe_2O_4 is +2.5 and below the charge ordering temperature, ~ 350 K, the layers tend to be arranged with alternating ratios of Fe^{2+} and Fe^{3+} ions (2:1 and 1:2). Thus, the charge transfer from one to the next layer gives rise to net ferroelectric polarization, as depicted in FIG. I. 5(b). The last example is the magnetism-induced ferroelectrics, where competing nature of frustrated magnetic spins results in complex magnetic structures accompanied by broken inversion symmetry, leading to ferroelectric polarization. The details of theoretical understanding and experimental realization for such compounds are discussed in Section 3 and 4.

3. Spiral-Magnetism-induced Ferroelectricity

Theoretical insight into the remarkably observed cross-coupling effects between electric and magnetic properties is based on the symmetries of two different order parameters, i.e. electric polarization and magnetization. Polarization and electric field change their signs on the inversion of all coordinates but remain unchanged on time reversal whereas magnetization and magnetic field are invariant on coordinate inversion and change their signs on time reversal. Due to the different transformation properties, for static \mathbf{P} and \mathbf{M} , nonlinear coupling can only be allowed, resulting from interplay of charge, spin, lattice and orbital degrees of freedom [5, 24]. If the magnetic ordering is inhomogeneous over the crystal, symmetries allow for the third-order term, $\mathbf{PM}\partial\mathbf{M}$, and give magnetically-driven ferroelectric polarization in cubic crystals as the form of

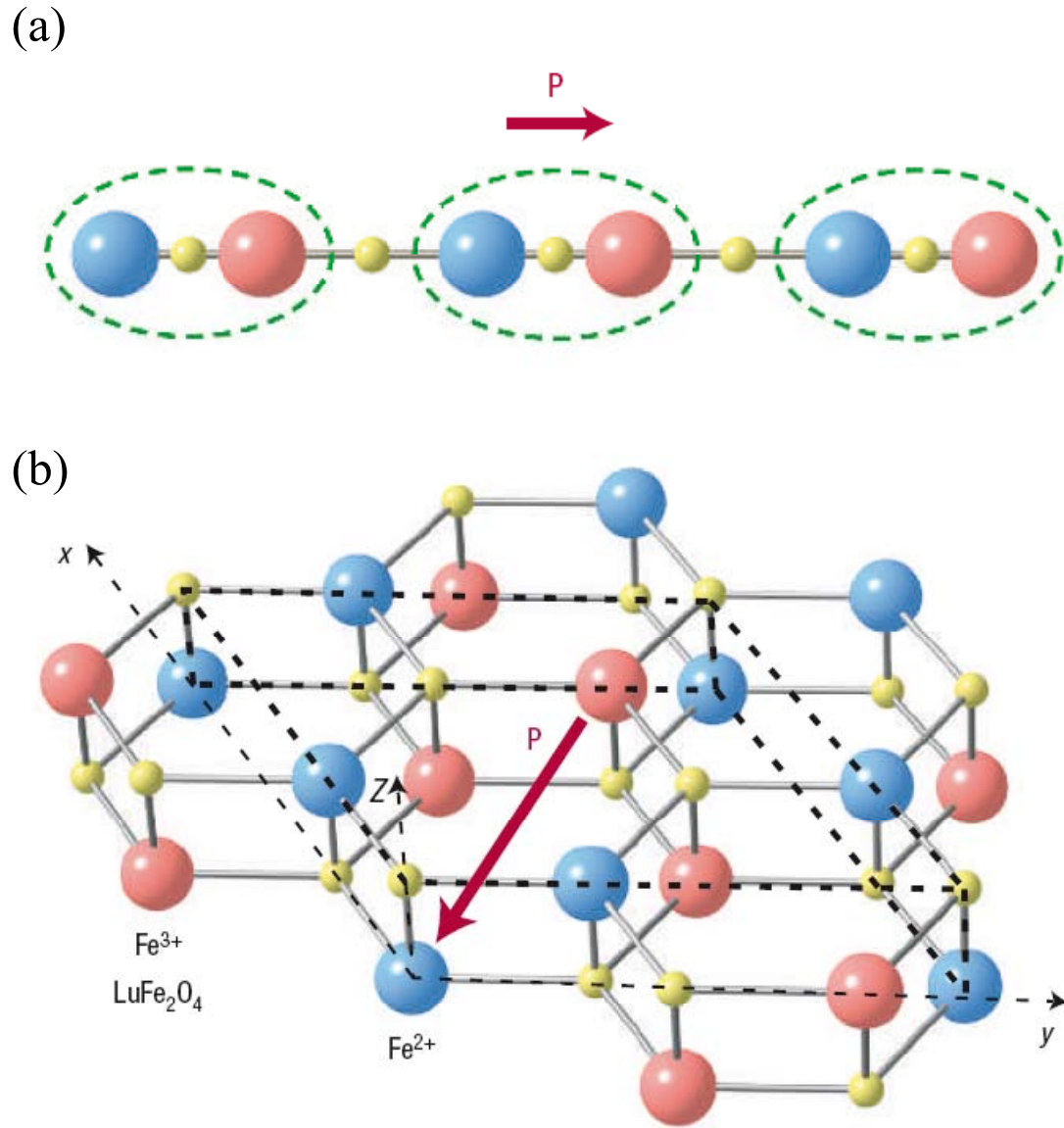


FIG. I. 5. Ferroelectricity in charge-ordered systems [5, 32, 33]. Red/blue balls correspond to cations with more/less positive charges. (a) Ferroelectricity induced by coexistence of site-centered and bond-centered charge orders in a chain. (b) Induced polarization by charge ordering in bilayered LuFe_2O_4 with a triangular lattice of Fe ion in each layer.

$\mathbf{P} \propto [(\mathbf{M} \cdot \partial)\mathbf{M} - \mathbf{M}(\partial \cdot \mathbf{M})]$ [24]. In this induced polarization, spatial variations of magnetic ordering would let frustration come into play. For instance, in a spin chain, the nearest-neighbor ferromagnetic interaction produces uniform spin order along the chain as a ground state. The next-nearest neighbor antiferromagnetic interaction frustrates the spin order and when sufficiently strong, stabilizes a spiral magnetic state, $\mathbf{S}_n = S [\hat{x} \cos(\mathbf{Q} \cdot \mathbf{r}_n) + \hat{y} \sin(\mathbf{Q} \cdot \mathbf{r}_n)]$, where \hat{x} and \hat{y} are orthogonal unit vectors and \mathbf{Q} is the wave vector. Spiral magnetic states are characterized by two vectors; the modulation wave vector \mathbf{Q} and the spin-rotation axis \mathbf{e} (along the \hat{z} axis). The induced electric dipole moment in spiral-magnetic ferroelectrics is orthogonal both to \mathbf{Q} and \mathbf{e} ; $\mathbf{P} \propto \mathbf{e} \times \mathbf{Q}$ [24]. As an intriguing aspect, a spiral magnetic state spontaneously breaks time and inversion symmetries. Thus two spiral states are mutually accessible by space inversion operation as shown in FIG. I. 6 and the sign of polarization is determined by spin rotation direction.

A proposed microscopic mechanism involves lattice relaxation through exchange striction in the magnetically ordered states. In cases when ferroelectricity is induced by spiral magnetic order, the ionic displacements are due to the antisymmetric exchange known as the Dzyaloshinski-Moriya (DM) interaction, $\mathbf{D}_{n,n+1} \cdot \mathbf{S}_n \times \mathbf{S}_{n+1}$ [5, 23]. The Dzyaloshinski vector \mathbf{D} is proportional to the spin-orbit coupling constant and depends on the position of the oxygen ion between two magnetic ions. The DM interaction favors non-collinear spin ordering. FIG. I. 7 depicts oxygen displacement depending on relative spin coupling between two adjacent magnetic ions and induced electric moment. If the alternating sign of spin chirality, i.e. $\text{sign}(\mathbf{S}_n \times \mathbf{S}_{n+1})$, constitutes a chain as seen in FIG. I. 7(c), then weak ferromagnetism can be induced and net polarization does not exist [5, 6]. On the other hand, as shown in FIG. I. 7(a) and (b), with a spiral-type magnetic ordering,

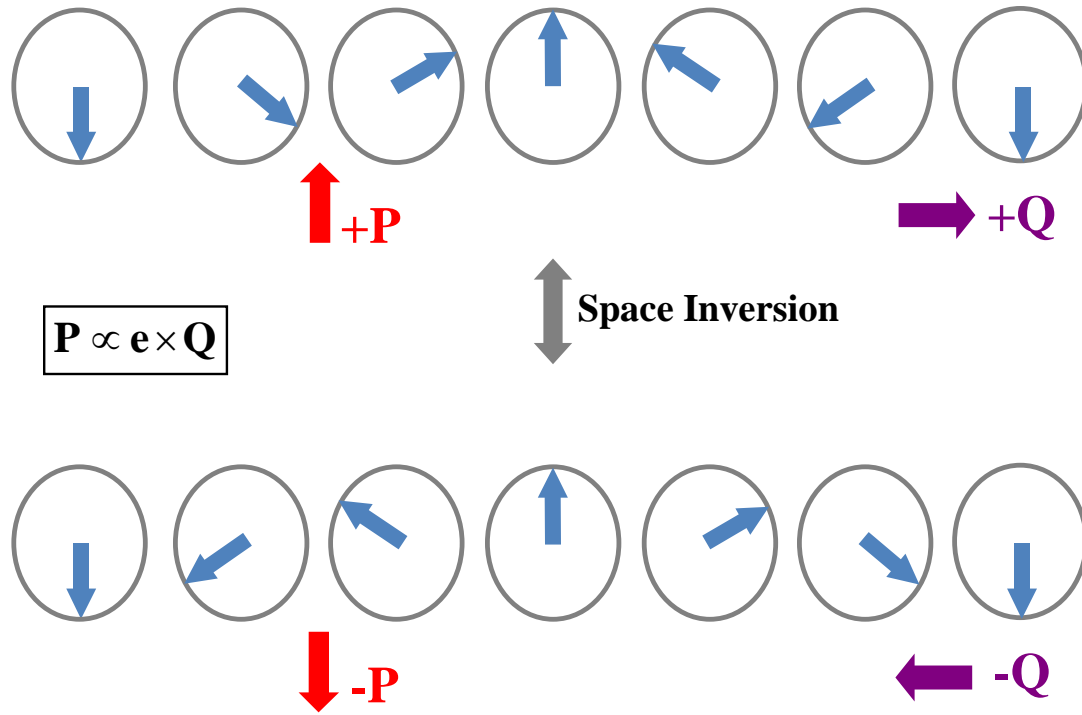


FIG. I. 6. Two domains of spiral structure. They are mutually convertible by space inversion operation. Red and purple arrows denote the spiral wave vector and the direction of induced polarization, respectively.

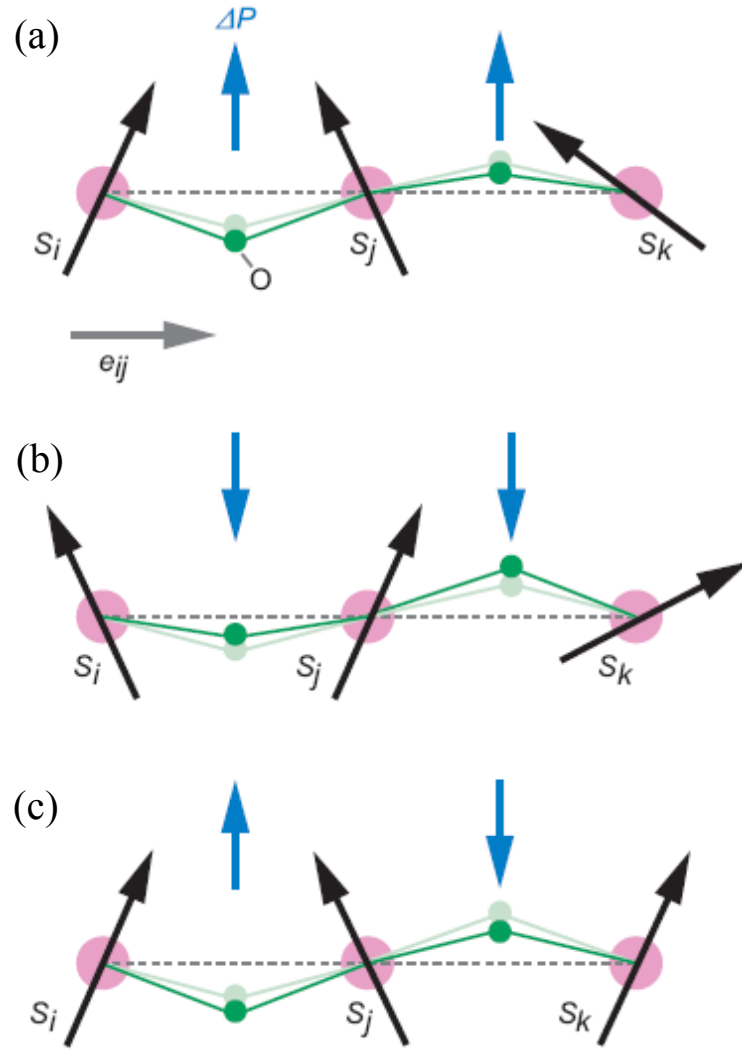


FIG. I. 7. Oxygen displacement, and electric moment depending on the type of noncollinear spin order. (a) Counterclockwise spiral with upward net polarization. (b) Clockwise spiral with downward net polarization. (c) Weak ferromagnetism without net polarization. [6]

the induced local polarizations by the inverse DM effects are unidirectional along the chain, leading to a net polarization perpendicular to the direction of the spin wave vector [5, 23].

The prototypical example of spiral-magnetism-induced ferroelectricity is the orthorhombic perovskite $\text{Eu}_{0.75}\text{Y}_{0.25}\text{MnO}_3$ [34]. $\text{Eu}_{0.75}\text{Y}_{0.25}\text{MnO}_3$ undergoes two successive magnetic transitions at ~ 50 and 30 K corresponding to a collinear sinusoidal antiferromagnetic state and a spiral ferroelectric state, respectively (FIG. I. 8). The anisotropic magnetic susceptibility implies a magnetic spiral with the easy ab plane (i.e. spin rotation vector along the c axis) and a propagation wave vector along the easy b axis below 30 K. As expected from $\mathbf{P} \propto \mathbf{e} \times \mathbf{Q}$, polarization emerges along the a axis (FIG. I. 9(a)). In a strong magnetic field along the a axis, the spiral plane tends to be perpendicular to the magnetic field direction, i.e., spin-flop transition by rotating 90° , resulting in polarization along the c -axis (FIG. I. 9(b)). As shown in FIG. I. 9(c), in 9 T along the a axis, the ab spiral plane is overtaken by the bc plane. Thus polarization along the a axis significantly decreases and polarization along the c axis appears.

Another interesting type of spiral magnet was found in LiCu_2O_2 which reveals intriguing complex spiral structure associated with the quantum quasi-one-dimensional (1D) $S=1/2$ nature of the system. LiCu_2O_2 consists of an equal number of Cu^{1+} and Cu^{2+} ions [18]. The magnetic Cu^{2+} ions carry $S=1/2$ and form 1D $S=1/2$ chains along the b -axis. A typical condition for obtaining a spiral magnetic order is when in a chain magnet the nearest-neighbor ferromagnetic coupling (J_F) competes with the next-nearest-neighbor antiferromagnetic coupling (J_{AF}). In a classical regime, it is well known that when $|J_F/J_{AF}|$ is larger than $1/4$, a spiral order with $2\pi\zeta = \cos^{-1}(1/4|J_F/J_{AF}|)$ (pitching angle

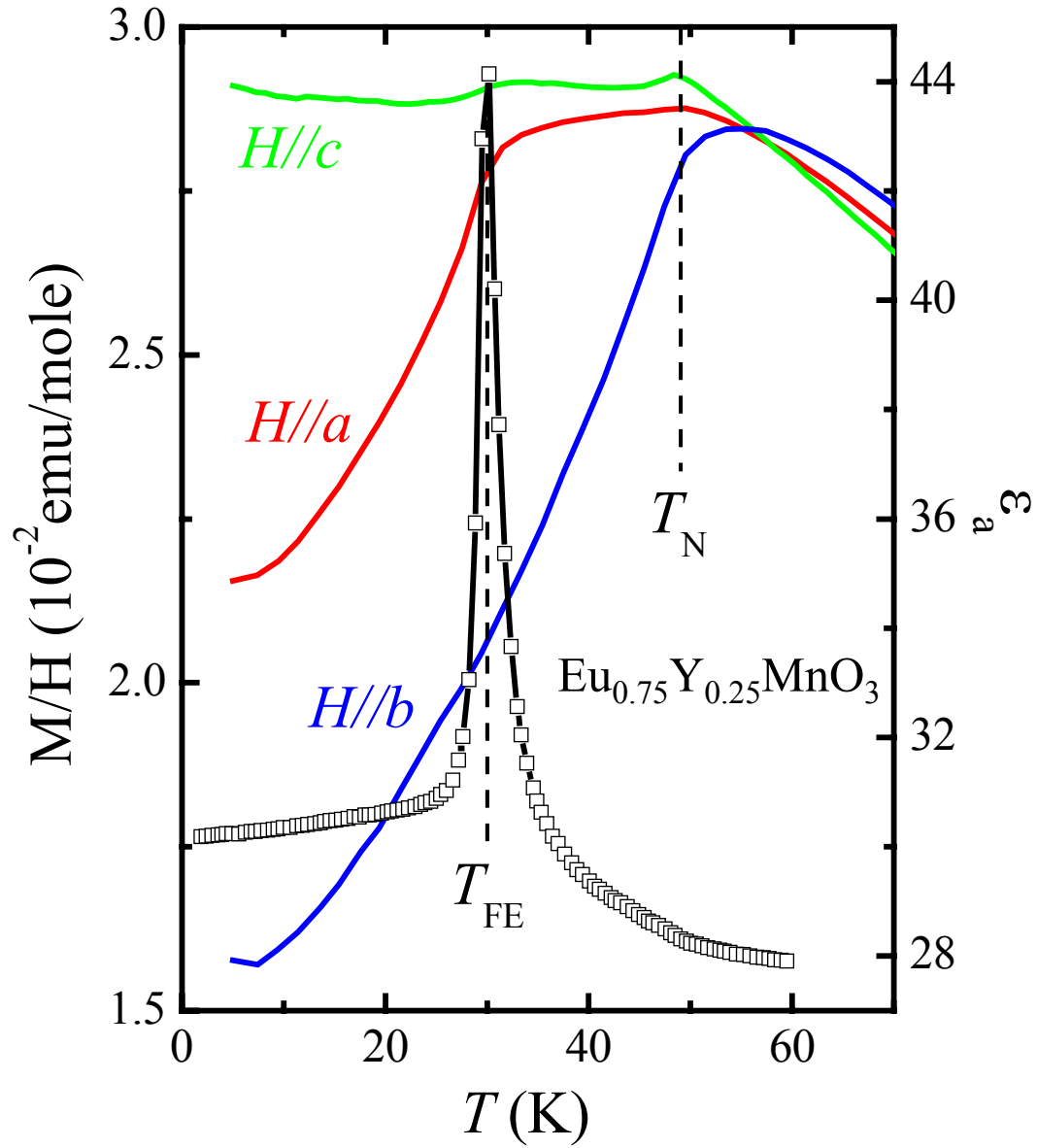


FIG. I. 8. Anisotropic magnetization as well as the dielectric constant along the ferroelectric polarization direction ($E//a$) for $\text{Eu}_{0.75}\text{Y}_{0.25}\text{MnO}_3$ [34].

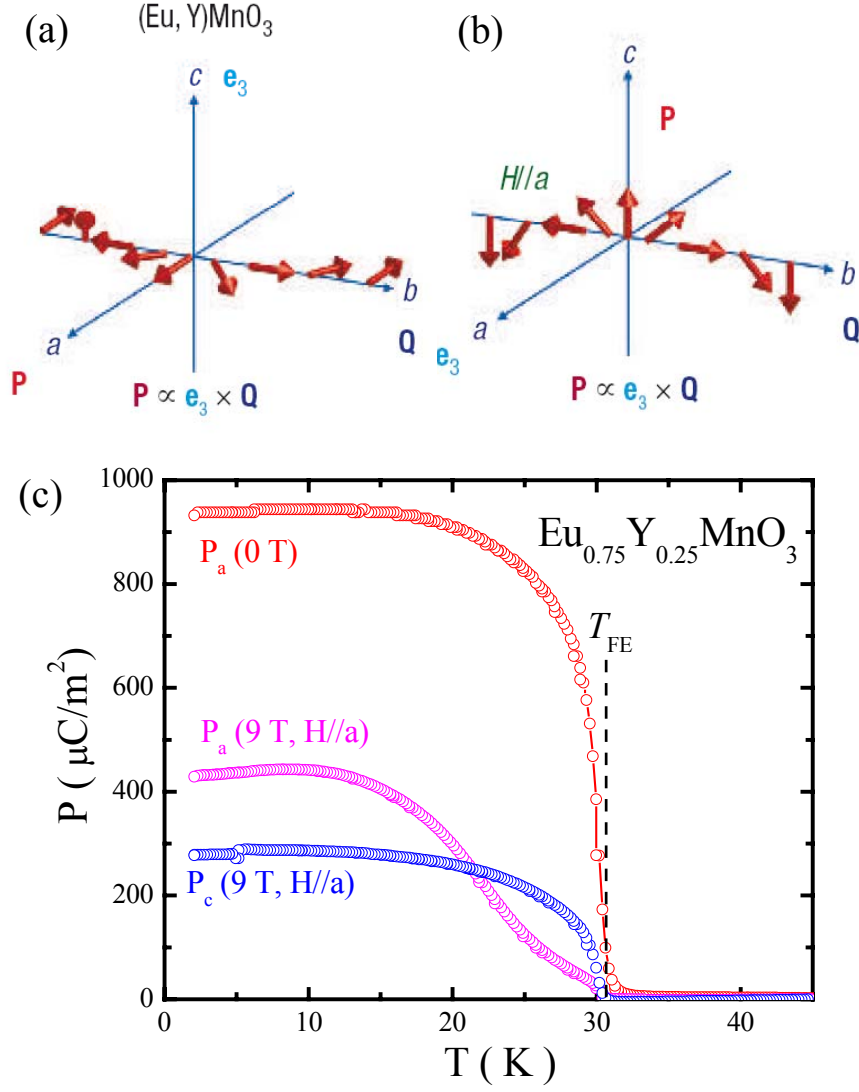


FIG. 1. 9. (a) Spiral spin state of $(\text{Eu}, \text{Y})\text{MnO}_3$ in zero magnetic field. In $H=0$ T, polarization appears along the a axis with the spiral a - b plane and $\mathbf{Q} // b$. (b) For $H//a$, Mn spins undergo spin-flop transition, leading to the polarization along the c direction. (c) Temperature dependence of ferroelectric polarization in $\text{Eu}_{0.75}\text{Y}_{0.25}\text{MnO}_3$ [34]. For $H//a$, Mn spins are overtaken by the b - c plane around $H=9$ T, leading to decrease in P_a and increase in P_c .

$= 2\pi\zeta$) becomes the ground state [35]. Even though it has been controversial, LiCu_2O_2 appears to be a wonderful example of this 1D spiral magnet with $J_F = -11 \pm 3$ meV and $J_{AF} = +7 \pm 1$ meV [36-38]. The phase diagram of LiCu_2O_2 (FIG. I. 10(a)) shows the presence of a paraelectric/paramagnetic state, a ferroelectric (FE) state with P_a , and a FE state with P_c induced by H_b . The proposed spiral spin structure in zero magnetic field is consistent with the presence of a finite electric polarization along the c axis. Electric polarization emerges along the c direction below the spiral magnetic order temperature, but changes from the c to a axis when magnetic fields (H) are applied along the b direction (FIG. I. 10(b,c)). It was also found that P_c increases with H_c , and P_a appears with H_a . LiCu_2O_2 in zero field appears to be a prototypical example of the “1D spiral-magnetic ferroelectrics”. However, the unexpected behavior in H may demonstrate the complexity associated with the quantum and fluctuating nature of the 1D $S=1/2$ magnet.

4. Collinear-Magnetism-induced Ferroelectricity

Spiral magnetic order is not the only possible route towards magnetism-induced ferroelectricity. In RMn_2O_5 ($R=\text{Tb} - \text{Lu}$), for example, a nearly-collinear acentric magnetic order with broken inversion symmetry was proposed to be responsible for ferroelectricity [5, 39]. In more detail, YMn_2O_5 shows three sequential magnetic transitions: incommensurate sinusoidal ordering of Mn spins at ~ 45 K, commensurate antiferromagnetic ordering at ~ 40 K at which ferroelectricity emerges, and reentrant incommensurate sinusoidal ordering at ~ 20 K (FIG. I. 11(a)). FIG. I. 11(b) depicts spin ordering in the nearly collinear phase of YMn_2O_5 below the 2nd transition. Mn^{3+} and Mn^{4+} ions are surrounded by O^{2-} atoms, which form pyramids and octahedra, respectively.

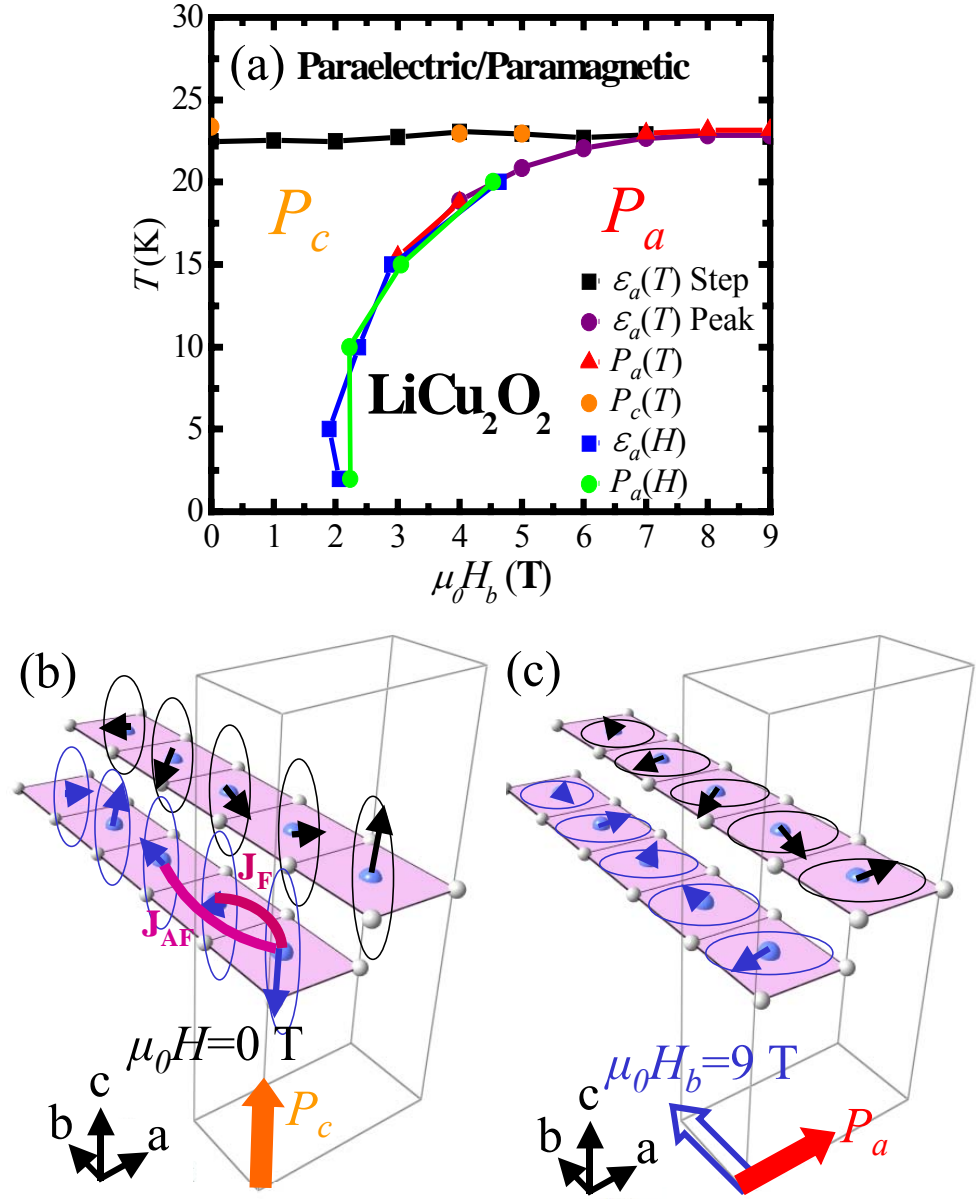


FIG. I. 10. (a) Phase diagram of LiCu_2O_2 . (b) Proposed spiral spin structure in zero field, consistent with the presence of a finite electric polarization along the c axis. (c) Proposed spiral spin structure in $H = 9 \text{ T}$ along the b axis. Electric polarization switches to the a axis. [18]

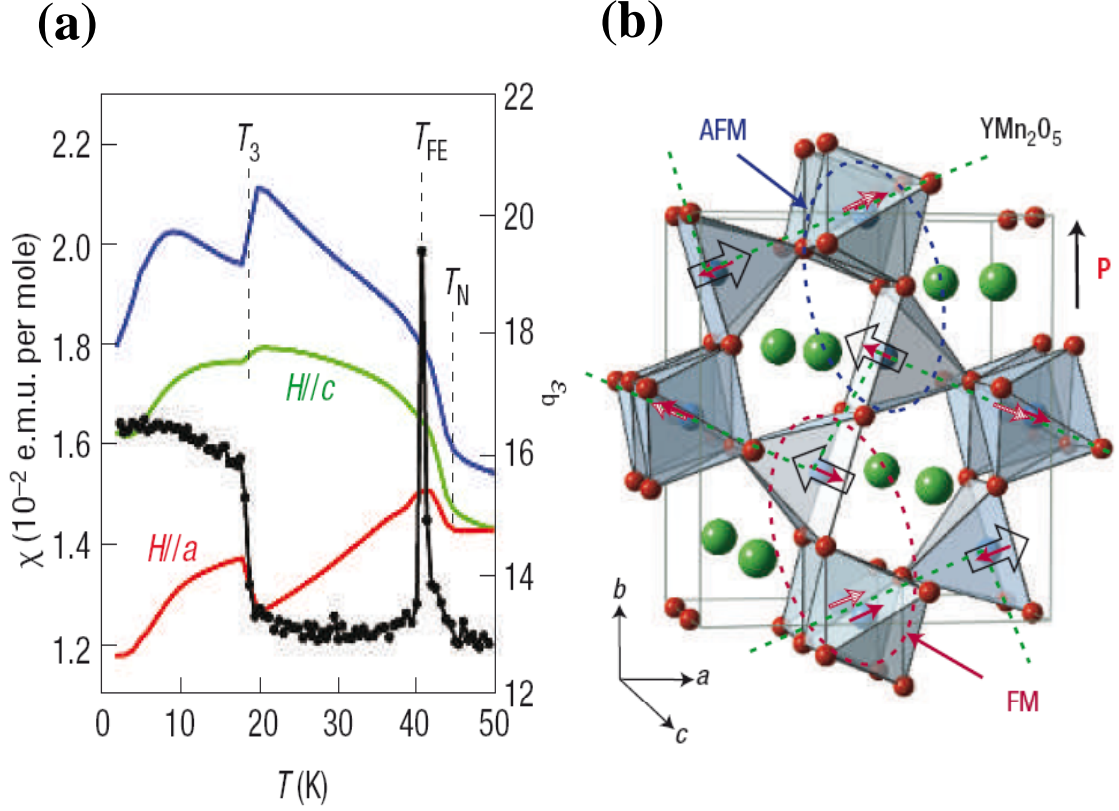


FIG. I. 11. (a) Anisotropic magnetization as well as the dielectric constant along the ferroelectric polarization direction ($E//b$) for YMn_2O_5 . (b) The crystallographic and magnetic structure of YMn_2O_5 below T_{FE} . Ferroelectricity is induced by symmetric exchange striction for alternating parallel and antiparallel Mn^{3+} - Mn^{4+} spin pairs formed along the b direction. [5, 39]

Green dashed lines indicate antiferromagnetic zigzag chains along the a axis and in the ab plane five Mn atoms form a loop. In spite of antiferromagnetic coupling of all bonds in a loop, odd number of spins gives rise to frustration and favors more complex magnetic structures. As a result, parallel (red dotted ellipsoid) and antiparallel (blue dotted ellipsoid) spin pairs across the antiferromagnetic zigzag chains form along with alternating Mn^{3+} and Mn^{4+} ions. The antiferromagnetic nearest-neighbor spin coupling and exchange striction result in expanding bonds of parallel spins and contracting bonds of antiparallel spins. The resulting Mn^{3+} distortions induce ferroelectric polarization along the b axis. On the other hand, a latest study of neutron diffraction on YMn_2O_5 determines complex spiral spin structures and the presence of Mn^{4+} spiral chains along the c axis also contributes to polarization along the b axis. Thus, the dominant contribution to the b -axis polarization is currently uncertain.

A simple and conceptually important model in which a collinear spin order induces ferroelectricity through symmetric superexchange has been discussed [5]. As illustrated in FIG. I. 12(a), up-up-down-down ($\uparrow\uparrow\downarrow\downarrow$)-type spin order can be constructed using an Ising spin chain with competing nearest-neighbor ferromagnetic (J_F) and next-nearest-neighbor antiferromagnetic (J_{AF}) interactions, being $|J_{AF}/J_F| > 1/2$. If the charges of magnetic ions alternate along the chain, this magnetic ordering breaks inversion symmetry on magnetic sites. Favoring ferromagnetic nearest-neighbor spin coupling, ions are shifted away from centrosymmetric positions (dotted red circles), inducing electric polarization via exchange striction along the chain direction. This theoretical prediction has been remarkably realized in an Ising chain magnet of $\text{Ca}_3(\text{Co,Mn})\text{O}_6$ [19] and more details are discussed in Chapter III. Another possible example has also been suggested for

perovskite YNiO_3 . As seen in FIG. I 12(b), $\uparrow\uparrow\downarrow\downarrow$ spin order in the ab plane combined with charge ordering (slight valence difference of alternating Ni ions) would induce ferroelectric polarization along the diagonal direction.

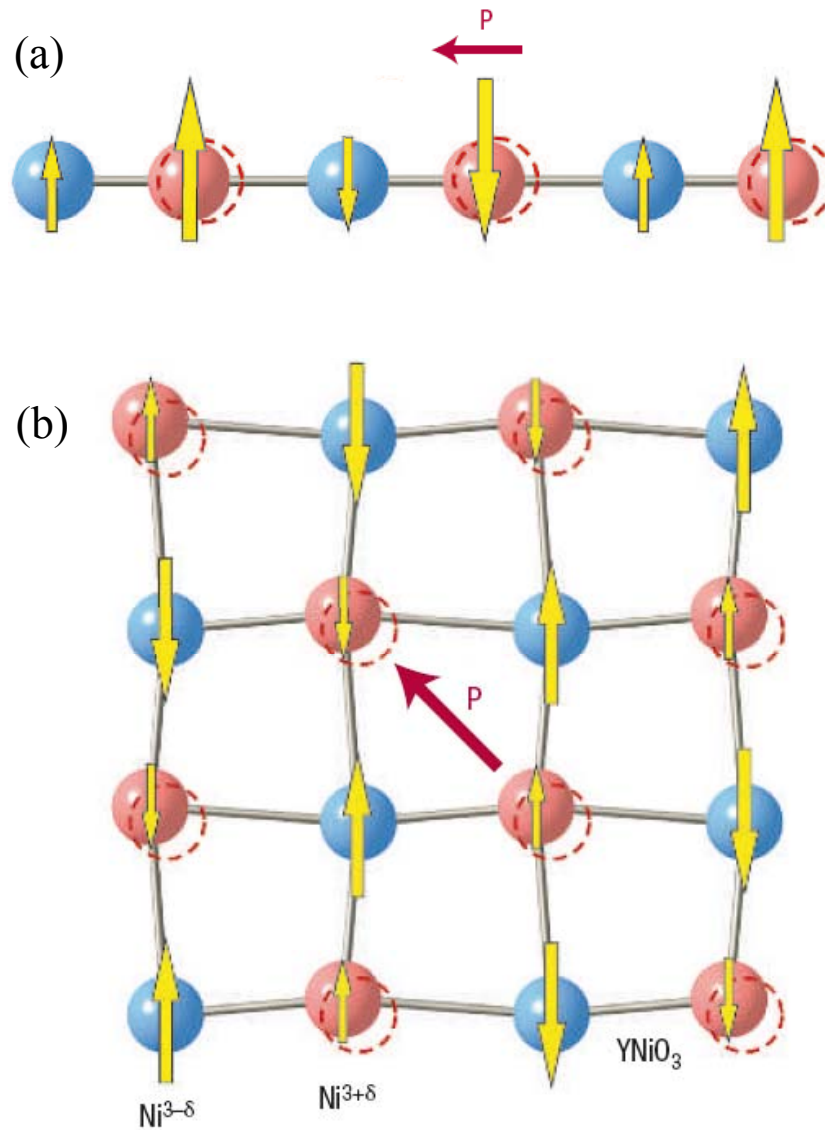


FIG. I. 12. (a) Polarization induced by exchange striction of alternating magnetic ions having up-up-down-down spin order. (b) Possible polarization along the diagonal direction in the ab plane of YNiO_3 . [5]

5. REFERENCES

- [1] M. Fiebig, J. Phys. D **38**, R123 (2005).
- [2] N. Spaldin and M. Fiebig, Science **309**, 391 (2005).
- [3] D. I. Khomskii, J. Magn. Magn. Mater. **306**, 1 (2006).
- [4] W. Eerenstein *et al.*, Nature **442**, 759 (2006).
- [5] S-W. Cheong and M. Mostovoy, Nature Mater. **6**, 13 (2007).
- [6] T. Kimura, Annu. Rev. Mater. Res. **37**, 387 (2007).
- [7] T. Kimura *et al.*, Nature **426**, 55 (2003).
- [8] N. Hur *et al.*, Nature **429**, 392 (2004).
- [9] T. Goto *et al.*, Phys. Rev. Lett. **92**, 257201 (2004).
- [10] N. Hur *et al.*, Phys. Rev. Lett. **93**, 107207 (2004).
- [11] G. Lawes *et al.*, Phys. Rev. Lett. **95**, 087205 (2005).
- [12] T. Kimura *et al.*, Phys. Rev. B **73**, 220401(R) (2006).
- [13] S. Seki *et al.*, Phys. Rev. Lett. **101**, 067204 (2008).
- [14] K. Taniguchi *et al.*, Phys. Rev. Lett. **97**, 097203 (2006).
- [15] T. Kimura *et al.*, Phys. Rev. Lett. **94**, 137201 (2005).
- [16] Y. Yamasaki *et al.*, Phys. Rev. Lett. **96**, 207204 (2006).
- [17] Y. J. Choi *et al.*, Phys. Rev. Lett. **102**, 067601 (2009).
- [18] S. Park *et al.*, Phys. Rev. Lett. **98**, 057601 (2007).
- [19] Y. J. Choi *et al.*, Phys. Rev. Lett. **100**, 047601 (2008).
- [20] Y. J. Jo *et al.*, Phys. Rev. B **79**, 012407 (2009).
- [21] T. Kimura *et al.*, Nature Mater. **7**, 291 (2008).
- [22] A. Daoud-Aladine *et al.*, arXiv/cond-mat/0812.4429v1 (2009).

- [23] H. Katsura *et al.*, Phys. Rev. Lett. **95**, 057205 (2005); C. Jia *et al.*, Phys. Rev. B **76**, 144424 (2007).
- [24] M. Mostovoy, Phys. Rev. Lett. **96**, 067601 (2006).
- [25] T. A. Kaplan and S. D. Mahanti, arXiv/cond-mat/0608227 (2006).
- [26] R. E. Cohen, Nature **358**, 136 (2002).
- [27] R. Seshadri and N. A. Hill, Chem. Mater. **13**, 2892 (2001).
- [28] T. Kimura *et al.*, Phys. Rev. B **67**, 180401(R) (2003).
- [29] A. P. Levanyuk and D. G. Sannikov, Sov. Phys. Usp. **17**, 199 (1974).
- [30] B. B. van Arken *et al.*, Nature Mater. **3**, 164 (2004).
- [31] C. J. Fennie and K. M. Rabe, Phys. Rev. B **72**, 100103 (2005).
- [32] D. V. Efremov *et al.*, Nature Mater. **3**, 853 (2004).
- [33] N. Ikeda *et al.*, Nature **436**, 1136 (2005).
- [34] Y. J. Choi, C. L. Zhang, and S-W. Cheong, unpublished.
- [35] R. Bursill, *et al.*, Phys. Condens. Matter **7**, 8605 (1995).
- [36] T. Masuda *et al.*, Phys. Rev. Lett. **92**, 177201 (2004).
- [37] S.-L. Drechsler *et al.*, Phys. Rev. Lett. **94**, 039705 (2005).
- [38] L. Mihály *et al.*, Phys. Rev. Lett. **97**, 067206 (2006).
- [39] L. C. Chapon, *et al.*, Phys. Rev. Lett. **96**, 097601 (2006).

Chapter II

Thermally or Magnetically Induced Polarization

Reversal in the Multiferroic CoCr_2O_4

1. Introduction

Magnetism and ferroelectricity are known to coexist in a special class of materials termed multiferroics [1, 2]. Large cross-coupling effects between magnetism and ferroelectricity in multiferroics have been a primary driver of multiferroics research. Magnetically-driven ferroelectrics where magnetic order with broken inversion symmetry accompanies the occurrence of ferroelectric polarization, have been of great recent interest, the first example of which was reported by Newnham *et al.* [3] and termed magnetoferroelectricity. Recently, high tunability of dielectric properties by applied magnetic fields, such as reversibly flipping ferroelectric polarization or a drastic change of dielectric constant with applied magnetic fields, has been found in such materials. [4-6] Spinel CoCr_2O_4 , which shows a complex conical spiral ferrimagnetic spin order [7], is unique among such materials [3, 8-15] in that it has a spontaneous magnetization \mathbf{M} , and the spiral component induces the observed electric polarization \mathbf{P} [12]. (All other spiral multiferroics are antiferromagnetic, as far as we are aware.) In addition to \mathbf{M} and \mathbf{P} , a multiferroic domain is characterized by a magnetic modulation wave vector \mathbf{Q} , and single such domains can be produced by various poling procedures. Here we report the first comprehensive study of the switching behavior of these domains under variation of applied magnetic fields, and temperature. We find that \mathbf{Q} -dependence of \mathbf{P} differs from that expected from previous simpler spiral orderings, where a change in $\text{sign}(\mathbf{P})$ accompanies a change in $\text{sign}(\mathbf{Q})$.

CoCr_2O_4 (CCO) crystallizes in a normal cubic spinel structure, magnetic Co^{2+} and Cr^{3+} ions occupying the tetrahedral (A) and octahedral (B) sites respectively (FIG. II. 1). For nearest-neighbor (nn) isotropic and antiferromagnetic A-B, A-A and B-B exchange

interactions, (J_{AB}, J_{AA}, J_{BB}) , one has a collinear ferrimagnetic ground state if J_{AB} dominates, e.g. the Nèel state [16] in magnetite. But for $J_{BB} \sim J_{AB}$ (J_{AA} being neglected), an approximate, variational solution for the ground state was found, a “ferrimagnetic spiral”, where the spins lie on conical surfaces [17-19]: The spins on each of the 6 f.c.c. sublattices containing the magnetic sites are given by

$$\mathbf{S}_{n\nu} = \sin \theta_\nu [\hat{x} \cos(\mathbf{Q} \cdot \mathbf{r}_{n\nu} + \gamma_\nu) + \hat{y} \sin(\mathbf{Q} \cdot \mathbf{r}_{n\nu} + \gamma_\nu)] + \hat{z} \cos \theta_\nu, \quad 0 \leq \theta_\nu \leq \pi, \nu = 1, \dots, 6. \quad (\text{I-1})$$

For fixed ν , $\mathbf{r}_{n\nu}$ goes over the sites of the given sublattice, the values of the cone $1/2$ -angle θ_ν and phase γ_ν depend on the sublattice ν , the wave vector \mathbf{Q} and the orthogonal unit vectors $\hat{x}, \hat{y}, \hat{z}$ being the same for all sublattices. This is illustrated (partially) in FIG. II. 1. The exchange forces determine that $\mathbf{Q} \cong (0.6, 0.6, 0)$ (in units of $2\pi/\text{lattice constant}$), or any of its cubic equivalents; they also determine the θ ’s and γ ’s (see [17]-[19] for further details). The direction \hat{z} of the cone axes is determined by smaller, anisotropic forces.

A state approximately of this form was found from powder neutron diffraction by Menyuk *et al.* [7] in CCO, with \hat{z} the [001] crystal direction when \mathbf{Q} is in the + or – [110] direction, “[110] \mathbf{Q} -domains” (with the same relative orientation for the cubically equivalent \mathbf{Q} ’s), and later by Tomiyasu *et al.* [20] for a single crystal. In particular, the wave vector was found to be $\mathbf{Q} = (0.62, 0.62, 0)$, in good agreement with the theoretical prediction [17]. For further details as to comparison between theory and experiment regarding the magnetic structure, see [7], [18], [19]. In [110] domains, the z -components produce the magnetization \mathbf{M} (along $\pm [001]$). According to Yamasaki *et al.* [12], the spiral components give rise to ferroelectricity, their results being interpreted according to

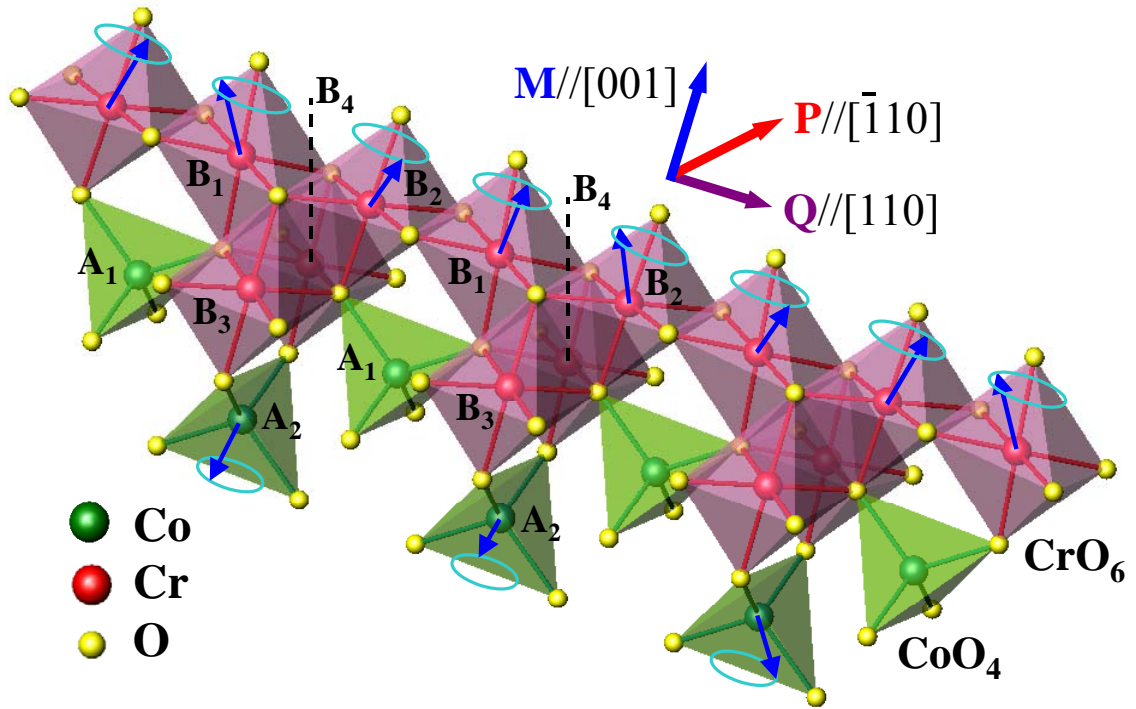


FIG. II. 1. Crystallographic and low- T magnetic structure of spinel CoCr_2O_4 . Co^{2+} and Cr^{3+} ions are located at the center of tetrahedral and octahedral O^{2-} cages, respectively. Conical spiral spins of Co^{2+} (green balls) and Cr^{3+} ions (red balls) for only 3 of the 6 sublattices (A_2 , B_1 , and B_2) are shown for clarity. Cone angles shown are from [12], which, with [13], should be consulted for more details. Also shown are the directions of \mathbf{M} , \mathbf{P} and \mathbf{Q} .

the model of Katsura *et al.* [21] (see also [22], [23]), where $\mathbf{P} \propto \mathbf{e}_{12} \times (\mathbf{S}_1 \times \mathbf{S}_2)$ for a pair of spins \mathbf{S}_1 and \mathbf{S}_2 with relative displacement \mathbf{e}_{12} . For the spiraling components of the Cr spins lying along the $[110]$ chains, shown in FIG. II. 1, this gives the same contribution for every nearest-neighbor (nn) pair, namely $\mathbf{P} \propto \mathbf{Q} \times [001] \propto [\bar{1}10]$, as seen in FIG. II. 1, and as observed [12].

2. Experimental Method

Single crystals of CoCr_2O_4 were grown by chemical vapor transport method [24], using chlorine as a transport agent. The starting material was the polycrystalline powders of CoCr_2O_4 obtained by a standard solid state reaction technique. A crystal was cut and polished with the $(\bar{1}10)$ plane of $\sim 4 \text{ mm}^2$ and a thickness of $\sim 0.2 \text{ mm}$, and then annealed at 650°C for 5 hours to remove strain built up during polishing. Magnetic measurement was performed in a SQUID magnetometer, specific heat was measured using a Quantum Design PPMS, and dielectric constant, ϵ , was measured using an LCR meter at $f = 44 \text{ kHz}$. The temperature [magnetic field] dependence of electric polarization, \mathbf{P} , was obtained by the integration of pyroelectric [magnetoelectric] current measured using an electrometer with the temperature [magnetic field] variation of 4 K/min [$0.01\text{-}0.02 \text{ T/s}$] after poling a specimen from 120 K (above the ferrimagnetic transition temperature of 95 K) to 7 K [a specific T] in a static electric field, $E \approx 10 \text{ kV/cm}$. While poling, a static magnetic field ($H = 0.5 \text{ T}$ for FIG. II. 4 and 5) was also applied along the magnetic easy axis of the $[001]$ direction, so that this magnetoelectric cooling procedure with E and H fixes the directions of the possible electric polarization, the magnetic domain, and the wave vector. The electric field was removed before collecting data of pyroelectric and

magnetoelectric currents. Experiments of x-ray absorption spectroscopy and resonant soft x-ray magnetic scattering were performed with the elliptically polarized-undulator beamline at National Synchrotron Radiation Research Center in Taiwan. Soft x-ray absorption was recorded with the fluorescence yield method; the energy resolution of the incident photons was estimated to be ~ 0.15 eV. We performed resonant soft x-ray magnetic scattering on a CoCr_2O_4 single crystal with dimensions of $(2 \times 2 \times 1)$ mm³. The crystal was aligned in an ultra-high-vacuum soft-x-ray two-circle diffractometer with the $[110]$ and $[1\bar{1}0]$ axes, defining the scattering plane. The \mathbf{E} vector of the incident soft x-ray was parallel to the $[001]$ axis, i.e., the σ polarization.

3. Result and Discussion

The temperature (T) dependence of physical properties of our single-crystalline CCO, grown with a vapor-transport method [24], exhibits sharp features, indicative of three phase transitions, as displayed in FIG. II. 2. The long-range ferrimagnetic collinear spin order appears below $T_C=95$ K, in agreement with previous findings [7, 20]. A sharp but continuous increase of $M(T)$ at $T_S=27$ K is ascribed to the conical spiral order of spins, going along with a sharp peak in the specific heat, $C(T)$ and a peaky anomaly in $\alpha(T)$ along the $[1\bar{1}0]$ direction where the electric polarization emerges. A step-like jump of $M(T)$ at $T_L=14$ K (see also FIG. II. 4), accompanied by a small feature in $C(T)$ and $\alpha(T)$, is associated with a small, but clear thermal hysteresis (not shown in FIG. II. 2), indicating the 1st order nature of this transition. Similar, but much less sharp, features were also previously observed [12].

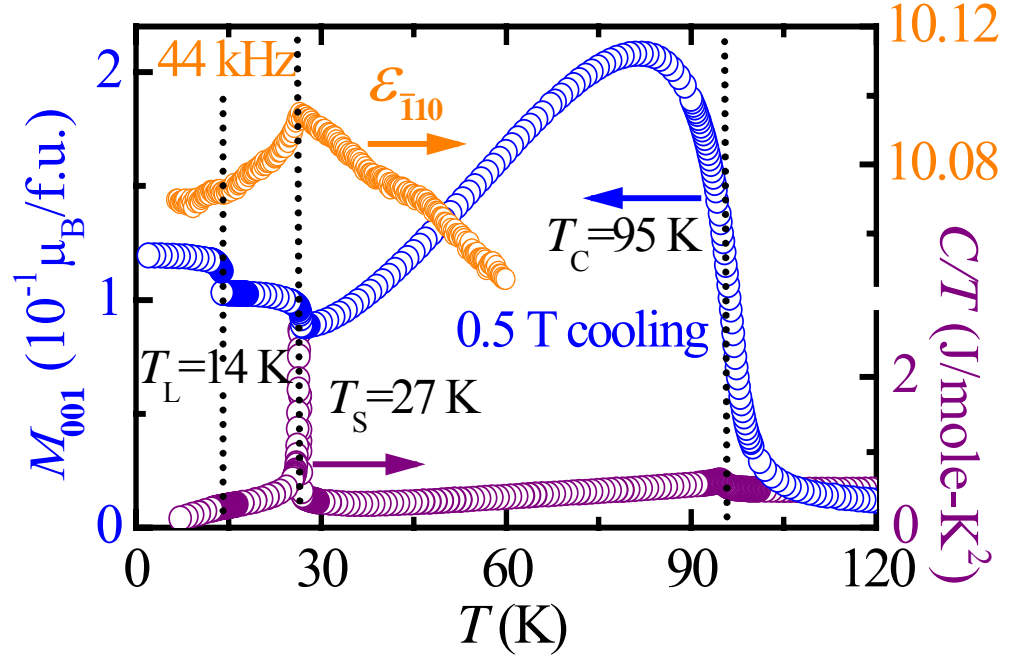


FIG. II. 2. T dependence of magnetization, \mathbf{M} , along the $[001]$ direction in $H=0.5$ T upon cooling, specific heat divided by temperature in $H=0$ T upon cooling, and dielectric constant in $H=0$ T at 44 kHz upon warming. The existence of three phase transitions is evident, and T_C , T_S , and T_L denote temperatures for ferrimagnetic transition, conical spin ordering, and lock-in transition, respectively.

It is worthy to discuss how the features of physical properties at the 14 K transition depend on the quality of single crystals grown with different techniques. The T dependence of magnetization, \mathbf{M} , for crystals grown by various methods is shown in FIG. II. 3(a). Our single crystalline specimen, prepared with a chemical vapor transport (CVT) technique and measured in 0.01 T (solid circles in red) and 0.5 T (solid lines) upon cooling, shows clear step-like sharp features at 14 K. A similar step-like feature at 14 K is evident in $\mathbf{P}(T)$ shown in FIG. II. 4. In addition, there exists a thermal hysteresis: the transition temperatures differ by ~ 0.6 K between cooling and warming run (in $H=0.5$ T). This thermal hysteresis and the step-like features clearly represent the 1st-order nature of the 14 K transition. On the other hand, for a crystal grown with a floating zone (FZ, solid circles in blue) method [12], the 14 K-transition feature in $\mathbf{M}(T)$, measured in 0.01 T upon cooling, appears smeared or reduced significantly. In addition, the spiral magnetic transition at $T_s=27$ K in both $\mathbf{M}(T)$ and $C/T(T)$ (heat capacity plotted in FIG. II. 3(b)) emerges broad while the CVT crystal reveals much sharper features at 27 K. In a flux-grown (FG, solid circles in orange) crystal [20], both transitions at 14 and 27 K appear almost absent in $\mathbf{M}(T)$. Note that the spin correlation length (~ 600 Å) deduced from the x-ray peak width of the CVT crystal is significantly larger than the results of a recent neutron scattering experiment on a FG crystal, showing the correlation length of less than 30 Å [20]. It should be emphasized that the \mathbf{P} reversal at 14 K was not observed in a FZ crystal [12], but our observation of the \mathbf{P} flipping at 14 K is highly reproducible in the CVT crystals: it was observed in a number of our CVT crystals. The high sensitivity of the nature of the 14 K transition on the quality of single crystals (or the crystal growth technique) probably stems from the metastable nature of the 1st-order 14 K

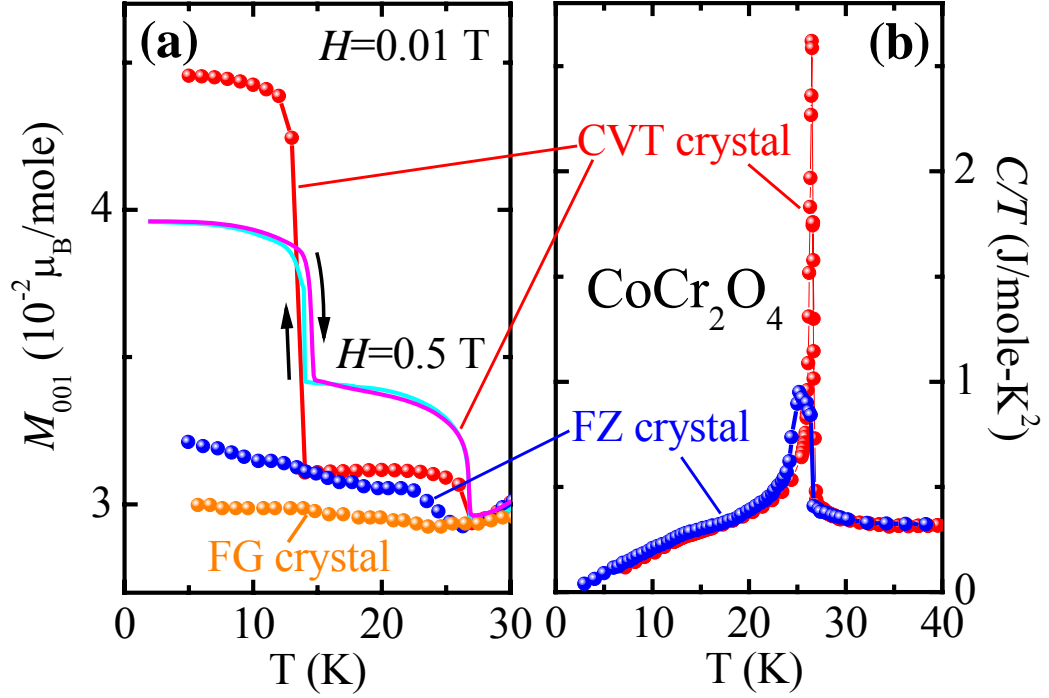


FIG. II. 3. (a) T dependence of magnetization, \mathbf{M} , for crystals grown with different methods. \mathbf{M} on a crystal grown with a chemical vapor transport (CVT) method was measured in 0.01 T upon cooling (solid circles in red) and 0.5 T upon both cooling and warming (solid lines). Magnetizations on floating-zone and flux-grown crystals (FZ and FG crystals), measured in 0.01 T, are from References 12 and 20, respectively. Magnetizations are normalized to \mathbf{M} ($H=0.01$ T, $T=27.5$ K) of the CVT crystal. (b) T dependence of heat capacity divided by T , C/T , for CVT (solid circles in red) and FZ (solid circles in blue) crystals.

transition as well as the long-range lattice interaction associated with electric polarization. It is noteworthy that crystals grown with flux methods are highly susceptible to the incorporation of chemical impurities from flux, and crystals grown with floating zone methods tend to have concentration gradient/variation due to the kinetic (thermodynamic non-equilibrium) nature of the growth.

The onset of ferroelectricity along the $[\bar{1}10]$ direction, signified by the emergence of polarization, matches the spiral magnetic ordering transition at $T_s=27$ K (FIG. II. 4); the spiral transition was found previously, but it was much less sharp [20]; the appearance of \mathbf{P} found earlier [12] is at essentially the same T . At the 14 K transition, when \mathbf{M} is kept in one direction with H , \mathbf{P} suddenly flips its direction, in contrast to the previous finding [12]. (This difference probably originates from the high quality of our crystals, indicated in the sharp phase transitions and long-range magnetic correlations.) But in agreement with [12], when H , and therefore \mathbf{M} , is reversed at fixed T we find \mathbf{P} to be reversed; as seen in FIG. II. 5(a) and (b). This correlation between \mathbf{M} and \mathbf{P} was attributed [12] to Bloch domain wall motion involved in reversing \mathbf{M} . Such an essentially uniform rotation of the spin state characterizing the wall, taking \mathbf{M} to $-\mathbf{M}$, can be seen to take a \mathbf{Q} domain to a $-\mathbf{Q}$ domain [25] (See the detail in Appendix I). We have observed directly this sign change of \mathbf{Q} upon H reversal by our circularly polarized resonant magnetic x-ray scattering experiment. Thus, \mathbf{M} , \mathbf{P} , and \mathbf{Q} change to $-\mathbf{M}$, $-\mathbf{P}$, $-\mathbf{Q}$ in $-H$, respectively (FIG. II. 5(a)). Furthermore, at 10 K (below T_L), H reversal also induces the 180° flipping of \mathbf{M} , $-\mathbf{P}$ and \mathbf{Q} (FIG. II. 5(b)).

In contrast to this behavior, we find that the sign flip of \mathbf{P} across the 14 K transition is not accompanied by a change of sign(\mathbf{Q}), rather our results indicate that the

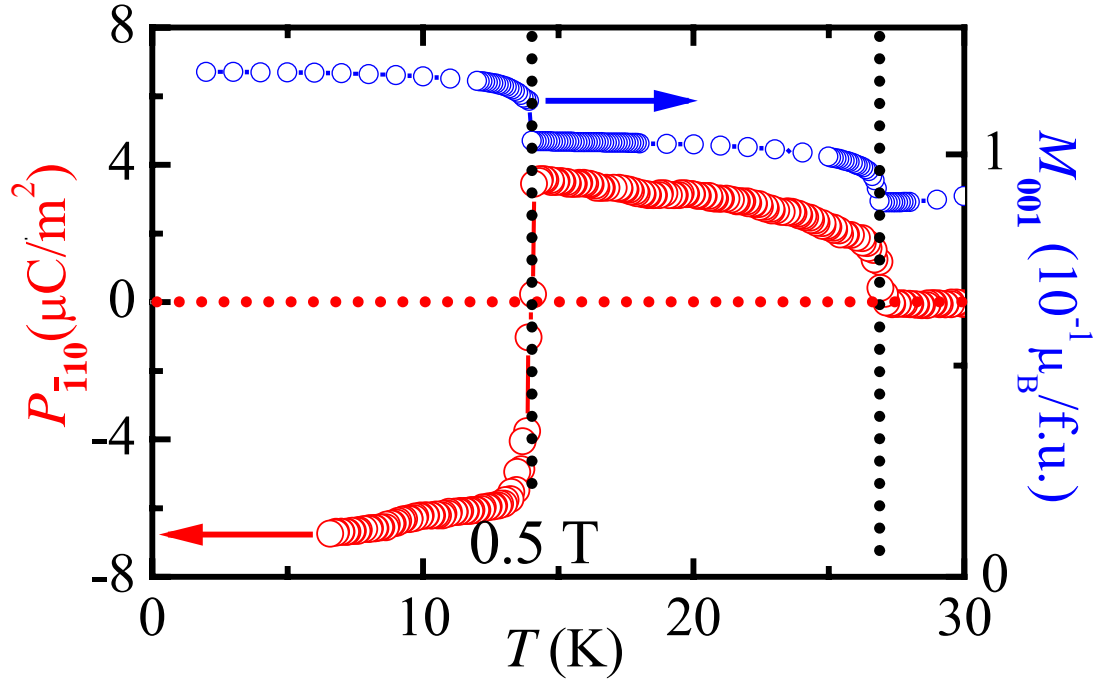


FIG. II. 4. T dependence of electric polarization, \mathbf{P} , along the $[\bar{1}10]$ direction and \mathbf{M} along the $[001]$ direction below 30 K. \mathbf{P} suddenly switches sign when cooling across 14 K without changing the signs of \mathbf{M} and \mathbf{Q} .

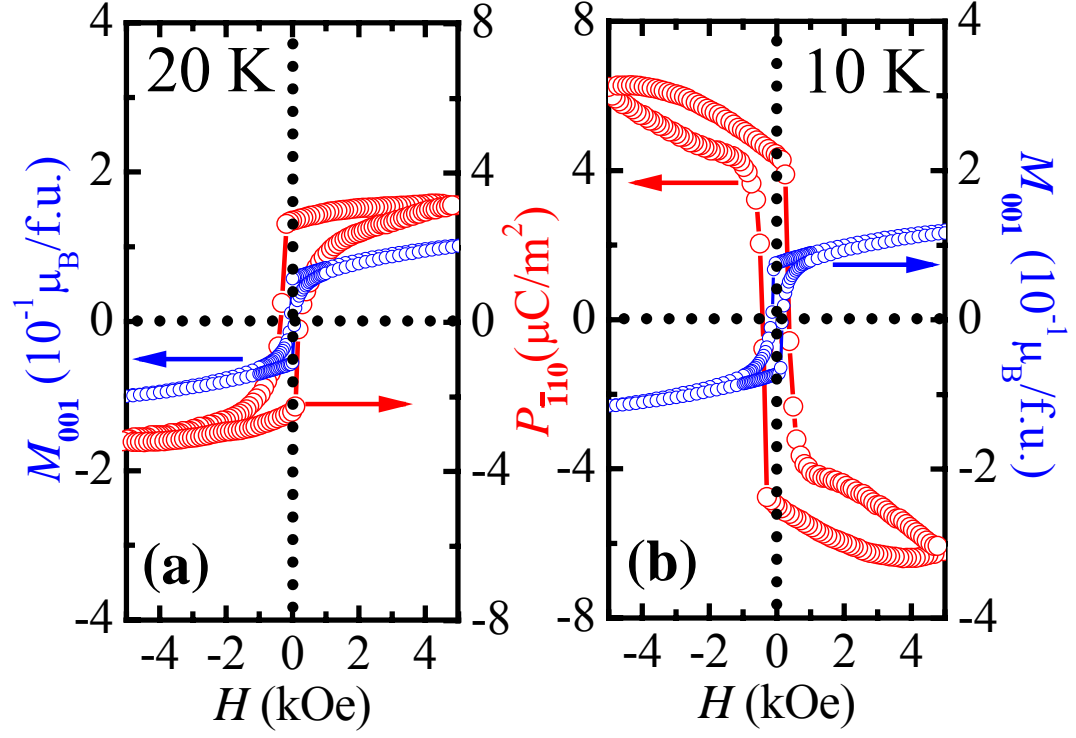


FIG. II. 5. (a) & (b) H dependence of \mathbf{M} and \mathbf{P} at 20 K and 10 K, respectively. The reversal of all of \mathbf{M} , \mathbf{P} and \mathbf{Q} is achieved by H reversal.

sign of \mathbf{Q} (or spiral handedness) is invariant at the 14 K transition (discussed further below). The low-temperature state is associated with a slight increase of the magnitude of \mathbf{M} as well as \mathbf{P} , as shown in FIG. II. 4. Note that in a multiferroic with a spiral magnetic order with only one magnetic sublattice, switching of \mathbf{P} is expected to result from the sign change of \mathbf{Q} . In other words, the direction of \mathbf{P} in such a single sublattice spiral is entirely determined by the clockwise or counterclockwise rotation of the spiraling spins along the propagation axis [26]. (This is the usual behavior found in other multiferroics with spiral magnetism.)

\mathbf{Q} -sign conservation across 14 K and change by H reversal are well evidenced in our circularly polarized resonant magnetic x-ray scattering experiment, performed with the elliptically polarized-undulator beamline at National Synchrotron Radiation Research Center in Taiwan. With photon energy tuned at Co L_3 edge, i.e., 778.4 eV, the scattering results reveal that there is an abrupt change in magnetic modulations at ~ 14 K. Unlike earlier neutron results [7, 20, 27], we found two incommensurate magnetic modulations \mathbf{Q}_+ and \mathbf{Q}_- at 15 K, a temperature above T_L , while, for T below T_L , there are one commensurate modulation $\mathbf{Q}_C=(2/3, 2/3, 0)$ and two incommensurate ones, \mathbf{Q}_+' and \mathbf{Q}_-' with a separation along $[1\bar{1}0]$ much larger than that between \mathbf{Q}_+ and \mathbf{Q}_- , as illustrated in the contour plots (FIG. II. 6) which show the scattering intensity in the plane defined by the $[110]$ and $[1\bar{1}0]$ axes. The intensities of the \mathbf{Q}' peaks are 1 to 2 orders of magnitude smaller than the \mathbf{Q}_C peak, and the three vectors are approximately equal in direction as well as magnitude; similarly, the vectors \mathbf{Q}_+ , \mathbf{Q}_- are approximately equal (FIG. II. 6). The resonant magnetic X-ray scattering intensity can distinguish between spirals with wave vector \mathbf{Q} and $-\mathbf{Q}$, if the incident beam is *circularly* polarized. [28] This is similar to the

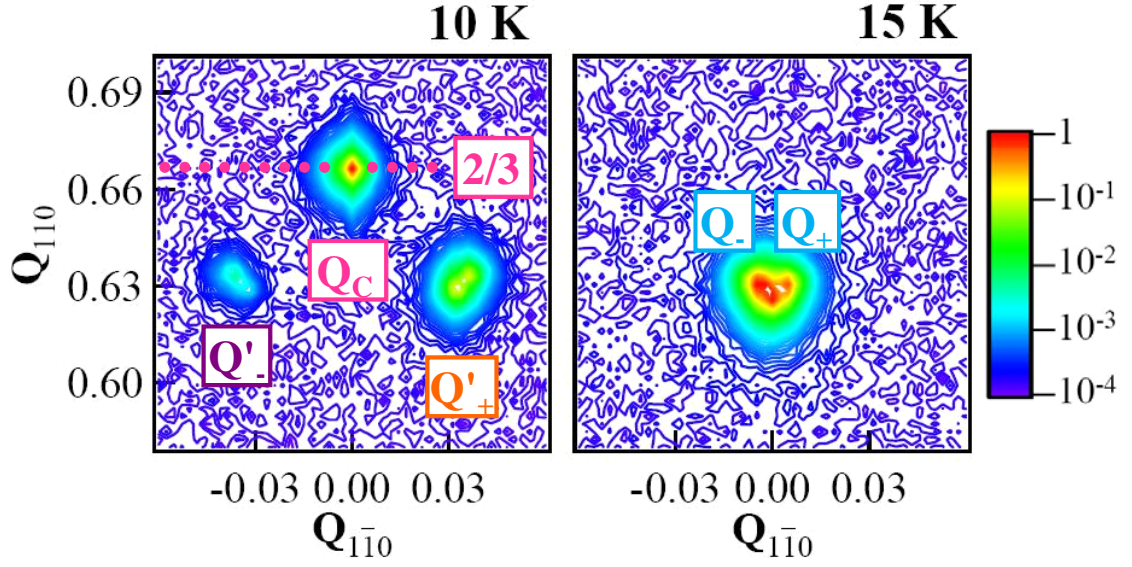


FIG. II. 6. Contour plots of the Co L_3 -edge magnetic soft x-ray scattering intensity in the plane defined by Q_{110} and $Q_{\bar{1}\bar{1}0}$ recorded at temperatures above and below T_L (14 K) with photon energy of 778.4 eV. The \mathbf{E} vector of incident x-rays was parallel to the [001] axis. The contour plots are shown in a logarithmic scale with its order of magnitude expressed by means of color.

scattering of polarized neutrons [26, 29]. In our calculation for the coherent scattering intensity of resonant magnetic x-ray (See the detail in Appendix II), it is found that the spirals of $+\mathbf{Q}$ and $-\mathbf{Q}$ cannot be distinguished by linearly polarized light because an observed peak intensity is given by an even function for the sign of \mathbf{Q} . However a peak intensity in scattering of circularly polarized light contains both even and odd function terms for the sign of \mathbf{Q} , so different scattering intensities are expected for the spirals of $+\mathbf{Q}$ and $-\mathbf{Q}$. FIG. II. 7(a), (c) and (d) show the measured scattering intensities with circularly polarized light, and the red curves and blue open circles correspond to $\pm H$ cooling of the sample, respectively. The observed scattering intensities do indeed change upon the reversal of magnetization along [001], disclosing the flip of \mathbf{Q} with H reversal. FIG. II. 6(b) also illustrates conical spiral spins above and below the 14 K transition where $\pm\mathbf{M}$ correspond to $\pm\mathbf{Q}$, respectively. Strikingly, the scattering results also reveal that the sign of the \mathbf{Q} of the largest peak at each T (\mathbf{Q}_C and \mathbf{Q}_L) remains unchanged as T changes across T_L : the H dependences of the intensities of these peaks do not reverse. Thus, to the extent that we can consider a single-wave-vector spiral as a good approximation to the observed state, this is solid evidence of $\text{sign}(\mathbf{Q})$ invariance across T_L . In addition, the only one of the smaller peaks \mathbf{Q}'_+ that has an observable intensity change on H reversal also shows this invariance, and further, the wave vectors of all the peaks are approximately equal. Therefore, even considering the complexity of having multiple Fourier components in the spin configuration, the data strongly suggest that the sign of \mathbf{Q} (for each Fourier component) does not change across the 1st order transition (See the detail in Appendix II). We note that the spin correlation length deduced from the peak width (~ 600 Å) is significantly larger than the results of a recent neutron scattering

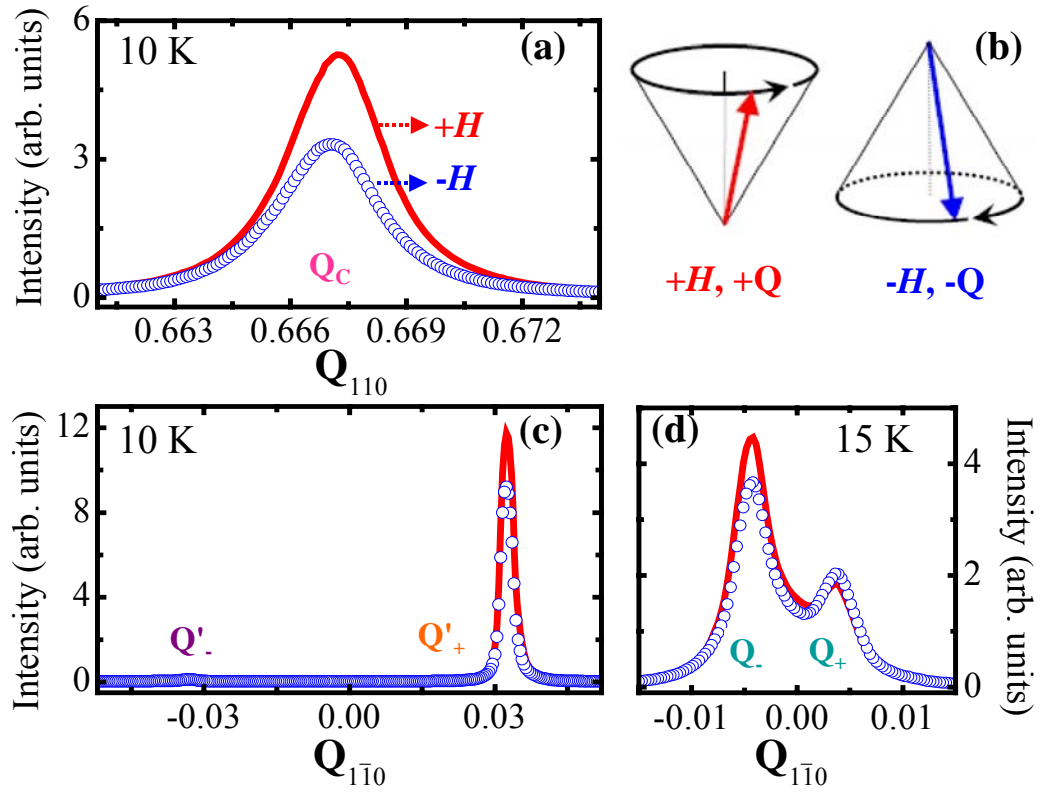


FIG. II. 7. (a), (c) & (d) Scattering intensity of \mathbf{Q} scans along $[110]$ and $[1\bar{1}0]$ under $+\mathbf{M}$ (solid curves) and $-\mathbf{M}$ (open circles) with circularly polarized x-rays. (b) Depiction of conical spiral spins where $\pm\mathbf{M}$ go with $\pm\mathbf{Q}$ above and below T_L , respectively.

experiment [20] on a flux-method-grown crystal, showing the correlation length of less than 30 Å. This difference strengthens the claim that our single crystals grown with a chemical vapor transport method are of high quality.

A plausible interpretation for the switch in sign of \mathbf{P} across 14 K without sign change of \mathbf{Q} and \mathbf{M} (despite its impossibility for a single sublattice conical spiral, as noted above) is found in a “ferrielectric”-type scenario. Now, Co^{2+} has a more-than-half-filled d shell while Cr^{3+} has a less-than-half-filled shell, suggesting that Co-Cr and Cr-Cr bonds have the opposite sign of spin-orbit interaction, resulting in the opposite directions of electric dipole moments, $\mathbf{P}_{\text{Co-Cr}}$ and $\mathbf{P}_{\text{Cr-Cr}}$ from the different bonds of form eq. (I-1) [30]. Furthermore, the bond charges that give rise to the dipole moments are inter-ionic overlap charge densities [21, 22], and are therefore very sensitive to small changes in inter-ionic distances expected to occur through the 1st order phase transition at T_L . Then, it is conceivable that the delicately balanced net polarization can change its sign at T_L without a change in sign(\mathbf{Q}) (the directions of each contribution $\mathbf{P}_{\text{Co-Cr}}$ and $\mathbf{P}_{\text{Cr-Cr}}$ don’t change, but their magnitudes do).

Repeated switching of electric polarization direction is achieved by varying temperature step-linearly with time between 8 K and 20 K as shown in FIG. II. 8. The measurement of pyroelectric current began at 8 K in the (+, −, +) state defined as (sign(\mathbf{M}), sign(\mathbf{P}), sign(\mathbf{Q})) after poling in $H=0.1$ T and $E \approx 10$ kV/cm. Upon warming, this state switches to the (+, +, +) state, but the initial state is recovered by cooling back to 8 K. Due to the 1st order nature of the T_L transition, the temperatures at which \mathbf{P} flips differ by ~ 1.6 K between warming and cooling. FIG. II. 9(a) displays how $\mathbf{P}(T)$ depends on large cooling H , showing a slight increasing tendency of T_L with increasing H . At

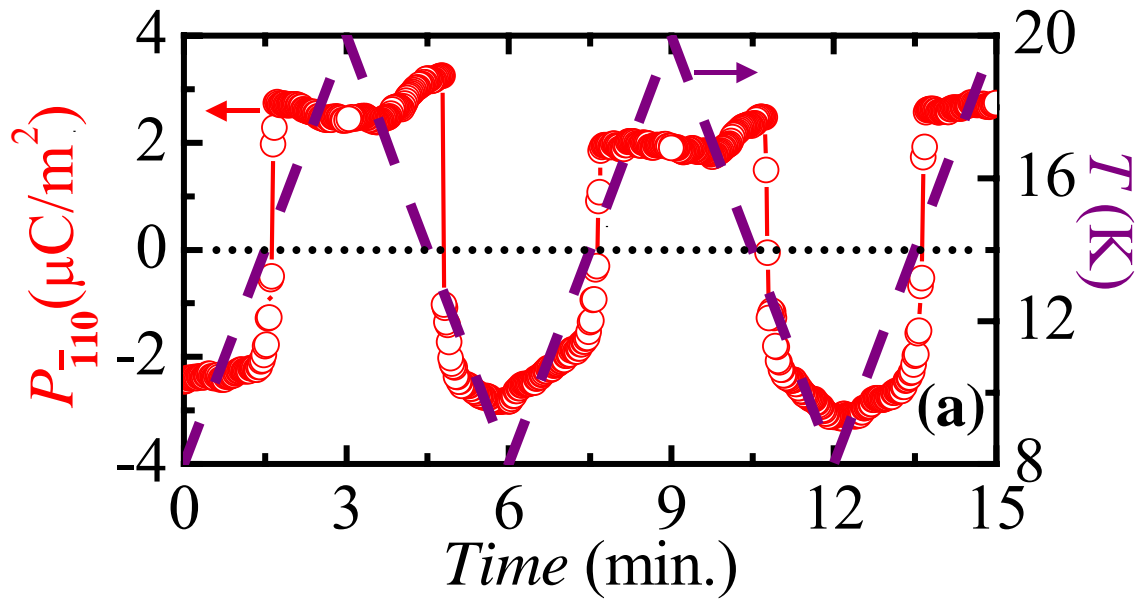


FIG. II. 8. Repeatable polarization switching with T varied linearly with time between 8 K and 20 K.

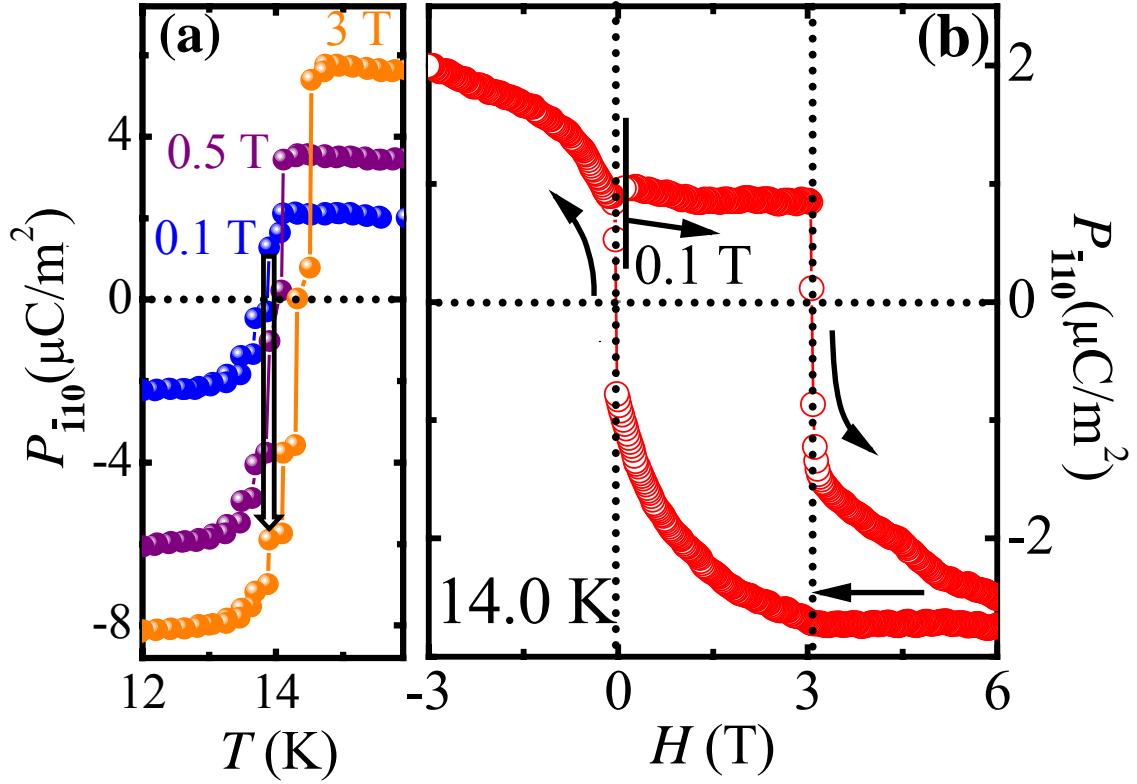


FIG. II. 9. (a) T dependence of polarization around the T_L transition in different applied H (0.1, 0.5 and 3 T), indicating that T_L increases slightly with increasing H . (b) \mathbf{P} at 14.0 K vs. H after poling the specimen in $H=0.1$ T and $E \approx 10$ kV/cm. The initial (+, +, +) state which is defined as (sign(\mathbf{M}), sign(\mathbf{P}), sign(\mathbf{Q})) changes to the (+, −, +) state in $H \approx 3$ T. Negative H scan, reversing \mathbf{M} , induces switching of \mathbf{P} and \mathbf{Q} , i.e. resulting in (−, +, −) state.

exactly 14.0 K, the phase cooled in 0.1 T is in the (+, +, +) state, whereas cooling in 3 T puts the phase in the (+, −, +) state. The black downward arrow denotes the possible switching of the physical state with increasing H at 14.0 K. As demonstrated in FIG. II. 9 (b), the isothermal polarization reversal is, indeed, achieved by varying H at 14.0 K. After cooling down to 14.0 K in 0.1 T, the phase is initially in the (+, +, +) state. The isothermal increase of H results in changing the state to (+, −, +) by reversing \mathbf{P} , but keeping the direction of \mathbf{M} and \mathbf{Q} fixed. Due to the 1st order nature of the T_L transition, the (+, −, +) state does not go back to the initial state of (+, +, +) when H is reduced to zero (or the original 0.1 T). When the H direction is reversed, \mathbf{M} flips, so do \mathbf{P} and \mathbf{Q} , and thus the (+, −, +) state becomes the (−, +, −) state. Note that in spite of the strong H -field dependence of electric polarization in CoCr_2O_4 as shown above, it does not imply the strong effects of electric fields on spontaneous magnetization. Since the electric polarization does not break time-reversal symmetry, \mathbf{P} cannot produce magnetic ordering as the spiral spin order with broken inversion symmetry induces spontaneous ferroelectric polarization. Thus the control of magnetism by electric fields, essential in novel technological application, would require other mechanisms.

We have found the concept of handedness to be convenient in describing the complex qualitative behavior of the various observables that we have found. The ferrimagnetic spiral with a clockwise or counter-clockwise spin rotation direction can be determined by the sign of \mathbf{Q} in our representation, which naturally leads to the concept of handedness, “spiral handedness” (h_s). Furthermore, the magnetoelectric domains, being characterized by the three physical parameters, \mathbf{M} , \mathbf{P} and \mathbf{Q} , allow us to define the “ \mathbf{MPQ} handedness” characterizing the relative arrangement of these three orthogonal vectors in

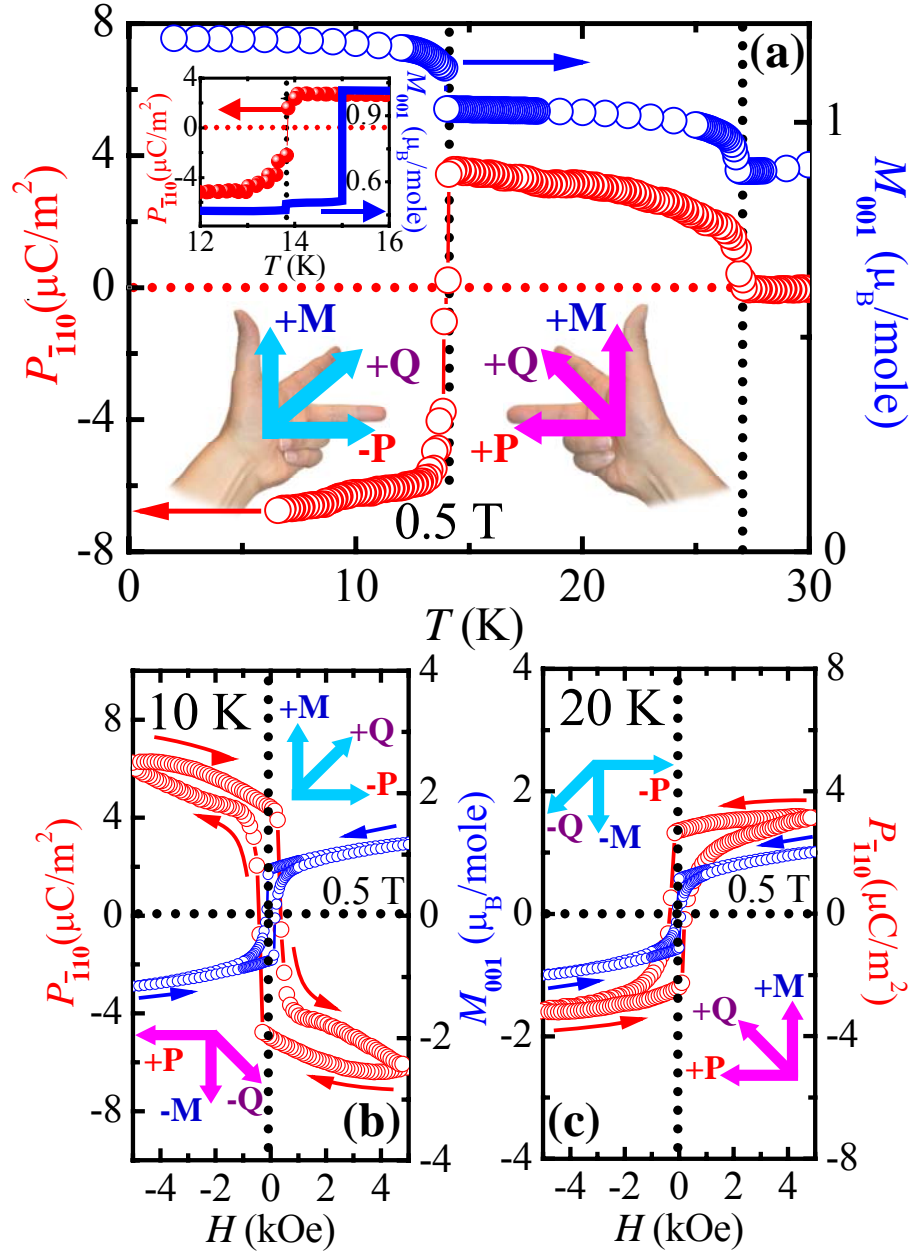


FIG. II. 10. (a) Handedness, defined by the directions of \mathbf{M} , \mathbf{P} and \mathbf{Q} switches at 14 K. The inset shows warming $\mathbf{P}(T)$ obtained after magnetoelectric cooling from 120 K to 15 K and the temperature dependence of magnetization measured upon cooling with removing H at 15 K. (b) & (c) H dependence of \mathbf{M} and \mathbf{P} at 10 K and 20 K, respectively. The reversal of all of \mathbf{M} , \mathbf{P} and \mathbf{Q} by H corresponds to flipping the \mathbf{MPQ} handedness.

a given domain. Note that handedness is often considered synonymous with chirality – loss of the mirror symmetry. However, the handed light propagation is *not* chiral (See the detail in Appendix III). Similarly, handedness concept that we use here is based on the vector cross-products rather than the mirror operations. Our definitions of both handedness are equivalent to the following precise statements.

$$h_s \equiv \text{sign}(\mathbf{S}_n^t \times \mathbf{S}_{n+1}^t \cdot \hat{\mathbf{z}}) = \text{sign}(\mathbf{Q}) \quad (\text{I. 2}),$$

$$h_{\text{MPQ}} \equiv \text{sign}(\mathbf{P} \times \mathbf{M} \cdot \mathbf{Q}) \quad (\text{I. 3}),$$

with “right” and “left” associated with + and −. Here, \mathbf{S}_n^t and \mathbf{S}_{n+1}^t are the transverse components of the spins in any one sublattice of the ferrimagnetic spiral, n and $n+1$ being successive sites along the $+[110]$ crystal direction, $\hat{\mathbf{z}}$ being in the $+[001]$ direction. The T and H dependences of various order parameters can be described by the relative switching of the two types of independent handedness. At the 14 K transition, \mathbf{P} suddenly flips its direction while keeping the directions of \mathbf{M} and \mathbf{Q} (FIG. II. 10(a)). Thus the h_{MPQ} suddenly switches from right- to left-handedness upon cooling through the 14 K transition without changing the h_s , depicted in FIG. II. 10(a) where the hands represent the relationship among \mathbf{M} , \mathbf{P} and \mathbf{Q} and three fingers in each hand stand for the directions of the vectors. H reversal at 20 K demonstrates that \mathbf{M} , \mathbf{P} , \mathbf{Q} goes to $-\mathbf{M}$, $-\mathbf{P}$, $-\mathbf{Q}$ (FIG. II. 10(c)), giving a simultaneous switching of the h_{MPQ} and h_s . The data at 10 K also indicates that even below 14 K, where the h_{MPQ} is now left-handed, it switches under reversing H with the concurrent flipping of the h_s (FIG. II. 10(b)). As shown in the inset of FIG. II. 10(a), in order to check the influence of the presence of finite E and H on the reversal of \mathbf{P} at 14 K, E and H were removed at 15 K after poling from 120 K, then the specimen was cooled to 7 K, and then warmed across 14 K without E and H . The

polarization definitely reverses even in $E=H=0$ with only a minor decrease in magnitude. We also found that \mathbf{M} , measured upon cooling (H was removed at 15 K during this cooling), decreases slightly in magnitude at 14 K without changing its sign. These decreases of \mathbf{P} and \mathbf{M} would reflect that minority domains having different \mathbf{P} and \mathbf{Q} set in at 14 K. In any case, we have demonstrated that regardless of the presence of finite E and H , the \mathbf{MPQ} handedness flips upon thermal variation across 14 K.

Finally, we discuss the possible magnetoelectric domains based on the model where the dominant energy is the Heisenberg exchange plus a small anisotropy. The exchange fixes the spiral wave vector \mathbf{Q} to be in one of the 12 cubically equivalent $[110]$ directions, with a wavelength $2\pi/Q \approx 1.06a$ (a : the lattice constant), the cone axis $\perp \mathbf{Q}$, the various cone angles, and the relative phases; the anisotropy removes the remaining degeneracy in the direction of the cone axis, picking out the $[001]$ axis when \mathbf{Q} is along $[110]$ [17, 19]. Thus the magnetization \mathbf{M} is in the $[001]$ or $[00\bar{1}]$ direction, degenerate because of time-reversal invariance of the energy. Thus we have 24 magnetic domains. The polarization \mathbf{P} is closely related to \mathbf{Q} : its direction $\hat{\mathbf{P}} = c\mathbf{e} \times \hat{\mathbf{Q}}$ where $\mathbf{e} \equiv [001]$ and c is a temperature-dependent constant of magnitude unity, as theoretically predicted [21-23] and verified experimentally (ref. 12 and present work). We find that c changes sign across the first order transition at 14 K (this possibility is explained in the text as being due to contributions to \mathbf{P} from AB and BB bonds, of opposite sign). Thus, for $T > 14$ K or < 14 K, $c = \text{constant}$, leading to the conclusion that there remain 24 magnetoelectric domains. Our poling procedure, i.e. cooling in small magnetic and electric fields, is used to select, uniquely, various ones of these domains. In detail, for a given lattice of CoCr_2O_4 , and under our poling conditions, \mathbf{M} , \mathbf{P} and \mathbf{Q} can have + or – sign, i.e. H along

MPQ handedness	$T < 14$ K				MPQ handedness	$14 \text{ K} < T < 27 \text{ K}$		
	M	P	Q			M	P	Q
L	+	-	+	\longleftrightarrow	R	+	+	+
\updownarrow					\updownarrow			
R	-	+	-	\longleftrightarrow	L	-	-	-
L	+	+	-	\longleftrightarrow	R	+	-	-
\updownarrow					\updownarrow			
R	-	-	+	\longleftrightarrow	L	-	+	+

\updownarrow : H -reversal effect \longleftrightarrow : T -variation effect

Table II. 1. Possible magnetoelectric domains in high- T ($14 \text{ K} < T < 27 \text{ K}$) and low- T ($T < 14 \text{ K}$) phases. Each phase can have four different types of domains in set of (**M**, **P**, **Q**) due to the constraint between **P** and **Q**. Each domain formed by external E and H can be described by a right or left **MPQ**-handedness (h_{MPQ}). H reversal (blue arrows) and T -cooling across 14 K (red arrows) induce transformation of one domain to another and also switching of h_{MPQ} .

$\pm[001]$, E along $\pm[\bar{1}10]$; this selects the signs of \mathbf{M} and \mathbf{P} , and automatically fixes the direction of \mathbf{Q} along $\pm[110]$. In particular, we find that $\text{sign}(\mathbf{Q})=\text{sign}(\mathbf{P})$ in the high- T phase, so that $\text{sign}(\mathbf{Q})= -\text{sign}(\mathbf{P})$ in the low- T phase. Thus there are 4 possible magnetoelectric domains to be seen in our experiment in either the high or low- T phases, as displayed in Table II.1, and any of these types of domain, which corresponds to a right or left **MPQ**-handedness (h_{MPQ}), can be produced by using the appropriate external E and H upon poling.

In summary, the conical spiral ferroelectricity in CoCr_2O_4 can be described by inter-relationship among ferroelectric polarization, magnetization and spiral wave vector. Our results demonstrate that spontaneous electric polarization induced by non-collinear spin order changes its sign across the magnetic lock-in transition temperature ($T_L=14$ K); furthermore the sign change occurs while keeping fixed the spin rotation direction, i.e., spiral handedness or $\text{sign}(\mathbf{Q})$. This differs from the usual behavior wherein for a simple spiral, change in $\text{sign}(\mathbf{P})$ requires the handedness to change sign, and we give a possible mechanism for such unusual behavior. We also recover the previous finding wherein $\mathbf{P} \rightarrow -\mathbf{P}$ when $\mathbf{M} \rightarrow -\mathbf{M}$ ([12]), but further show experimentally that this is accompanied by $\mathbf{Q} \rightarrow -\mathbf{Q}$, as predicted from the Bloch wall mechanism for switching \mathbf{M} . We further show that polarization reverses its direction in ~ 3 T at exactly 14.0 K, due to a slight increasing trend of T_L with increasing magnetic field.

4. REFERENCES

- [1] D. I. Khomskii, J. Magn. Magn. Mater. **306**, 1 (2006).
- [2] S-W. Cheong and M. Mostovoy, Nature Mater. **6**, 13 (2007).
- [3] R. E. Newnham *et al.*, J. Appl. Phys. **49** (12), 6088 (1978).
- [4] N. Hur *et al.*, Nature **429**, 392 (2004).
- [5] T. Goto *et al.*, Phys. Rev. Lett. **92**, 257201 (2004).
- [6] N. Hur *et al.*, Phys. Rev. Lett. **93**, 107207 (2004).
- [7] N. Menyuk *et al.*, J. de Physique **25**, 528-536 (1964).
- [8] T. Kimura *et al.*, Nature **426**, 55 (2003).
- [9] G. Lawes *et al.*, Phys. Rev. Lett. **95**, 087205 (2005).
- [10] T. Kimura *et al.*, Phys. Rev. B **73**, 220401(R) (2006).
- [11] T. Kimura *et al.*, Phys. Rev. Lett. **94**, 137201 (2005).
- [12] Y. Yamasaki *et al.*, Phys. Rev. Lett. **96**, 207204 (2006).
- [13] G. Lawes *et al.*, Phys. Rev. B **74**, 024413 (2006).
- [14] K. Taniguchi *et al.*, Phys. Rev. Lett. **97**, 097203 (2006).
- [15] S. Park *et al.*, Phys. Rev. Lett. **98**, 057601 (2007).
- [16] L. Néel, Ann. Phys. **3**, 137-198 (1948).
- [17] D. H. Lyons *et al.*, Phys. Rev. **126**, 540-555 (1962).
- [18] A review: N. Menyuk, in Modern Aspects of Solid State Chemistry, Ed. C. N. R. Rao (Plenum, NY-London, 1970), page 1.
- [19] A review: T. A. Kaplan and N. Menyuk, Phil. Mag. **87**, No. 25, 3711-3785 (2007);
Corrigendum: *ibid*, **88**, No. 2, 279 (2008).
- [20] K. Tomiyasu *et al.*, Phys. Rev. B **70**, 214434 (2004).

- [21] H. Katsura *et al.*, Phys. Rev. Lett. **95**, 057205 (2005); C. Jia *et al.*, Phys. Rev. B **76**, 144424 (2007).
- [22] T. A. Kaplan and S. D. Mahanti, arXiv/cond-mat/0608227 (2006).
- [23] M. Mostovoy, Phys. Rev. Lett. **96**, 067601 (2006).
- [24] P. Peshev *et al.*, Mat. Res. Bull. **17**, 1413-1420 (1982).
- [25] T. A. Kaplan, unpublished work.
- [26] Y. Yamasaki *et al.*, Phys. Rev. Lett. **98**, 147204 (2007).
- [27] R. Plumier, J. Appl. Phys. **39**, 635-636 (1968).
- [28] M. Blume and D. Gibbs, Phys. Rev. B **37**, 1779 (1988); T. A. Kaplan, unpublished work.
- [29] M. Blume, Phys. Rev. **130**, 1670 (1963).
- [30] T. Arima *et al.*, J. Phys. Soc. Japan, **76**, 023602 (2007).

Chapter III

Ferroelectricity in an Ising Chain Magnet

1. Introduction

The concept of magnetism-driven ferroelectricity has recently drawn a significant attention [1,2]. In magnetism-driven ferroelectrics, development of inversion-symmetry-breaking magnetic order leads to the loss of the lattice inversion symmetry through exchange striction, thereby leading to the development of ferroelectricity. In these materials, external magnetic field influences the configuration of the magnetic order, naturally leading to changes in ferroelectric or dielectric properties. Spectacular cross-coupling effects, such as reversible flipping of ferroelectric polarization or drastic change of dielectric constant in applied magnetic fields, have been recently observed in magnetism-driven ferroelectrics [3-5]. Spiral magnetic order, resulting from magnetic frustration, is a common way to induce the loss of inversion symmetry, and ferroelectricity has been recently observed in a number of spiral magnets such as TbMnO_3 , $\text{Ni}_3\text{V}_2\text{O}_8$, CuFeO_2 , $(\text{Ba,Sr})_2\text{Zn}_2\text{Fe}_{12}\text{O}_{22}$, CoCr_2O_4 , MnWO_4 , and LiCu_2O_2 [6-12]. In the spiral magnets, the relevant exchange striction is associated with the antisymmetric part of the exchange coupling, which constitutes the so-called Dzyaloshinski-Moriya (DM) interaction [13-16].

Spiral magnetic order is not the only possible route towards magnetism-induced ferroelectricity. In RMn_2O_5 ($\text{R}=\text{Tb} - \text{Lu}$), for example, a nearly-collinear acentric magnetic order with broken inversion symmetry was proposed to be responsible for the ferroelectricity [17]. In this mechanism, the ferroelectricity results from lattice relaxation through exchange striction associated with the symmetric superexchange coupling. However, a model where ferroelectricity is induced by a spiral spin configuration along the Mn^{4+} spin chain has been also discussed for RMn_2O_5 [18,19]. Thus, the true origin of

multiferroicity in RMn_2O_5 is currently uncertain. Another promising example is the so-called E-type magnetic order. This collinear order, combined with alternating oxygen cage rotations, has been suggested as the origin of ferroelectricity in the orthorhombic HoMnO_3 [20]. Polycrystalline HoMnO_3 has been experimentally studied to test this theoretical prediction [21], but the induced polarization turned out to be too small to support the proposed theory. Identification of non-spiral magnetism-driven ferroelectrics remains, therefore, an important task. Among those, systems driven by the potentially large symmetric superexchange are, clearly, of special interest.

A simple and conceptually important model in which a collinear spin order induces ferroelectricity through symmetric superexchange can be constructed using an Ising spin chain with competing nearest-neighbor ferromagnetic (J_F) and next-nearest-neighbor antiferromagnetic (J_{AF}) interactions [2]. For $|J_{AF}/J_F| > 1/2$, the ground-state magnetic order is of the up-up-down-down ($\uparrow\uparrow\downarrow\downarrow$) type [22]. If the charges of magnetic ions alternate along the chain, this magnetic ordering breaks inversion symmetry on magnetic sites and can induce electric polarization via exchange striction. This mechanism is illustrated in FIG. III. 1. The exchange striction associated with symmetric superexchange shortens the bonds between the parallel spins, while stretching those connecting the antiparallel spins. As a result, electric polarization, P , is induced in the direction of the chain. As shown in FIG. III. 1, there are two ways to combine the $\uparrow\uparrow\downarrow\downarrow$ order with the ionic charge order, giving rise to the opposite electrical polarization vectors. Experimental realization of such a simple model system would be of a significant importance in the field. Herein, we report discovery of a chain magnet in which this model is remarkably realized.

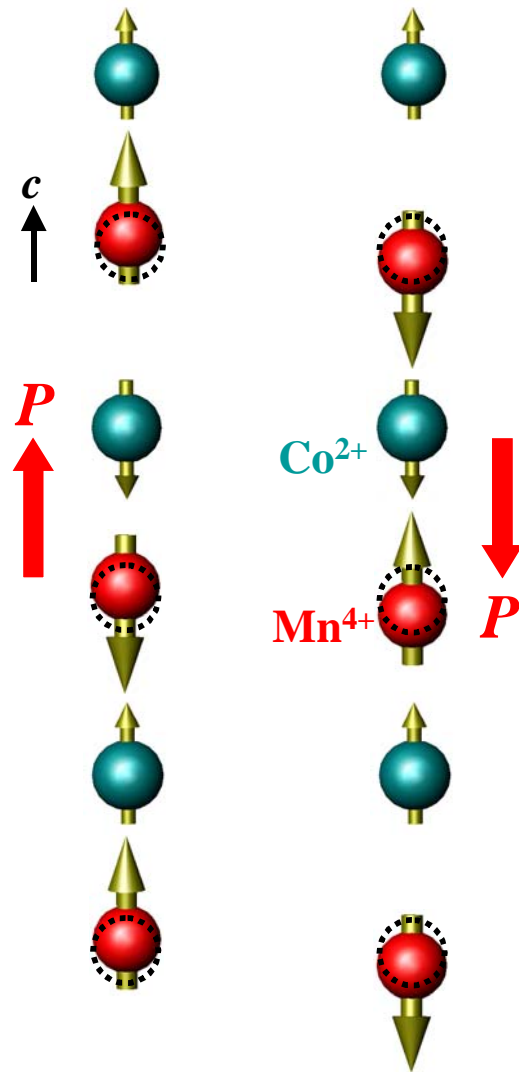


FIG. III. 1. Ising chains with the up-up-down-down spin order and alternating ionic order, in which electric polarization is induced through symmetric exchange striction. The two possible magnetic configurations leading to the opposite polarizations are shown. The atomic positions in the undistorted chains are shown with dashed circles.

2. Experimental Method

To find the appropriate experimental system, we have identified $\text{Ca}_3\text{Co}_2\text{O}_6$ -derived compounds as possible candidates because $\text{Ca}_3\text{Co}_2\text{O}_6$ is an Ising chain magnet where about a half of Co ions can be replaced by Mn ions [23,24]. The structure of $\text{Ca}_3\text{Co}_{2-x}\text{Mn}_x\text{O}_6$, as depicted in FIG. III. 2(a) and (b), contains spin chains consisting of magnetic ions with alternating oxygen cages of face-shared trigonal prisms and octahedra along the c axis. The spin chains are separated by Ca ions, and form a triangular lattice in the ab plane. Mn ions have a strong tendency to avoid the trigonal prismatic oxygen coordination. Thus, for example, for $x=1$, all the Co ions are located in the trigonal prismatic sites, and all the Mn ions occupy the octahedral sites [24]. We prepared single-phase polycrystalline $\text{Ca}_3\text{Co}_{2-x}\text{Mn}_x\text{O}_6$ with x up to 1 by using standard solid state reaction method [23]. Since single crystals are necessary for conclusive measurements of the ferroelectric properties, we have attempted to grow single crystals of $\text{Ca}_3(\text{Co,Mn})_2\text{O}_6$ by utilizing the known technique (KCl- K_2CO_3 flux method) for the growth of $\text{Ca}_3\text{Co}_2\text{O}_6$ crystals [25]. With increasing Mn concentration, the crystal growth was found to be increasingly more difficult. However, single crystals with maximum x approaching 0.96 (as determined by comparing x-ray diffraction patterns of crushed crystals with those of polycrystalline samples) were grown successfully.

DC magnetic susceptibility ($\chi=M/H$) was measured in a SQUID magnetometer, specific heat (C) and AC magnetic susceptibility (χ' and χ'') measurements were carried out in the Quantum Design PPMS, and dielectric constant (ϵ) was measured using an LCR meter at $f=44$ kHz. The temperature (T) dependence of electric polarization (P) was obtained by the integration of pyroelectric current with the T variation of 2 K/min after

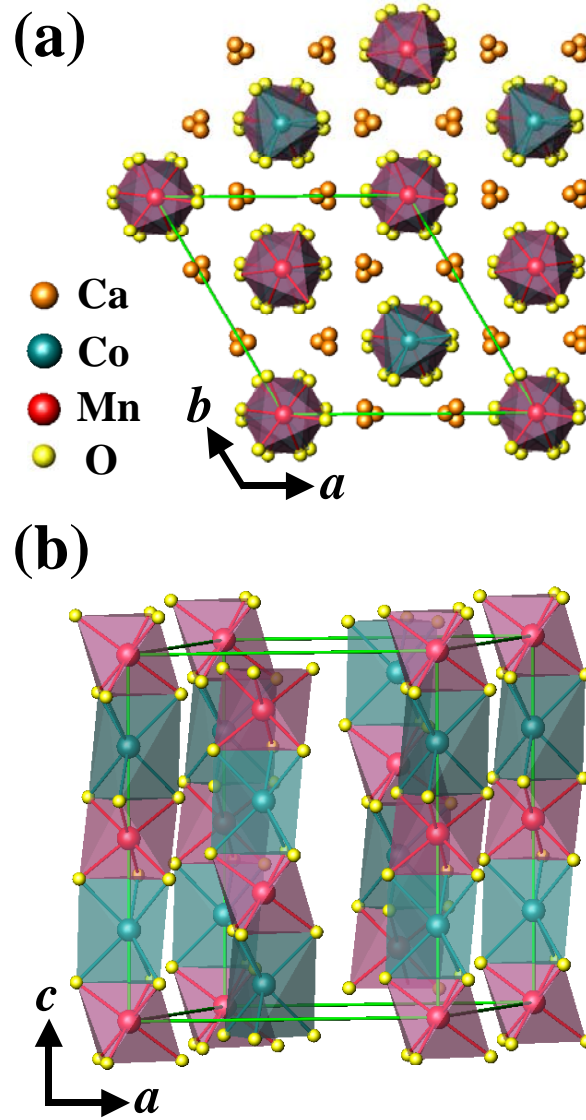


FIG. III. 2. (a) and (b) The crystal structure of the $\text{Ca}_3\text{CoMnO}_6$ chain magnet. The green boxes represent the crystallographic unit cell.

poling a specimen from 40 K to 2 K in a static electric field of $E \approx 6.7$ kV/cm. For ε and P measurements, a c -axis needle-shaped crystal was cut and polished with the ab plane cross-section of ~ 0.64 mm² and thickness of ~ 0.15 mm, and then annealed at 650 °C for 5 hours to remove strain built up during polishing. Neutron powder diffraction measurements were performed on polycrystalline $\text{Ca}_3\text{Co}_{2-x}\text{Mn}_x\text{O}_6$ ($x=0.95$) at the BT-1 beamline at NIST Center for Neutron Research. Monochromatic neutrons ($\lambda=2.079$ Å) were produced by a Ge(311) monochromator, and the data were collected for $T=1.4$, 8, and 20 K.

3. Result and Discussion

Search for the ferroelectricity was performed in the crystal with the highest Mn concentration, $x=0.96$, and ferroelectric polarization along the chain direction was indeed found. FIG. III. 3 shows that the polarization smoothly emerges below the transition temperature of 16.5 K, increases rapidly below ~ 10 K, and reaches ~ 90 $\mu\text{C}/\text{m}^2$ at 2 K. The appearance of the polarization at 16.5 K coincides with the onset of the magnetic order, which is signified [24] by a broad peak in the magnetic susceptibility, $\chi(T)$, shown in FIG. III. 4(a). Specific heat also exhibits an upturn at this temperature. The temperature dependence of the dielectric constant along the c axis, $\varepsilon_c(T)$, starts deviating from its high-temperature behavior at the onset temperature of the polarization without showing any sharp anomaly, see FIG. III. 4(b). Instead, $\varepsilon_c(T)$ reveals a broad peak at ~ 8 K followed by a sharp decrease at lower temperatures. The electric polarization decreases in a magnetic field applied along the c axis. There is an additional magnetic anomaly at

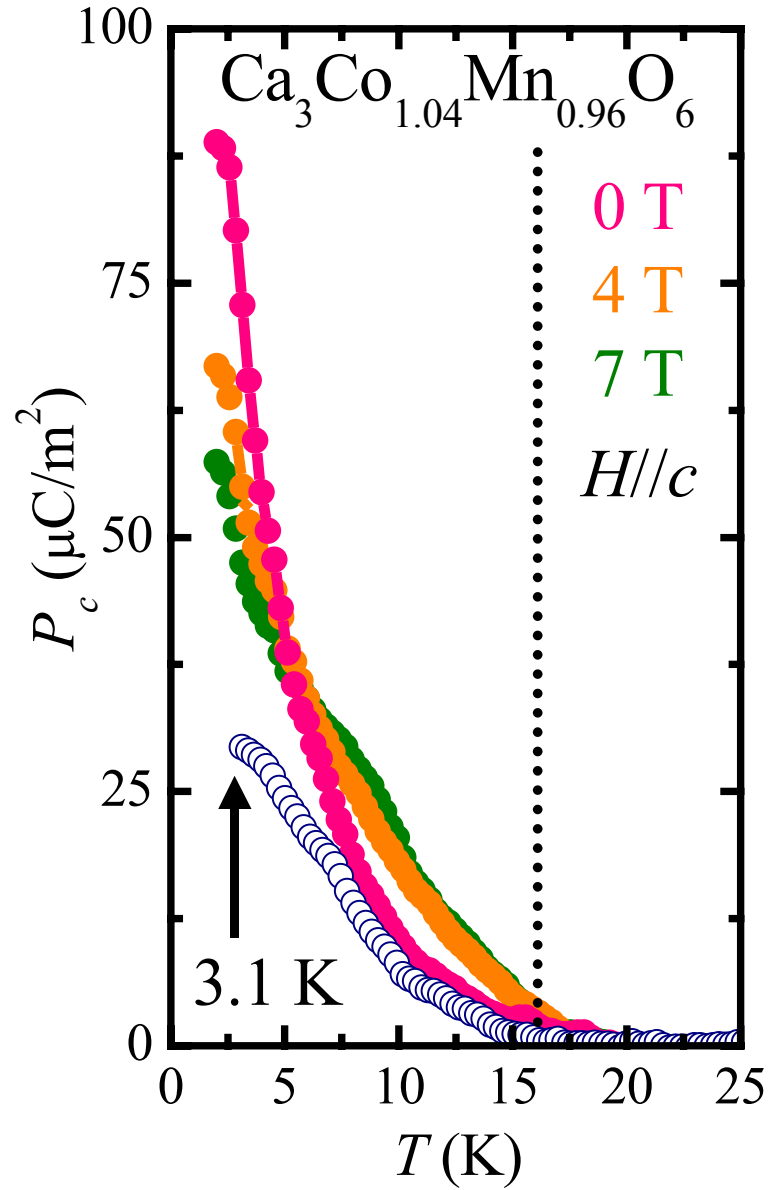


FIG. III. 3. Electric polarization of single crystal $\text{Ca}_3\text{Co}_{1-x}\text{Mn}_x\text{O}_6$ ($x=0.96$) along the chain direction ($P//c$), taken upon warming. The samples were poled upon cooling from 40 K to 2 K (filled circles), and to 3.1 K (open circles) before the measurement. The data for the 2 K poled sample were collected in various applied magnetic fields, as shown.

$T \approx 3$ K, which can be seen in the behavior of the derivative $d\chi(T)/dT$ shown in FIG. III. 4(a); it is discussed in more detail below. The Ising character of this compound is clearly reflected in the large anisotropy of $\chi(T)$.

Studies of $\text{Ca}_3\text{Co}_{2-x}\text{Mn}_x\text{O}_6$ polycrystalline samples suggest that a similar behavior is expected in a wide range of x near $x=1$. FIG. III. 5(a) and (b) display $\chi(T)$ and $\varepsilon(T)/\varepsilon(T=20 \text{ K})$ for various Mn concentrations, $x=0.85, 0.9, 0.95$ and 1.0 . These data exhibit the same features as those of the corresponding quantities of the $x=0.96$ single crystal, strongly suggesting that the observed properties of the single crystal are representative for large Mn concentrations. The temperatures of the maxima in $\chi(T)$ and $\varepsilon(T)$, shown in the insets in FIG. III. 5(a) and (b), decrease with increasing x , indicating the corresponding decrease in the magnetic transition temperature. The corresponding temperatures in the single crystal (dotted lines in the insets) agree well with the Mn concentration $x=0.96$, corroborating our x-ray results.

The structure of $\text{Ca}_3\text{Co}_{2-x}\text{Mn}_x\text{O}_6$ ($x=0.95$) was determined using neutron powder diffraction. The possible magnetic structures (including those with ab -plane components) were constructed using the magnetic symmetry analysis, and the diffraction data were refined using the FULLPROF program package [26]. The spins point along the c axis, as indicated by the absence of (003) magnetic peak, and the structure is of the $\uparrow\uparrow\downarrow\downarrow$ type. The accuracy of the final refinement result was independently estimated by the Simulated Annealing process, which shows that the deviation of the spins from the c axis cannot exceed 3° . The refinement results for $T=1.4$ K are shown in FIG. III. 6: good agreement factors, $\chi^2=1.44$, $R_B=2.4 \%$, $R_f=2.7 \%$, and $R_{mag}=9.8 \%$, are obtained. The obtained three-

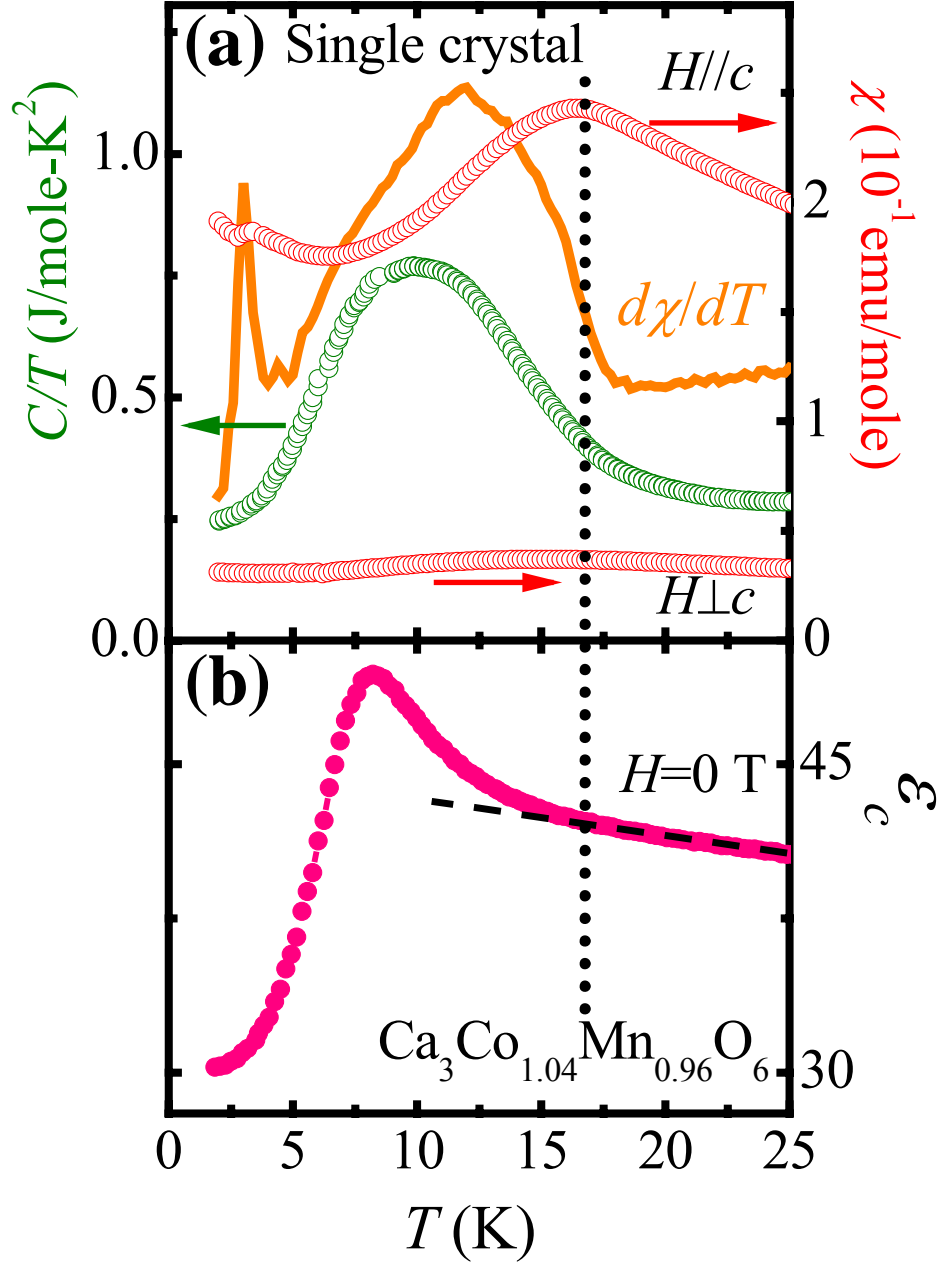


FIG. III. 4. (a) Temperature dependence of magnetic susceptibility, $\chi(T)=M/H$, measured in an applied magnetic field $H=0.2$ T along and perpendicular to the chain direction. The temperature derivative $d\chi/dT$, and zero-field heat capacity (C/T) are also shown. (b) The c -axis dielectric constant, ϵ_c . Dashed line shows the high-temperature behavior of ϵ_c .

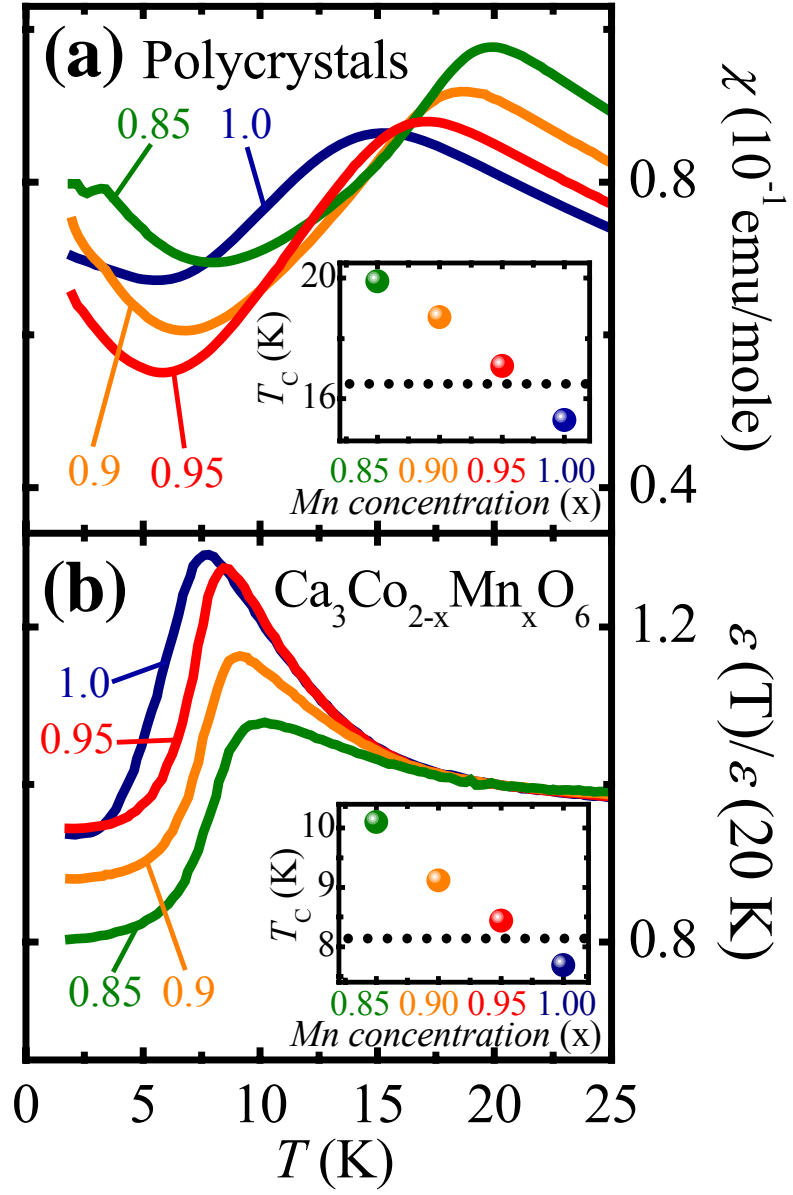


FIG. III. 5. (a) $\chi(T)$ of polycrystalline $\text{Ca}_3\text{Co}_{1-x}\text{Mn}_x\text{O}_6$ for $H=0.2$ T. (b) $\epsilon(T)$ of polycrystalline $\text{Ca}_3\text{Co}_{1-x}\text{Mn}_x\text{O}_6$ for $H=0$, normalized at $T=20$ K. The insets in (a) and (b) show peak positions of $\chi(T)$ and $\epsilon(T)$, respectively, for different Mn concentrations. The dashed lines indicate the corresponding peak positions in the $x=0.96$ single crystal.

dimensional magnetic structure is shown in the inset in FIG. III. 6. In agreement with [24], the Mn ions occupy the octahedral sites. The ordered magnetic moments of Co and Mn ions are $0.66(3) \mu_B$ and $1.93(3) \mu_B$, respectively, and the estimated valences of the cations from Bond-Valence calculation are 1.814(2) for Co and 3.997(3) for Mn. Thus, the magnetic chains consist of alternating low-spin Co^{2+} and high-spin Mn^{4+} ions. Combined with the $\uparrow\uparrow\downarrow\downarrow$ spin order, this makes $\text{Ca}_3(\text{Co,Mn})_2\text{O}_6$ an experimental realization of the magnetoelectric model system described above. In the unit cell shown in FIG. III. 6, all the chains possess the same polarization direction according to this model. We note that the (101) magnetic peak appears to be slightly broadened (see the inset in FIG. III. 6. This indicates that the magnetic order is not truly long-ranged. Measurements on yet unavailable large single crystals are needed to determine the magnetic correlation length with any adequate precision. On warming to $T=8$ K, no qualitative changes are observed in the magnetic structure, and no magnetic order is present at $T=20$ K.

While the magnetic origin of the ferroelectricity, and its description in the framework of the $\uparrow\uparrow\downarrow\downarrow$ chain with alternating ions, are established by the above data, the temperature dependences of both the electric and the magnetic properties are rather complicated. To gain insight into this complexity, we have measured temperature-dependent AC magnetic susceptibility in the $x=0.96$ single crystal. FIG. III.7 (a) and (b) reveal that both of the magnetic temperature anomalies (peaks) exhibit strong frequency indicative of magnetic freezing, which may range from simple superparamagnetism to complex spin-glass transition [27]. As shown in the inset in FIG. III. 7(a), the lower-temperature peak T_{max} of $\chi'(T)$ exhibits the Arrhenius behavior, $f=f_0\exp[-E_a/k_B T_{max}]$, with

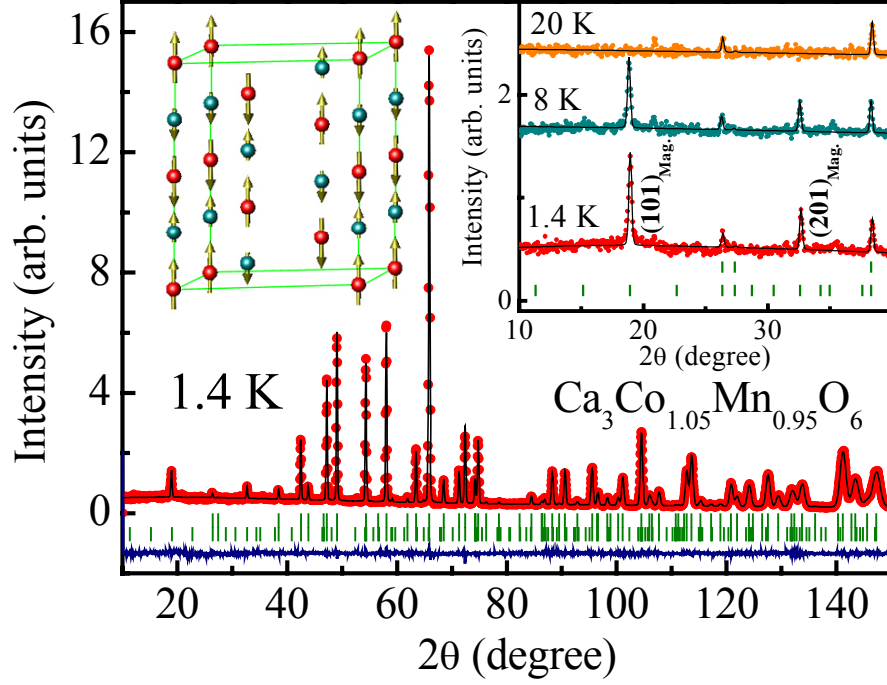


FIG. III. 6. Observed (symbols) and calculated (line) powder neutron diffraction patterns for polycrystalline $\text{Ca}_3\text{Co}_{1-x}\text{Mn}_x\text{O}_6$ ($x=0.95$) for $T=1.4$ K. The first row of bars below the diffraction pattern indicates the positions of the nuclear Bragg peaks and the second row depicts the locations of the magnetic Bragg peaks. The blue line shows the difference between the observed and calculated diffraction patterns. The insets show the low-angle patterns for $T=1.4$ K, 8 K and 20 K, and the refined spin structure.

physically reasonable values of the activation energy, $E_a/k_B \approx 60$ K, and $f_0 \approx 60$ MHz [27]. This behavior with $E_a/T_{max} \approx 20$, together with the numerical value of the slope parameter $\Delta T_{max}/T_{max} \Delta \ln[f]$ of 0.21, signals superparamagnetic blocking (freezing of poorly-correlated magnetic clusters) at low temperatures [27]. The behavior of the higher-temperature anomaly, associated with the magnetic ordering transition, is more complicated. For example, T_{max} (>16 K) of $\chi'(T)$ does not exhibit the simple Arrhenius behavior (see the inset of FIG. III. 7(a)). The data of FIG. III. 7, combined with the neutron data, show that only finite-size magnetic domains develop at the magnetic transition, and that these domains exhibit an additional freezing at a lower temperature. This behavior deserves further investigation since it is likely related to the one dimensionality of the magnetic chains and the geometrical frustration in the *ab*-plane triangular lattice.

While complicated, the observed magnetic behavior provides a consistent explanation of the unconventional temperature dependence of the electric polarization in FIG. III. 3. Magnetic disorder and freezing naturally lead to the corresponding phenomena for the ferroelectric properties in our system. Local clusters exhibiting the two different variants of the spin order shown in FIG. III. 1 give rise to the opposite electrical polarization vectors. Thus, on warming from 2 K, the frozen poled magnetoelectric domains should quickly become dynamic, leading to decreased macroscopic polarization. This is consistent with the rapid reduction of the polarization with increasing temperature. An additional confirmation of this scenario is obtained by observation of thermal history effects, which are characteristic to frozen states. As shown in FIG. III. 3, the polarization of the system poled on cooling down to $T=2$ K (filled

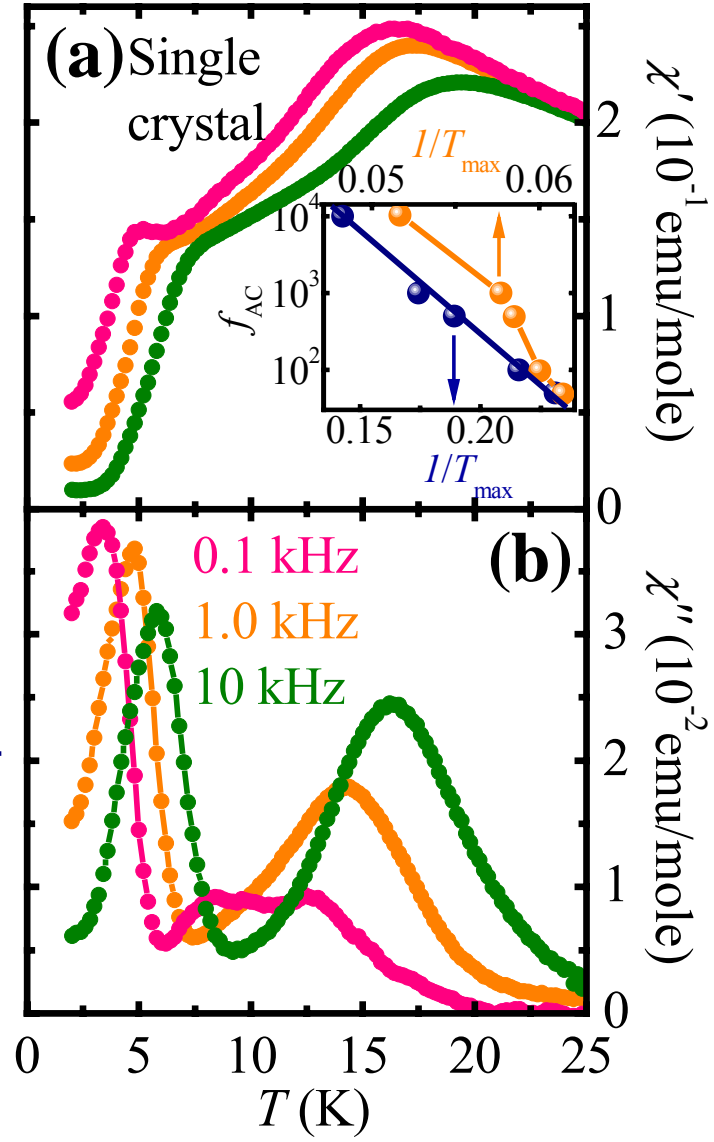


FIG. III. 7. (a) and (b) Real and imaginary parts of the AC susceptibility, $\chi'(T)$ and $\chi''(T)$, of the $x=0.96$ single crystal. The AC magnetic field is 5 Oe, and the frequencies are 0.1, 1 and 10 kHz, as shown. The inset in (a) shows $\log[f]$ vs. inverse temperature for the peak-like features of χ' . The low-temperature feature is shown with blue dots, and the high-temperature feature with orange dots.

circles) significantly exceeds the polarization of the sample poled at $T=3.1$ K (open circles), when the polarization is subsequently measured on warming in zero field. This is a typical behavior of a frozen system undergoing slow relaxation processes. This scenario is also consistent with the absence of any sharp anomaly of $\epsilon_c(T)$ at the magnetic transition. We conclude, therefore, that in $\text{Ca}_3(\text{Co,Mn})_2\text{O}_6$, thermal fluctuations of the magnetoelectric clusters tend to suppress the macroscopic polarization, leading to the complex temperature dependences and thermal history effects observed in the experiments.

The latest investigation by using Monte Carlo Simulation, based on simple 1D elastic Ising model, has remarkably recovered our experimental results as shown in FIG. III. 8 [28]. This qualitative coincidence between theoretical and experimental results confirms that $\uparrow\uparrow\downarrow\downarrow$ spin configuration along with alternating magnetic ions is a real driver for ferroelectricity in the Ising chain magnet of $\text{Ca}_3(\text{Co,Mn})_2\text{O}_6$. In addition, recent study with magnetic fields up to 33 T has shown that the field induced transition from $\uparrow\uparrow\downarrow\downarrow$ to $\uparrow\uparrow\uparrow\downarrow$ spin configurations leads to complete suppression of ferroelectric polarization [29]. $M(H)$ exhibits two successive metamagnetic transitions as shown in FIG. III. 9(a). The first plateau above 10 T with $\sim 3 \mu_B/\text{f.u.}$ corresponds to a fully polarized spin state of Mn^{4+} ions, i.e. $\uparrow\uparrow\uparrow\downarrow$ spin configurations. In this spin configuration with alternating two magnetic ions, inversion symmetry, broken in $\uparrow\uparrow\downarrow\downarrow$ spin state, is restored and electric polarization driven by symmetric exchange striction totally disappears, evident both in $P(H)$ and $P(T)$ (FIG. III. 9(a) and (b)). The other plateau above 25 T at $\sim 4 \mu_B/\text{f.u.}$ indicates fully saturated magnetic state for low-spin Co^{2+} and high-spin Mn^{4+} moments. Note that magnetic hysteresis only appears between $\uparrow\uparrow\downarrow\downarrow$ and

$\uparrow\uparrow\uparrow\downarrow$ states (below 15 T), suggesting intriguing coupling between frustrated spin state in Ising chains and geometrically frustrated magnetic state through inter-chains.

In summary, we report discovery of an unambiguous example of magnetism-driven ferroelectricity with a collinear magnetic order in the Ising chain magnet $\text{Ca}_3\text{Co}_{2-x}\text{Mn}_x\text{O}_6$ ($x \approx 0.96$). The ferroelectricity originates from the simultaneous presence of the alternating order of Co and Mn ions and the spin order with the $\uparrow\uparrow\downarrow\downarrow$ configuration. This provides the first experimental realization of theoretically predicted ferroelectricity in a frustrated Ising chain with an ionic order. Unlike in well-known spiral magnetoelectrics, symmetric exchange striction is expected to drive the ferroelectricity in this system.

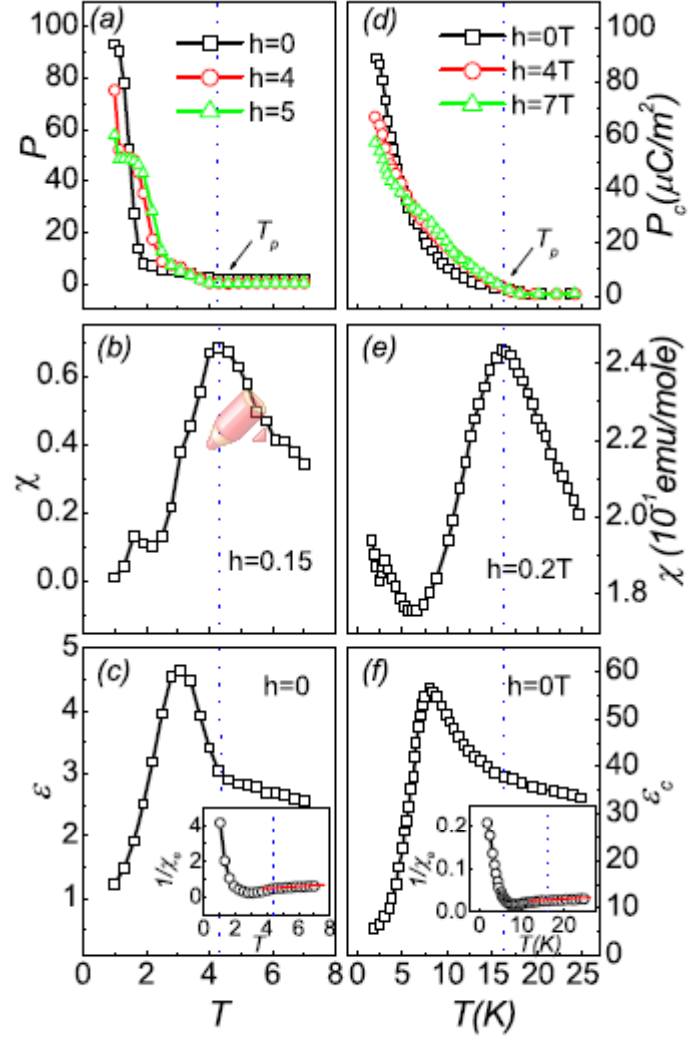


FIG. III. 8. Comparison between theoretical [28] and experimental results: (a), (b), and (c) T dependence of P , χ , and ϵ along the c -axis, produced by Monte Carlo Simulation. (d), (e), and (f) Corresponding experimental data.

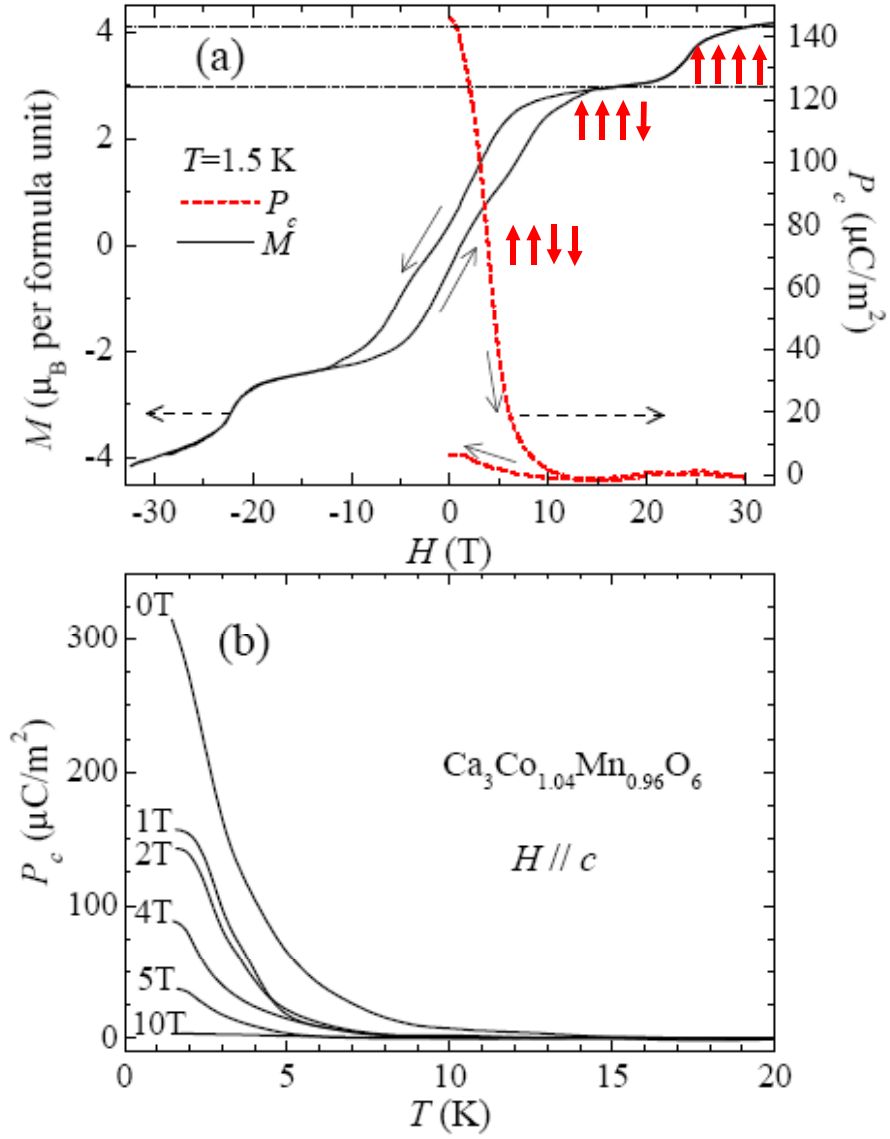


FIG. III. 9. (a) H dependence of magnetization and electric polarization along the c -axis at 1.5 and 1.4 K, respectively. The $0 \mu_B$ state in magnetization corresponds to $\uparrow\uparrow\downarrow\downarrow$ along with spontaneous ferroelectric polarization, $3 \mu_B$ to $\uparrow\uparrow\uparrow\downarrow$ with suppression of polarization and $4 \mu_B$ to $\uparrow\uparrow\uparrow\uparrow$ [29]. (b) T dependent polarization ($P//c$) in various magnetic fields ($H//c$). The polarization completely disappears above 10 T [29].

4. REFERENCES

- [1] D. I. Khomskii, J. Magn. Magn. Mater. **306**, 1 (2006).
- [2] S-W. Cheong and M. Mostovoy, Nature Mater. **6**, 13 (2007).
- [3] N. Hur *et al.*, Nature **429**, 392 (2004).
- [4] T. Goto *et al.*, Phys. Rev. Lett. **92**, 257201 (2004).
- [5] N. Hur *et al.*, Phys. Rev. Lett. **93**, 107207 (2004).
- [6] T. Kimura *et al.*, Nature **426**, 55 (2003).
- [7] G. Lawes *et al.*, Phys. Rev. Lett. **95**, 087205 (2005).
- [8] T. Kimura *et al.*, Phys. Rev. B **73**, 220401(R) (2006).
- [9] T. Kimura *et al.*, Phys. Rev. Lett. **94**, 137201 (2005).
- [10] Y. Yamasaki *et al.*, Phys. Rev. Lett. **96**, 207204 (2006).
- [11] K. Taniguchi *et al.*, Phys. Rev. Lett. **97**, 097203 (2006).
- [12] S. Park *et al.*, Phys. Rev. Lett. **98**, 057601 (2007).
- [13] H. Katsura *et al.*, Phys. Rev. Lett. **95**, 057205 (2005).
- [14] M. Mostovoy, Phys. Rev. Lett. **96**, 067601 (2006).
- [15] I.A. Sergienko, and E. Dagotto, Phys. Rev. B **73**, 094434 (2006).
- [16] A. B. Harris *et al.*, Phys. Rev. B **73**, 184433 (2006).
- [17] L. C. Chapon *et al.*, Phys. Rev. Lett. **96**, 097601 (2006).
- [18] Y. Noda *et al.*, Physica B **385-386**, 119 (2006).
- [19] H. Kimura *et al.*, J. Phys. Soc. Jpn. **75**, 113701-1 (2006).
- [20] I. A. Sergienko *et al.*, Phys. Rev. Lett. **97**, 227204 (2006).
- [21] B. Lorentz *et al.*, Phys. Rev. B **76**, 104405 (2007).
- [22] M. E. Fisher and W. Selke, Phys. Rev. Lett. **44**, 1502 (1980).

- [23] S. Rayaprol *et al.*, Sol. Stat. Comm. **128**, 79 (2003).
- [24] V. G. Zubkov *et al.*, J. of Sol. Stat. Chem. **160**, 293 (2001).
- [25] A. Maignan *et al.*, Eur. Phys. J. B, **15**, 657 (2000).
- [26] J. Rodriguez-Carvajal, Physica B **192**, 55 (1993).
- [27] J. A. Mydosh, *Spin Glasses. An Experimental Introduction*. (Taylor & Francis, London, 1993).
- [28] X. Yao and V. C. Lo, J. Appl. Phys. **104**, 083919 (2008).
- [29] Y. J. Jo *et al.*, Phys. Rev. B **79**(1), 012407 (2009).

Chapter IV

Multiferroicity in the square-lattice antiferromagnet of $\text{Ba}_2\text{CoGe}_2\text{O}_7$

1. Introduction

The recent renaissance of the research on multiferroics, where magnetic order and ferroelectricity coexist, has been invigorated by scientific discoveries of significant cross-coupling between spin and lattice degrees of freedom as well as potentials for device applications such as ferroelectric memory tunable by magnetic fields or magnetic memory controlled by electric fields [1-5]. The remarkable cross-coupling effects in multiferroics include reversible flipping of ferroelectric polarization or drastic changes of dielectric constant with applied magnetic fields [4-6]. These recently discovered effects have been observed in the so-called “magnetism-driven ferroelectrics”. Magnetic order is developed with the loss of inversion symmetry on the magnetic lattice. The lattice relaxation occurs through exchange striction in the magnetically ordered state and thus the crystallographic lattice naturally loses inversion symmetry. Ferroelectricity is developed by this mechanism in magnetism-driven ferroelectrics. Spiral magnetic order, resulting from magnetic frustration, is a common way to induce the loss of magnetic inversion symmetry, and magnetism-driven ferroelectricity has been, indeed, observed in a number of spiral magnets such as TbMnO_3 , $\text{Ni}_3\text{V}_2\text{O}_8$, MnWO_4 , CuFeO_2 , CoCr_2O_4 and LiCu_2O_2 [4, 7-12]. Note that the “antisymmetric” part of exchange coupling, known as the Dzyaloshinski-Moriya (DM) interaction, becomes active when ferroelectricity is induced by spiral magnetic order in non-collinear magnets. Alternatively, ferroelectricity can result from lattice relaxation through exchange striction associated with the “symmetric” part of the exchange coupling. This kind of multiferroicity has been found in Ising magnets such as $\text{Ca}_3(\text{Co,Mn})_2\text{O}_6$ [13].

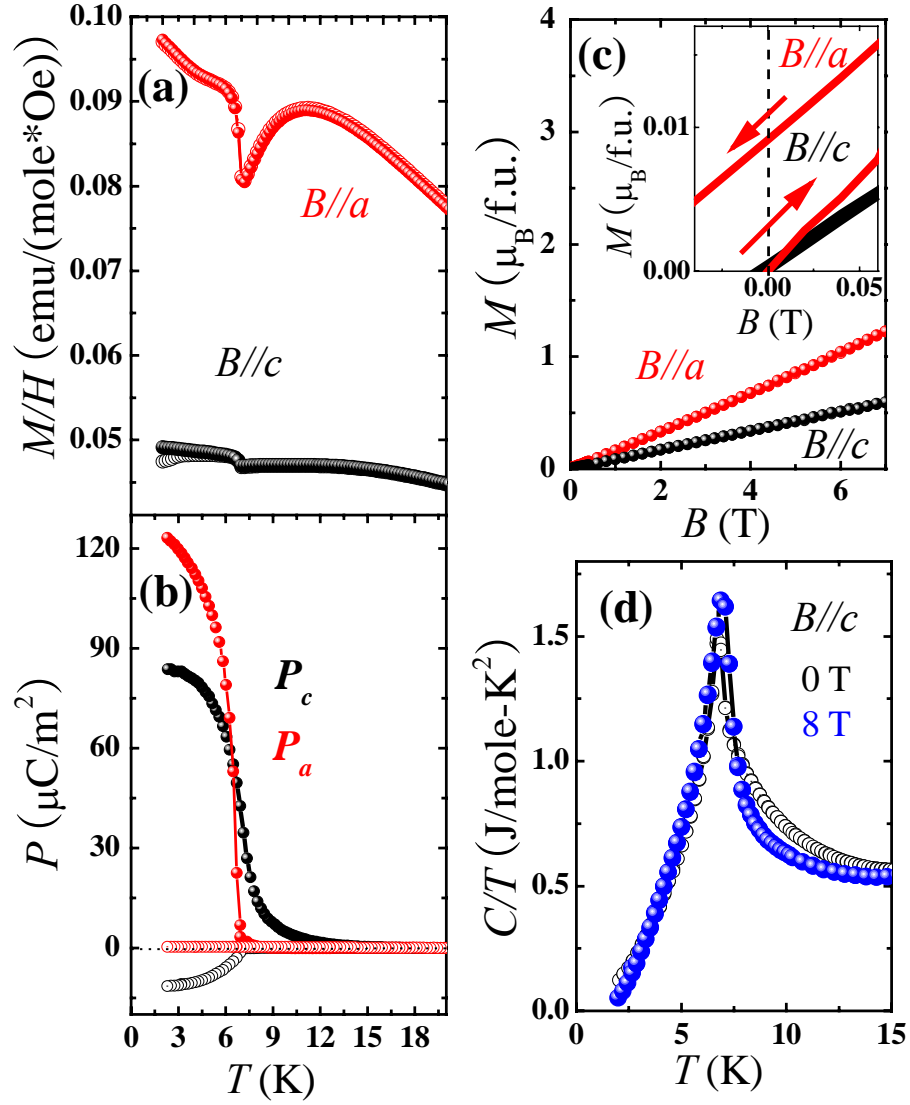


FIG. IV. 1. (a) Temperature dependence of magnetic susceptibility measured in 0.2 T applied along the c axis (black) and the a axis (red): open and filled circles represent zero-field-cooled (ZFC) and field-cooled (FC) data, respectively. (b) Temperature dependence of polarization along the a (red) and c (black) axes in $B=0$ (open circle) and $B=8$ T (filled circle). (c) Magnetization ($\mu_B/\text{f.u.}$ (formula unit)) at 2 K in fields along the c (black) and a (red) axes: a magnified figure near $B=0$ is shown in the inset. (d) The temperature dependence of specific heat divided by temperature in $B=0$ (black) and 8 T (blue).

2. Experimental Method

A single crystal of $\text{Ba}_2\text{CoGe}_2\text{O}_7$ (6 mm in diameter and 50 mm in length) was grown using a floating zone method. For the feed rods, a solid-state reaction method was employed in air. DC magnetization was measured using a SQUID magnetometer: the Quantum Design MPMS. We measured specific heat using the standard relaxation method with the Quantum Design PPMS. The experiments for dielectric constant (ϵ) on polished crystals ($4.2 \times 3.5 \text{ mm}^2$ in the a - b plane by 0.306 mm along the c axis for the c -direction measurement, and $3.2 \times 2.4 \text{ mm}^2$ the b - c plane by 0.324 mm along the a axes for the a direction measurement) were performed using an LCR meter at 44 KHz. The pyroelectric current to obtain polarization was measured with an electrometer during a warming process (at a rate of 4 K/min) after poling samples from 40 K to 2 K in the electric field of $\sim 7 \text{ kV/cm}$.

3. Result and Discussion: Bulk composite

The compound $\text{Ba}_2\text{CoGe}_2\text{O}_7$ crystallizes in a tetragonal structure with a square magnetic lattice. The crystal structure of $\text{Ba}_2\text{CoGe}_2\text{O}_7$ is characterized as a $\bar{p}4_2m$ crystallographic space group with a unit cell of $a=b=0.8410 \text{ nm}$ and $c=0.5537 \text{ nm}$ at 10 K [14]. However, the magnetic ground state of $\text{Ba}_2\text{CoGe}_2\text{O}_7$ is concluded as an in-planar antiferromagnetic order below the Neel temperature of $T_N=6.7 \text{ K}$ [14, 15]. It has been postulated that the DM vector in $\text{Ba}_2\text{CoGe}_2\text{O}_7$ alternates its direction along [001], resulting in the in-planar antiferromagnetic order with an in-plane weak ferromagnetic component [16]. Neutron scattering results on $\text{Ba}_2\text{CoGe}_2\text{O}_7$ suggest the presence of

commensurate and collinear magnetic order with spins antiferromagnetically pointing along the b axis [14]. The presence of two-types of DM vectors in the square-lattice antiferromagnets suggests that the system can be an intriguing candidate for multiferroicity. Indeed, we discovered that ferroelectric polarization develops below T_N of $\text{Ba}_2\text{CoGe}_2\text{O}_7$, and exhibits a remarkable increase in magnitude as well as a smooth rotation of direction with external magnetic fields.

Magnetization (M) behavior of our crystal is consistent with the results in literature [14]. FIG. IV. 1(a) shows the zero-field-cooled (ZFC) and field-cooled (FC) magnetization curves in $B=0.2$ T (parallel to the c and a axes). A sharp step appears at 6.7 K (T_N) with a significant magnetic anisotropy. The large M/B (magnetization/external magnetic field) along the tetragonal a axis indicates that the system is an easy-planar magnet. The step-like increase of M/B along the a axis below T_N , much larger than that along the c axis, suggests the appearance of a weak ferromagnetic moment, predominantly, in the a - b plane. As shown in the FIG. IV. 1(c), Magnetization ($\mu_B/\text{f.u.}$ (formula unit)) increases linearly with increasing external magnetic field, B . However, the residual magnetization extrapolated to $B=0$ is found to be non-zero; about $0.009 \mu_B/\text{f.u.}$ and $0.0005 \mu_B/\text{f.u.}$ at 2 K along the a and c axes, respectively as shown in the inset figure of FIG. IV. 1(c). This result is consistent with the behavior of the step-like M/B increase below T_N , in FIG. IV. 1(a). This residual moment, mostly along the a axis, may be consistent with the presence of the [001]-direction DM vector.

We discovered that the magnetic transition accompanies the appearance of electric polarization (P). The temperature (T) dependences of P along the c axis (P_c) and along the a -axis (P_a) in $B_c=0$ (open circles) and $B_c=8$ T (filled circles) are shown in FIG.

IV. 1(b). The magnitude of P_c is $\sim 11 \mu\text{C}/\text{m}^2$ in $B_c=0$ and $\sim 80 \mu\text{C}/\text{m}^2$ in 8 T, while the P_a value changes from $\sim 0 \mu\text{C}/\text{m}^2$ to $\sim 120 \mu\text{C}/\text{m}^2$ in $B_c=0$ and 8 T, respectively. A small electric polarization exists only along the c axis in $B_c=0$. In 8 T, a large polarization appears in both a and c axes. Note that the negative sign of the small polarization in $B_c=0$ may suggest the presence of unusual pinning of ferroelectric domains during the poling process. A sharp peak in specific heat curve (C/T vs T) is observed at T_N and changes little with $B_c=8$ T, as shown in the inset FIG. IV. 1(d).

The details of the external magnetic field along c axis (B_c)-dependent dielectric properties of $\text{Ba}_2\text{CoGe}_2\text{O}_7$ are shown in FIG. IV. 2. The T dependence of dielectric constants along the c axis, ϵ_c , and along the a axis, ϵ_a , in various B_c is displayed in FIG. IV. 2(a) and (b), respectively. With decreasing temperature, ϵ_c in $B_c=0$ sharply increases below T_N , and tends to saturate at low temperatures. The temperature-induced change of ϵ_c decreases with increasing B_c , and becomes only $\sim 0.24\%$ in $B_c=8$ T. On the other hand, ϵ_a does not show any anomaly at T_N in $B=0$, but in $B_c>0$, a sharp ϵ_a peak appears at T_N , and the magnitude of the peak increases with increasing B_c . Consistent with earlier discussion, polarization along c axis in $B_c=0$ shows non-zero value but small below T_N , and is enhanced smoothly with increasing external magnetic field, FIG. IV. 2(c). Polarization along a axis is zero in $B_c=0$, but increases smoothly with increasing B_c ,

FIG. IV. 3(a) and (c) show the isothermal change of P_a and P_c with varying B_c at 2 K. The measurement was made with three sequential procedures; $B_c=0$ to 8 T (route 1; red), 8 T to -8 T (route 2; black), and -8 T to 8 T (route 3; blue). The simultaneous presence of non-zero P_a and P_c in finite indicates that the true electric polarization vector lies on the a - c plane, but away from the c axis. The external magnetic field along c axis

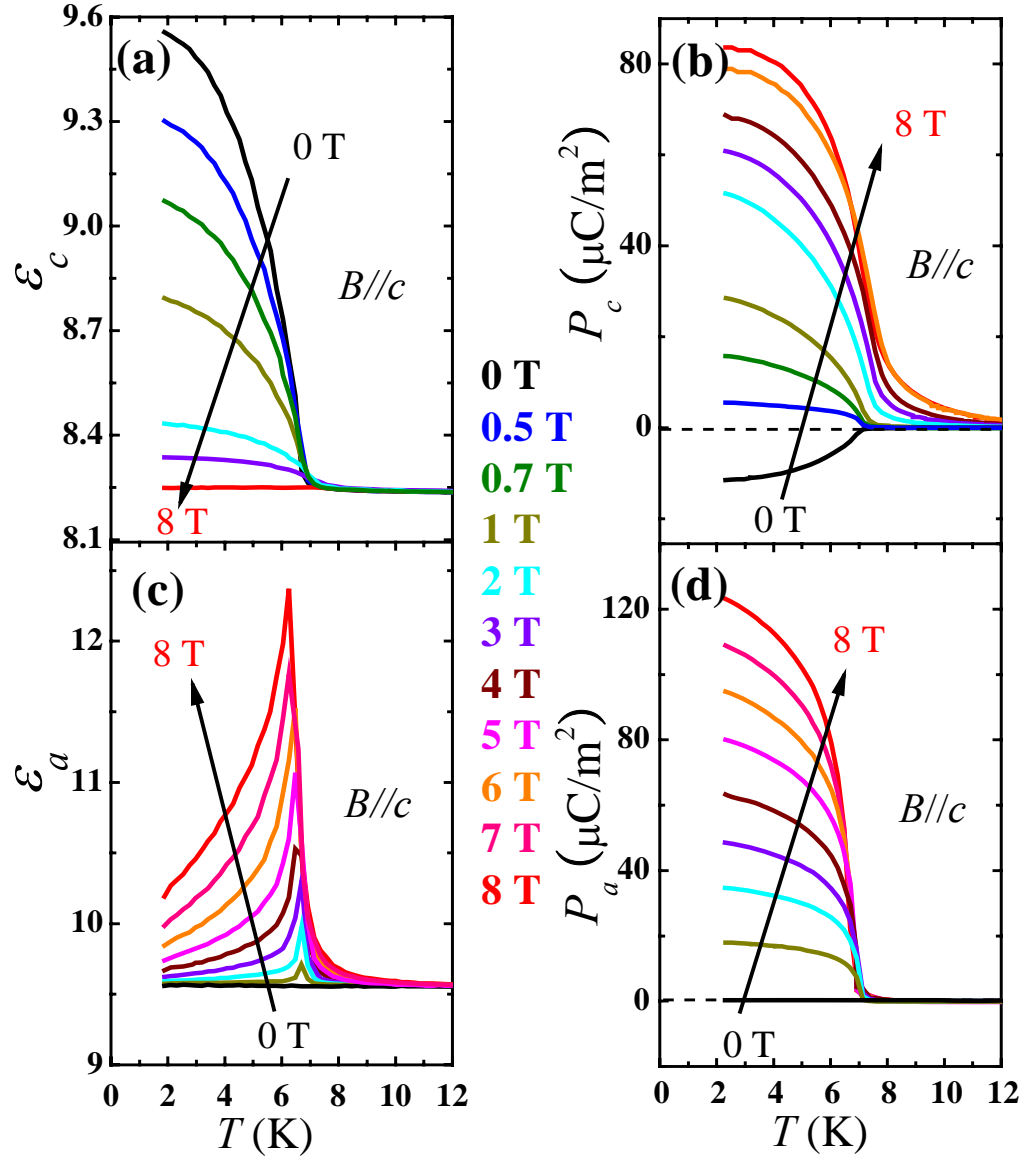


FIG. IV. 2. (a), (b), (c), and (d) Temperature dependences of the c -direction dielectric constant, the a -direction dielectric constant, the c -direction polarization, and the a -direction polarization in various applied magnetic fields ($B=0$ to 8 T) along the c axis.

dependence of the polarization vector for route 1 is displayed in FIG. IV. 4. With increasing B_c , polarization value increases and at the same time rotates smoothly away from the c axis. Note that P_a keeps increasing with increasing B_c up to our maximum measuring field of 8 T, while the increase of P_c tends to saturate for $B_c > \sim 2$ T. This polarization behavior corroborates with the external magnetic field dependence of ε_c and ε_a , shown in FIG. IV. 3(b) and (d): ε_c at 2 K changes sharply in low B_c , but saturates for $B_c > \sim 2$ T, but ε_a at 2 K keeps changing in the entire range of external magnetic field up to 8 T. Note that we have not observed any significant change of dielectric properties in $\text{Ba}_2\text{CoGe}_2\text{O}_7$ when magnetic fields were applied along the a or b axis.

We emphasize that the smooth rotation of polarization with external magnetic fields in $\text{Ba}_2\text{CoGe}_2\text{O}_7$, summarized in FIG. IV. 4, is rather unique. In other magnetism-driven multiferroics, Electric polarization tends to flip suddenly by 90° (TbMnO_3 , DyMnO_3 , MnWO_4 and LiCu_2O_2) or 180° (TbMn_2O_5) through 1st-order phase transitions when sufficiently-large magnetic fields are applied [3-5, 7-9]. $M(B)$ curves of $\text{Ba}_2\text{CoGe}_2\text{O}_7$, FIG. IV. 1(c), do not show any hint of a external magnetic field -induced phase transition. In addition, there exists no hint of any 1st-order phase transition in the external magnetic field dependence of P_c , ε_a , and ε_c . This unique behavior may be related with the possible presence of two types of the DM vectors in the square-lattice structure of $\text{Ba}_2\text{CoGe}_2\text{O}_7$; one along $[\bar{1}10]$ and the other along $[001]$. Detailed investigation of the exact magnetic structure in external magnetic field will be needed to unveil the origin of the intriguing multiferroic behavior in $\text{Ba}_2\text{CoGe}_2\text{O}_7$.

It is also noteworthy that there exists little hysteresis in the external magnetic field-dependence of P_c , ε_a , and ε_c (except P_a : the hysteretic behavior of P_a with external

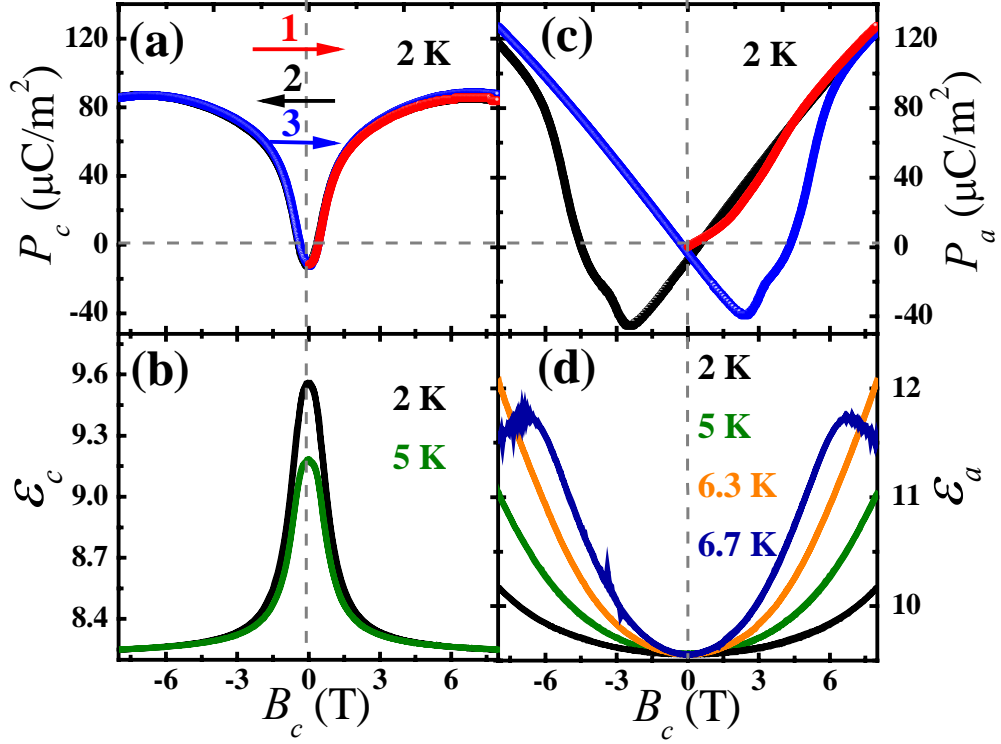


FIG. IV. 3. (a) External magnetic field dependence of the c -direction polarization at 2 K: red, black and blue lines are obtained from measurements with field sweeps from $B=0$ to 8 T, 8 T to -8 T, and -8 T to 8 T, respectively. (b) External magnetic field dependence of the c -direction dielectric constants at 2 K (black) and 5 K (green). (c) B_c dependence of the a -direction polarization at 2 K: red, black and blue lines are obtained from measurements with field sweeps from 0 to 8 T, 8 T to -8 T, and -8 T to 8 T, respectively. (d) B_c dependence of the a -direction dielectric constants at 2 K (black), 5 K (green), 6.3 K (orange) and 6.7 K (blue). All data in (b-e) show the results for the entire B_c sweeps from $0 \rightarrow 8 \text{ T} \rightarrow -8 \text{ T} \rightarrow 8 \text{ T}$.

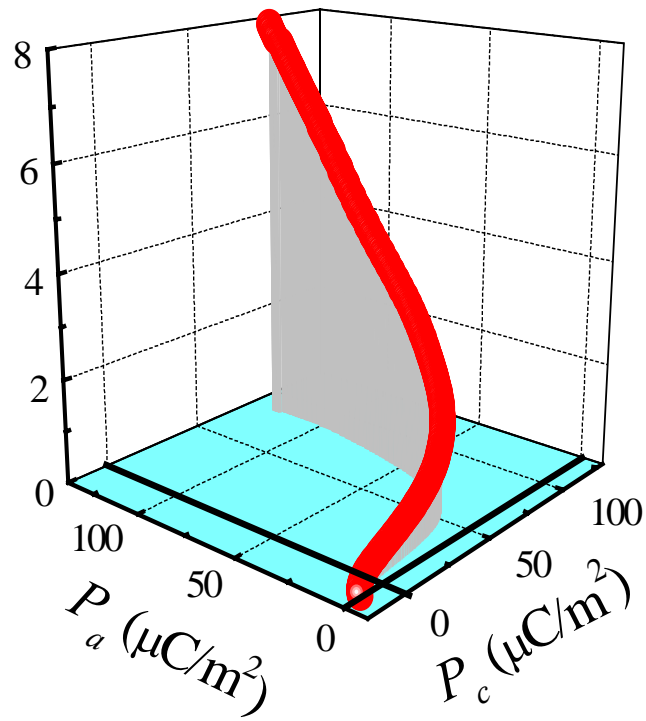


FIG. IV. 4. Variation of polarization vector with magnetic fields ($B_c=0-8$ T) along the c axis. This plot is obtained from results in FIG. IV. 3(a) and (c).

magnetic field may be related with ferroelectric domain pinning, rather than a 1st-order phase transition) (see FIG. IV. 3(a)-(d)). The external magnetic field-induced change of dielectric properties in multiferroics can be of use for technological devices, but a large field hysteresis can be detrimental for many applications. Since the drastic control of polarization and dielectric constant with external magnetic field in many multiferroics occurs through 1st-order phase transitions, a large field hysteresis is commonly accompanied. However, the field hysteresis of the external magnetic field-induced change of P_c , ε_a , and ε_c in $\text{Ba}_2\text{CoGe}_2\text{O}_7$ appears to be minimal: the hysteretic variation, defined as the change of polarization or dielectric constant with different field sweeps normalized by the difference of P or ε in $B_c=0$ and 8 T, is less than 1.04 % for ε_a , (<1.12 % for ε_c and <3.7 % for P_c)

In summary, we found that ferroelectricity develops below T_N in $\text{Ba}_2\text{CoGe}_2\text{O}_7$, and ferroelectric polarization is along the tetragonal c axis. The polarization increases significantly in magnitude and rotates away from the c axis when magnetic fields are applied along the c axis. This change of polarization and the associated change of dielectric constant with fields are smooth without going through any phase transition, and thus is involved with little field hysteresis. Exploration of this negligible external magnetic field-hysteresis effect will be indispensable towards the practical potential of multiferroics.

4. REFERENCES

- [1] S.-W. Cheong and M. Mostovoy, *Nat. Mater.* **6**, 13 (2007).
- [2] D. I. Khomskii, *J. Magn. Magn. Mater.* **306**, 1 (2006).
- [3] T. Goto, T. Kimura, G. Lawes, A. P. Tamires, and Y. Tokura, *Phys. Rev. Lett.* **92**, 257201 (2004).
- [4] T. Kimura, T. Goto, H. Shintani, K. Ishizaka, T. Arima, and Y. Tokura, *Nature (London)* **426**, 55 (2003).
- [5] N. Hur, S. Park, P. A. Sharma, J. S. Ahn, S. Guha, and S.-W. Cheong, *Nature (London)* **429**, 392 (2004).
- [6] N. Hur, S. Park, P. A. Sharma, S. Guha, and S.-W. Cheong, *Phys. Rev. Lett.* **93**, 107207 (2004).
- [7] T. Arima, A. Tokunaga, T. Goto, H. Kimura, Y. Noda, and Y. Tokura, *Phys. Rev. Lett.* **96**, 097202 (2006).
- [8] S. Park Y. J. Choi, C. L. Zhang, and S.-W. Cheong, *Phys. Rev. Lett.* **98**, 057601 (2007).
- [9] K. Taniguchi, N. Abe, T. Takenobu, Y. Iwasa, and T. Arima, *Phys. Rev. Lett.* **97**, 097203 (2006).
- [10] G. Lawes, A. B. Harris, T. Kimura, N. Rogado, R. J. Cava, A. Aharony, O. Entin-Wohlman, T. Yildirim, M. Kenzelmann, C. Broholm, and A. P. Ramirez, *Phys. Rev. Lett.* **95**, 087205 (2005).
- [11] T. Kimura, J. C. Lashley, and A. P. Ramirez, *Phys. Rev. B* **73**, 220401(R) (2006).
- [12] Y. Yamasaki, S. Miyasaka, Y. Kaneko, J.-P. He, T. Arima, and Y. Tokura, *Phys. Rev. Lett.* **96**, 207204 (2006).

- [13] Y. J. Choi, H. T. Yi, S. Lee, Q. Huang, V. Kiryukhin, and S.-W. Cheong, Phys. Rev. Lett. **100**, 047601 (2008).
- [14] A. Zheludev, T. Sato, T. Masuda, K. Uchinokura, G. Shirane, and B. Roessli, Phys. Rev. B **68**, 024428 (2003).
- [15] A. N. Bogdanow, U. K. Robler, M. Wolf, and K.-H. Muller, J. Magn. Magn. Mater. **272-276**, 332 (2003).
- [16] T. Sato, T. Masuda, and K. Uchinokura, Physica B **329-333**, 880 (2003).

Chapter V

Conclusion

1. Summary

In recent years, the study of multiferroics has opened a rich vein of new materials, novel phenomena and technological potentials: a number of new multiferroics are found and unprecedented cross-coupling effects such as high tunability of electric polarization with external magnetic fields have been discovered. In chapter I, we have presented the classification of the recently discovered multiferroics and discussed the possible origins of multiferroicity and magnetoelectric effects.

In chapter II, we have investigated unexpected evolution, with thermal and magnetic-field (H) variations, of the inter-relation between the polarization \mathbf{P} , magnetization \mathbf{M} and spiral wave vector \mathbf{Q} in CoCr_2O_4 , which has ferrimagnetic conical-spiral magnetic order. For example, \mathbf{P} suddenly jumps and changes its sign at the magnetic lock-in transition (T_L) with thermal variation, or with isothermal variation of H (without changing its direction) at T_L , which surprisingly occurs without change in spiral handedness (i.e. the sign of \mathbf{Q}). The presence of multiple spiral sublattices may be behind this unusual behavior.

In chapter III, we have presented our discovery of collinear-magnetism-driven ferroelectricity in the Ising chain magnet $\text{Ca}_3\text{Co}_{2-x}\text{Mn}_x\text{O}_6$ ($x \approx 0.96$). Neutron diffraction shows that Co^{2+} and Mn^{4+} ions alternating along the chains exhibit an up-up-down-down ($\uparrow\uparrow\downarrow\downarrow$) magnetic order. The ferroelectricity results from the inversion symmetry breaking in the $\uparrow\uparrow\downarrow\downarrow$ spin chain with an alternating charge order. Unlike in spiral magnetoelectrics where antisymmetric exchange coupling is active, the symmetry breaking in $\text{Ca}_3(\text{Co,Mn})_2\text{O}_6$ occurs through exchange striction associated with symmetric superexchange.

In chapter IV, we have discussed newly-discovered ferroelectricity below the Néel temperature of 6.7 K in the antiferromagnetic $\text{Ba}_2\text{CoGe}_2\text{O}_7$ with square magnetic lattice. The ferroelectric polarization is rather small in magnitude and aligns along the c axis, but its magnitude increases remarkably and its direction smoothly rotates away from the c axis when the magnetic fields are applied along the c axis. This behavior of smooth rotation, rather than sudden flip, of electric polarization is unique and accompanies a linear increase of magnetization and a smooth change of dielectric constant with little hysteresis, which may be important for certain technological applications.

2. A new dimension of multiferroics research

Until recently many known multiferroics, where ferroelectricity originates from magnetic ordering, exhibit highly-controlled ferroelectric polarization and dielectric constant by external magnetic fields. However, there still remains obstacles in the way toward practical application of the materials, such as small magnitudes of polarization, low transition temperatures at which multiferroicity comes in, and insensitive magnetization to applied electric fields.

In magnetism-induced ferroelectricity, ordering temperatures are inherently low because of the competing spin states of frustrated magnets. One exception is the hexagonal ferrite, $\text{Ba}_{0.5}\text{Sr}_{1.5}\text{Zn}_2\text{Fe}_{12}\text{O}_{22}$ [1] where multiferroicity appears even above room temperature. The hexagonal ferrite shows magnetic order at 326 K and ferroelectricity is induced by spiral spin nature under applied magnetic fields. But the ferroelectric polarization has only been measured up to 110 K because the sample becomes conducting at high temperature, making it difficult to align electric dipoles by

electric fields. The latest discovery of high- T ($T_{\text{FE}}=230$ K) magnetism-induced ferroelectricity in CuO therefore provides a new route to progress in multiferroics research [2]. FIG. V. 1(a) shows a diagram of superexchange interaction, J as a function of Cu-O-Cu bond angle, ϕ for various low-dimensional cuprate systems. The compounds with large J associated with ϕ close to 180° show high antiferromagnetic transition temperatures. With decreasing ϕ , J suppresses monotonically and becomes negative (ferromagnetic) at ϕ around 95° . For the recently found multiferroic LiCu_2O_2 , ferromagnetic J competes with higher order antiferromagnetic exchange interaction, leading to spiral magnetic order, i.e. ferroelectricity. However, this happens below 25 K [3]. In CuO, strong J with $\phi=146^\circ$ being intermediate between 90 and 180° induces high magnetic transition temperature (230 K) at which spiral order emerges with competing antiferromagnetic and ferromagnetic interactions maintaining high effective J . CuO undergoes two successive magnetic transitions at 213 K and 230 K and the ferroelectric state forms between two transition temperatures as shown in FIG. V. 1(b). Since the ferroelectric polarization exists in the narrow temperature range, for the pyroelectric current measurement the sample was poled to 220 K (a temperature in ferroelectric state), then the current was measured during the temperature up and down sweeps.

BiFeO_3 is the most extensively studied multiferroic material because it contains a large magnitude of polarization and presence of magnetism at room temperature [4, 5] (BiFeO_3 is a proper ferroelectric and magnetism results from Fe^{3+} ions, see the detail in Chapter I. 2). However, due to its significant current leakage at room temperature, usually considered as a serious problem that deteriorates their functionalities [6, 7], the relationship between electric transport characteristics and ferroelectric polarization has

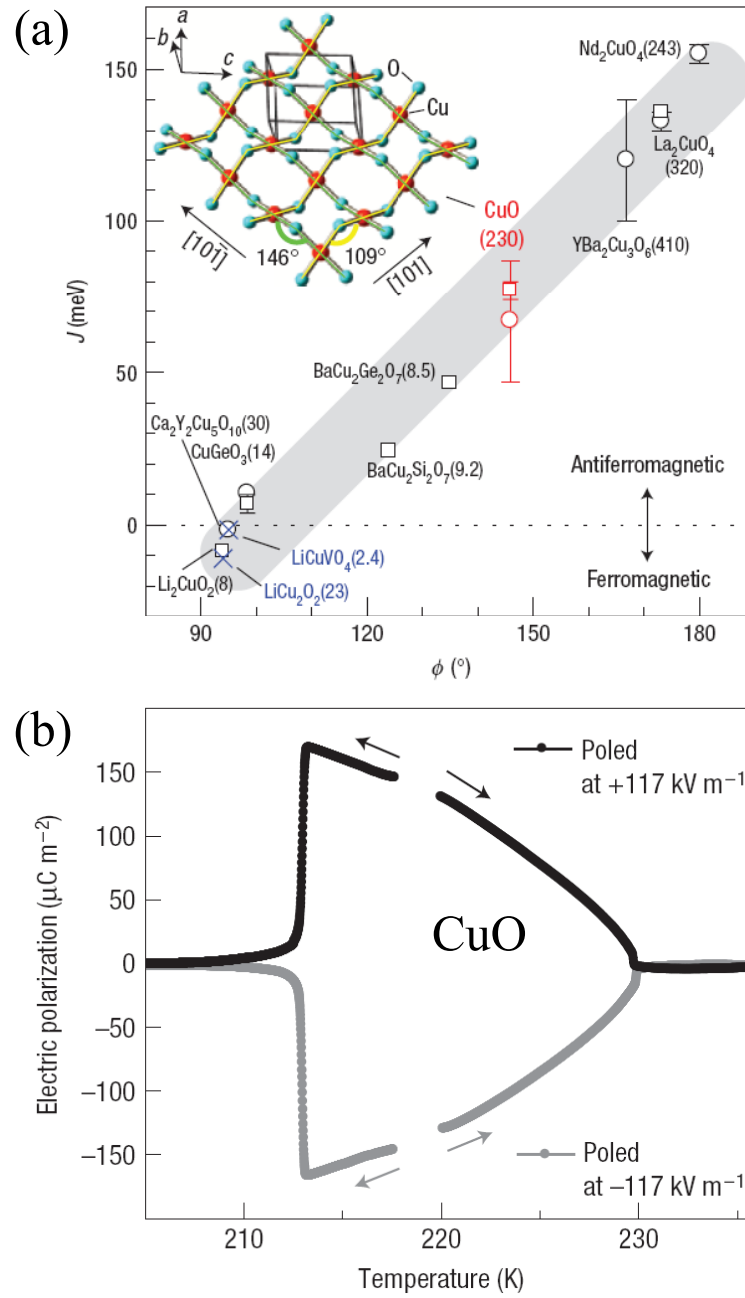


FIG. V. 1. (a) Principal superexchange interaction J as a function of Cu–O–Cu bond angle for various low-dimensional cuprates. CuO (red) has an intermediate magnitude of J among the various cuprates, showing ferroelectricity at high temperature. (b) Electric polarization, which appears at very high temperature (230 K), along the b axis as a function of temperature in a CuO crystal. [3]

been little studied. The recent study of electric transport on large BiFeO₃ single crystals has revealed intriguing charge conduction behavior such as diode-like effects which can be reproducibly switched by large external electric fields, and a significant zero bias photovoltaic effect when the crystal is illuminated with visible light [8]. As shown in FIG. V. 2, there exists significant currents that are non-linear with applied electric field, E , and also seem to show a strong dependence on the direction of E . Note that the magnitude of E here is much less than ferroelectric coercivity, so polarization switching does not occur during the E sweep for current density, J , vs. E curves. The diode forward-reverse directions switch when ferroelectric polarization is uniformly reversed by large electric voltage pulses. When +150 V (E of +17 kV/cm) pulses are applied to the top electrode shown in the FIG. V. 2(a), the ferroelectric polarization points down, as confirmed by piezoresponse force microscopy (PFM) (FIG. V. 2(b)). The electric current through the specimen is large when the current direction is also downward, i.e., the diode forward direction is from top to bottom, and along the polarization direction (FIG. V. 2(c)). When -150 V pulses are applied, ferroelectric polarization switches to the upward direction, and the diode forward direction becomes from bottom to top (still along the polarization direction). Application of +150 V pulses restores the original configuration. Therefore, the diode directions switch whenever ferroelectric polarization is reversed by external pulses, and the diode forward direction is always along the ferroelectric polarization direction (FIG. V. 2(c)). Note that the application of the second set of +150 V pulses does not completely restore the original $J(E)$ curve, and this incomplete restoration may be due to complex factors such as incomplete polarization flipping, formation of conducting paths, or irreversible changes in the interfacial regions. FIG. V. 3(a) and (b) show the

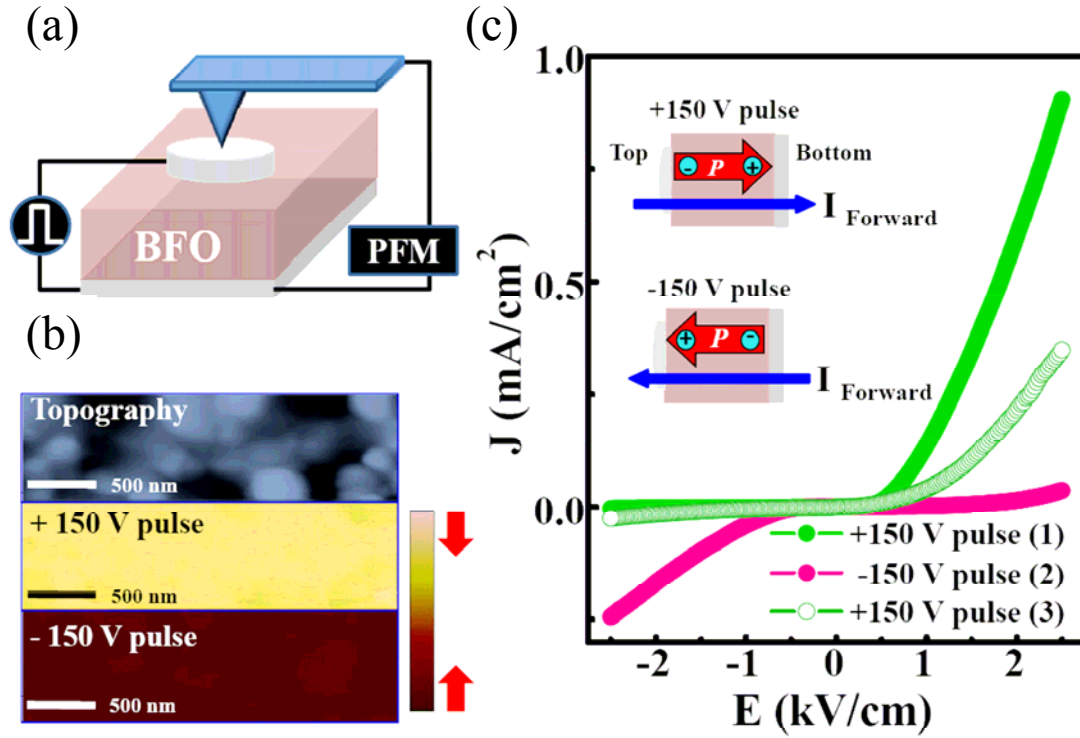


FIG. V. 2. (a) Sketch of the set-up for the simultaneous PFM and $J(E)$ measurements on Ag/BFO/Ag. (b) Topography image and out-of-plane PFM images after ± 150 V pulses. (c) $J(E)$ curves of BFO_3 after +150 V, -150 V and +150 V pulses, in sequence. The diode forward-reverse directions switch when the direction of out-of-plane polarization is reversed by ± 150 V pulses. The diode forward direction turns out to be same with the direction of electric pulses used for polarization flipping. [8]

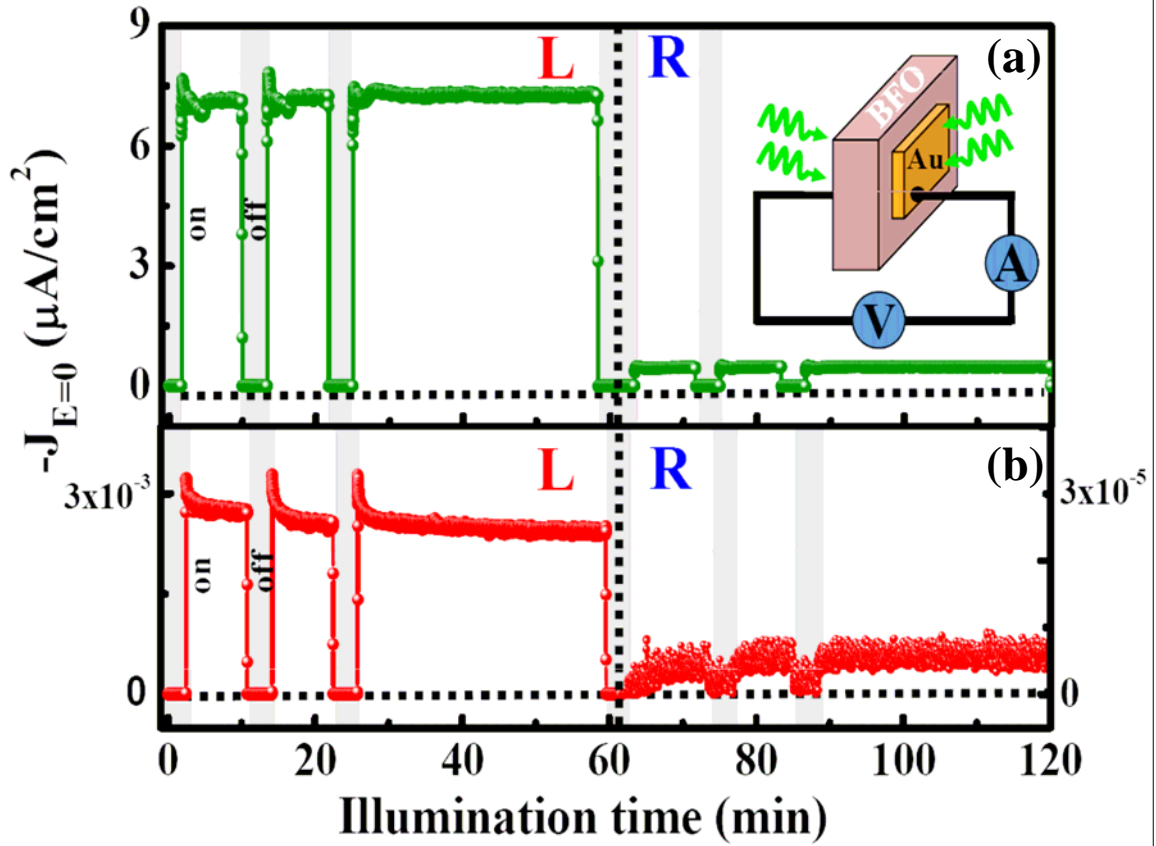


FIG. V. 3. The zero-bias photocurrent density as a function of time with (a) green light ($\lambda=532$ nm) or (b) red light ($\lambda=650$ nm) on or off, shining on the different sides of BFO (a sketch is shown in the inset). The large difference in the magnitude of photocurrent between green and red light illumination indicates that photo-excited carriers across bulk optical gap (~ 2.5 eV) dominate the photovoltaic effect. The observed R/L asymmetry may result from a thermoelectric power effect and/or uncontrolled asymmetries in the experimental configuration. [8]

(a) and a red (b) light on and off. For the first 60 minutes, the left electrode was illuminated and for the next 60 minutes the right electrode was illuminated. Detailed study of these effects with other experimental configurations (e.g., electrodes with different conductors or controlled doping levels) and spectroscopic studies of metal/BFO interfaces will be necessary to unveil the true origin of these intriguing effects.

In spite of the strong magnetic field dependence of electric polarization and dielectric constant in many known spiral magnets, this does not imply the strong effects of electric fields on magnetism. Since the electric polarization does not break time-reversal symmetry, polarization cannot produce magnetic ordering as the spiral spin order with broken inversion symmetry induces spontaneous ferroelectric polarization. Thus the control of magnetism by electric fields, essential in novel technological application, would require other mechanisms [9]. For instance, in conical spiral ferroelectric CoCr_2O_4 clamping of ferrimagnetic and ferroelectric domain walls can be achieved by ME cooling process. The behavior of single ME domain is clearly shown in polarization reversal by applied magnetic fields [10]. Furthermore, the inverse effect, electric control of magnetization reversal, would be expected in such conical spiral spin structure. But the tiny magnitude of polarization ($\sim 4 \mu\text{C}/\text{m}^2$) would make it difficult to reverse magnetization due to production of small electric energy when even a large electric field applied. Another way toward electric control of magnetism is to utilize a phase competing region where the ferroelectric-spiral phase competes with paraelectric-antiferromagnetic (or paraelectric-weak ferromagnetic) phase [11]. In this narrow temperature window of metastable states, the application of electric field may induce a

phase transition between two different phases, leading to the electric control of ME phase (or magnetization).

3. REFERENCES

- [1] T. Kimura *et al.*, Phys. Rev. Lett. **94**, 137201 (2005).
- [2] T. Kimura *et al.*, Nature Mater. **7**, 291 (2008).
- [3] S. Park *et al.*, Phys. Rev. Lett. **98**, 057601 (2007).
- [4] S. Lee *et al.*, Phys. Rev. B **78**, 100101(R) (2008).
- [5] Y. H. Chu *et al.*, Mater. Today **10**, 16 (2007).
- [6] J. F. Scott, J. Phys.: Condens. Matter **20**, 021001 (2008).
- [7] J. Wang *et al.*, Science **299**, 1719 (2003).
- [8] T. J. Choi, S. Lee, Y. J. Choi, V. Kiryukhin and S-W. Cheong, Science **324**, 63 (2009).
- [9] S-W. Cheong and M. Mostovoy, Nature Mater. **6**, 13 (2007).
- [10] Y. J. Choi *et al.*, Phys. Rev. Lett. **102**, 067601 (2009).
- [11] T. Kimura and Y. Tokura, J. Phys.: Condens. Matter **20**, 434204 (2008).

Appendix I.

Spin rotation and domain walls

Yamasaki *et al.* [1] found that on reversing the magnetization, the polarization also reversed. that is, $\text{sign}(\mathbf{M}) \cdot \text{sign}(\mathbf{P})$ is invariant in this process. This begs an explanation: The sign of \mathbf{P} is correlated with the sign of the spiral wave vector \mathbf{Q} , but the dominant energy, the Heisenberg exchange, is invariant under $\mathbf{Q} \rightarrow -\mathbf{Q}$, for either sign of \mathbf{M} ; so why should the sign of \mathbf{P} depend on the sign of \mathbf{M} ? We believe Yamasaki *et al.* were on the right track, looking for an explanation in the magnetization reversal process. However, their analysis was somewhat limited, and contained a somewhat misleading statement, namely that their observation implied invariance of $\mathbf{P} \times \mathbf{M} \equiv \mathbf{T}$, (which they called the average toroidal moment) [2], through a domain wall, whereas it is only the signs of \mathbf{P} and \mathbf{M} that were observed to be correlated. We therefore present an expanded discussion.

As a prelude to discussion of a domain wall, first consider a single conical spiral, cone half angle θ . Consider an ‘up’ domain,

$$\mathbf{M} = \hat{z} \cos \theta. \quad (\text{AII-1})$$

Then the spiralling components lie in the x-y plane:

$$\mathbf{S}_n = \sin \theta (\hat{x} c_n + \hat{y} s_n) + \hat{z} \cos \theta. \quad (\text{AII-2})$$

where

$$\begin{aligned} c_n &= \cos(\mathbf{Q} \cdot \mathbf{R}_n + \phi) \\ s_n &= \sin(\mathbf{Q} \cdot \mathbf{R}_n + \phi) \end{aligned} \quad (\text{AII-3})$$

the arbitrary phase ϕ shows there is no particular significance of the choice of \hat{x} and \hat{y} , as far as the spins are concerned. For simplicity, consider a simple cubic array of spins, with \hat{Q} , the direction of \mathbf{Q} along (100)($\equiv \hat{x}$). Then $\mathbf{Q} \cdot \mathbf{R}_n = naQ$, where a = lattice constant, na is the x-coordinate of a lattice site, and $Q > 0$; so this coordinate increases with n along the positive-x direction. Then,

$$\mathbf{S}_n \times \mathbf{S}_{n+1} = \sin^2 \theta \sin Qa \hat{z} + \sin \theta \cos \theta [\hat{x}(s_n - s_{n+1}) + \hat{y}(c_{n+1} - c_n)], \quad (\text{AII-4})$$

where $\mathbf{R}_{n+1} - \mathbf{R}_n = a \hat{x}$. Using the theories for spiral magnetoelectrics⁴⁻⁶, the electric dipole moment per spin is proportional to

$$\mathbf{P} = N^{-1} \sum_n \hat{x} \times (\mathbf{S}_n \times \mathbf{S}_{n+1}) \quad (\text{AII-5})$$

$$= N^{-1} \sum_n [-\hat{y} \sin^2 \theta \sin Qa + \hat{z} (c_{n+1} - c_n)] \quad (\text{AII-6})$$

$$= -\sin^2 \theta \sin Qa \hat{y}. \quad (\text{AII-7})$$

I.e., \mathbf{P} is in the negative y-direction. The sum on the z component in (S4-6) causes its disappearance. Thus

$$\mathbf{T} \equiv \mathbf{P} \times \mathbf{M} = -\cos \theta \sin^2 \theta \sin Qa \hat{x} \quad (\text{AII-8})$$

(in the negative x-direction, taking $0 \leq \theta \leq \pi/2$).

Now we consider the structure of a domain wall. This is a rather complex problem if looked on in its full generality: there are two disparate length scales, the spiral wavelength, $\approx 10\text{\AA}$, and the much greater wall thickness; there is the question of the direction of \mathbf{Q} relative to the wall boundaries, as well as the directions of \mathbf{M} and \mathbf{P} . We note that the dominant energy, the exchange, determines \hat{Q} relative to the crystal, as well as $|\mathbf{Q}|$, and forces the conical form of the spin orientations. But this energy leaves arbitrary the direction of the cone axis relative to \hat{Q} and the crystal. This reasonably

allows the simplification of assuming the cone structure is rigid through the wall, and \mathbf{Q} is fixed in the crystal.

Thus we assume uniform spin rotations to simulate a domain wall. In our model with simple cubic crystal structure, we then assume \mathbf{Q} is fixed along the x -direction. We assume a simple 180° wall with $\mathbf{Q} \perp$ or \parallel to the wall boundary planes. We consider separately two simple cases, rotation R_x through angle γ about the x -axis, and R_y about the y -axis.

1. Rotations about the x -axis (the “T- or Q-axis”)

One has

$$\begin{aligned} R_x \hat{x} &= \hat{x} \\ R_x \hat{y} &= \hat{y} \cos \gamma + \hat{z} \sin \gamma \\ R_x \hat{z} &= -\hat{y} \sin \gamma + \hat{z} \cos \gamma. \end{aligned} \quad (\text{AII-9})$$

Thus,

$$\mathbf{S}_n' \equiv R_x \mathbf{S}_n = \sin \theta [\hat{x} c_n + (\hat{y} \cos \gamma + \hat{z} \sin \gamma) s_n] + \cos \theta (-\hat{y} \sin \gamma + \hat{z} \cos \gamma). \quad (\text{AII-10})$$

This gives

$$\begin{aligned} \mathbf{S}_n' \times \mathbf{S}_{n+1}' &= \sin^2 \theta \sin Q a (\hat{z} \cos \gamma - \hat{y} \sin \gamma) \\ &\quad + \sin \theta \cos \theta [\hat{x} (s_n - s_{n+1}) + (\hat{y} \cos \gamma + \hat{z} \sin \gamma) (c_n - c_{n+1})] \end{aligned} \quad (\text{AII-11})$$

(just the rotation of (AII-4)).

We are to insert this into (AII-5). The 2nd term, which vanished for the single domain after summing on n , will vanish, similarly, for $\hat{Q} \parallel$ the wall boundary; for the other case, $\hat{Q} \perp$ the wall boundary, this term will fluctuate sinusoidally on the scale $2\pi / Q \sim a \approx 8\text{\AA}$

for CoCr_2O_4 . Since one expects the domain wall thickness to be much greater than that, we can reasonably neglect this term, giving

$$N^{-1} \sum_n \mathbf{S}_n \times \mathbf{S}_{n+1} = \sin^2 \theta \sin Qa (\hat{z} \cos \gamma - \hat{y} \sin \gamma). \quad (\text{AII-12})$$

Note that \mathbf{Q} effectively changes sign when γ goes from 0 to π . Thus the rotated dipole moment, for both \hat{Q} , is

$$\mathbf{P}' = \sin^2 \theta \sin Qa (-\hat{y} \cos \gamma - \hat{z} \sin \gamma). \quad (\text{AII-13})$$

We also have

$$\mathbf{M}' = \cos \theta (-\hat{y} \sin \gamma + \hat{z} \cos \gamma). \quad (\text{AII-14})$$

We finally obtain \mathbf{T} transformed by rotation of the spins about the x -axis

$$\mathbf{T}' = -\hat{x} \cos \theta \sin^2 \theta \sin Qa. \quad (\text{AII-15})$$

This checks the statement of Yamasaki *et al* that \mathbf{T} is invariant through the wall, i.e. \mathbf{T} is independent of γ (the only rotations considered there are R_x).

2. Rotations about the y -axis (the “P-axis”)

For the y -rotations

$$\begin{aligned} R_y \hat{x} &= \hat{x} \cos \gamma - \hat{z} \sin \gamma \\ R_y \hat{y} &= \hat{y} \\ R_y \hat{z} &= \hat{x} \sin \gamma + \hat{z} \cos \gamma. \end{aligned} \quad (\text{AII-16})$$

Following the same procedure as for the x -rotations we find

$$\mathbf{P}' = -\hat{y} \cos \gamma \sin^2 \theta \sin Qa \quad (\text{AII-17})$$

and

$$\mathbf{M}' = \cos \theta (\hat{x} \sin \gamma + \hat{z} \cos \gamma). \quad (\text{AII-18})$$

Thus,

$$\mathbf{T}' = -\cos \theta \sin^2 \theta \sin Qa (\hat{x} \cos \gamma - \hat{z} \sin \gamma). \quad (\text{AII-19})$$

So now the axis along \mathbf{T} changes direction, that is, \mathbf{T} is not invariant, in general, across a Bloch wall. However, again it is seen that the full rotation through π gives $\mathbf{T}' = \mathbf{T}$ consistent with the experimental findings.

Reflecting on the various results above, we would say that the results for R_x , i.e. rotations around the \mathbf{T} -axis, are not at all surprising: All three of the observables (\mathbf{M} , \mathbf{P} and \mathbf{T}) behave exactly as one would expect, being merely the rotations, respectively, of their single-domain values (AII-1), (AII-7), and (AII-8). However, there is a quite surprising result under y - or \mathbf{P} -axis rotations. Certainly, à priori, one would expect rotations about this axis to leave \mathbf{P} unchanged; this is an ordinary, or polar vector, one would think. But the calculation says \mathbf{P} changes as the spin rotation angle γ changes! That is, rotation about the \mathbf{P} direction changes \mathbf{P} . The explanation of this behavior is probably that the rotations are of the spins (holding the lattice positions fixed), *clearly the relevant operation for the physical question considered*. But the usual symmetry operations under which vectors are classified involve the whole structure, including the lattice positions, and this would include rotating \hat{x} in eq. (AII-5).

The significance of this is that the experimental observations concerning the simultaneous change in sign of \mathbf{P} and \mathbf{M} are explained for the wall formed by rotation through π about any axis in the x - y plane. The generalization to any such direction confirms this statement [3].

3. Which rotation axis is best, i.e. expected physically?

To minimize confusion about the geometry, we first discuss the case where \hat{Q} , i.e. \hat{x} , is \perp the wall boundary. For ordinary soft bulk ferro- or ferrimagnets (with no electric polarization), the rotation axis is \hat{Q} , i.e. a Bloch wall. The reason is that this minimizes the magnetostatic energy (due to the long range dipole-dipole interactions). And this interaction can be interpreted in terms of the existence of free magnetic charges, $\propto \nabla \cdot \mathbf{M}$. One can easily see that for a wall of the form of a spiral connecting an up to a down domain, this vanishes only for the rotation axis $= \hat{Q}$. Our case has, in addition to the requirement that the magnetostatic energy be minimized (which first of all requires the existence of domains so that the total magnetic moment vanishes), but also the electrostatic energy to consider. A similar argument as to the existence of free electric charges should occur. So originally this led us to the conclusion that the rotation should be the \mathbf{T} -axis (then both \mathbf{M} and \mathbf{P} will spiral in the plane $\perp \hat{Q}$ and so both divergence of \mathbf{M} and of \mathbf{P} will vanish). However, domain walls in known ferroelectrics, like BaTiO_3 , are very narrow. We presume that is because there the polarization is due to lattice distortion which is very stiff (analogous to highly anisotropic magnets), giving an energy that outweighs the electrostatic energy. Now there are two fundamentally different microscopic mechanisms for spiral-caused ferroelectricity, as we have said. For the one where the primary cause is distortion of the lattice [4], the situation might be similar to BaTiO_3 . But for the case where the primary cause is a charge density distortion [5, 6], the resistance to rotation of \mathbf{P} might be quite soft. Thus there are competing tendencies, and

without a direct measurement of the wall structure, or a detailed calculation of these competing effects, we don't know how magnetization and polarization look in a domain wall of this kind of multiferroic. This discussion seems to suggest that knowledge of the nature of the wall might give insight into which mechanism for the spiral-caused ferroelectricity is more important.

Finally, we mention the other case, $\hat{Q} = \hat{x} \parallel$ to the wall boundary plane. Assuming, again, a Bloch wall, so \mathbf{M} is, again, in the plane of the domain wall, \mathbf{P} is \perp to that plane, with $\mathbf{T} \parallel$ to that plane. So the magnetic Bloch wall occurs for spin rotation about \mathbf{P} , with \mathbf{P} not rotating, but changing its component along \hat{y} (\perp to the wall boundary). The latter would entail large electrostatic energy, but as in the previous case, it is not clear if that would dominate.

4. References

- [1] Y. Yamasaki *et al.*, Phys. Rev. Lett. **96**, 207204 (2006).
- [2] It has been noted that this quantity does not conform to the historical definition of toroidal moment (See C. Ederer, and N. A. Spaldin, ArXiv/cond-mat/0608227 (2006).); nevertheless we consider $\mathbf{P} \times \mathbf{M}$ because of the usage of Yamasaki *et al.* [1].
- [3] Sergienko, *et al.*, I. A. Phys. Rev. B **73**, 094434 (2006).
- [4] M. Mostovoy, Phys. Rev. Lett. **96**, 067601 (2006).
- [5] T. A. Kaplan and S. D. Mahanti, arXiv/cond-mat/0608227 (2006).
- [6] H. Katsura *et al.*, Phys. Rev. Lett. **95**, 057205 (2005); C. Jia *et al.*, Phys. Rev. B **76**, 144424 (2007).

Appendix II.

Magnetic x-ray scattering from complex spin structures

We have calculated the resonant magnetic x-ray coherent scattering intensity for a spiral, and more general spin structures. We found that while scattering of linearly polarized light cannot distinguish between spirals of wave vector \mathbf{Q} and $-\mathbf{Q}$, the circularly polarized case can make such a distinction. Details of this result, which we believe is a minor generalization to more complex spin states of a previous work [1], are provided here.

We consider cases where the Fourier components of the spins are a discrete set

$$\mathbf{S}_n = \sum_j \mathbf{C}_j \exp i\mathbf{Q}_j \cdot \mathbf{R}_n + c.c. \quad (\text{AIII-1})$$

A familiar special case of this is where there is just one non-zero $\mathbf{C} = (\hat{x} - i\hat{y})/2$, which yields a simple spiral

$$\mathbf{S}_n = \hat{x} \cos \mathbf{Q} \cdot \mathbf{R}_n + \hat{y} \sin \mathbf{Q} \cdot \mathbf{R}_n. \quad (\text{AIII -2})$$

The Fourier amplitudes \mathbf{C}_j are not known for our case of CoCr_2O_4 , particularly where we find more than one wave vector (in addition to the one at $\mathbf{Q}=0$, which corresponds to the axial spin components in the ferrimagnetic spiral). We confine ourselves here to just the non-zero wave vectors. For simplicity, and with some measure of intuitive reasonableness, we take these contributions as being of the form

$$\mathbf{C}_j = c_j (\hat{x} - i\hat{y}); \quad (\text{AIII -3})$$

that is equivalent to saying the spin state is a linear combination of spirals all lying in the x-y plane with different wave vectors, strengths and phases. Then the intensity for resonant scattering as a function of the scattering vector \mathbf{k} is found to be proportional to

$$\begin{aligned} I(\mathbf{k}, \dots \mathbf{Q}_j \dots) = & a \sum_m |c_m|^2 [\delta(\mathbf{k} + \mathbf{Q}_m) + \delta(\mathbf{k} - \mathbf{Q}_m)] \\ & + b \sum_m |c_m|^2 [\delta(\mathbf{k} + \mathbf{Q}_m) - \delta(\mathbf{k} - \mathbf{Q}_m)] \end{aligned} \quad (\text{AIII -4})$$

where

$$\begin{aligned} a &= |p_x|^2 + |p_y|^2, \\ b &= 2 \text{Im}(p_x^* p_y), \\ \mathbf{p} &= (\mathbf{e}_s^* \times \mathbf{e}_i)(F_{1,1} - F_{1,-1}), \end{aligned}$$

and \mathbf{e}_i and \mathbf{e}_s are the incident and scattered polarizations. Also, $\delta(\mathbf{k})$ is the familiar function that is peaked at the reciprocal vectors \mathbf{G} , giving rise to Bragg peaks, and $F_{1,\pm 1}$ are scattering amplitudes corresponding to the changes in magnetic quantum number $\Delta m = \pm 1$ [2]. This intensity formula was derived on the basis of the scattering amplitude for resonant elastic scattering by a single spin in the z direction, namely $-i\mathbf{p} \cdot \hat{\mathbf{z}}(F_{1,1} - F_{1,-1})$ [3].

The essential point here is that the coefficient of a is even in $\mathbf{Q}_j \rightarrow -\mathbf{Q}_j$, whereas the coefficient of b is odd. Thus the intensities at \mathbf{Q}_j and $-\mathbf{Q}_j$ will be equal if $b=0$, which occurs for linear polarization, but they differ when $b \neq 0$, achievable by using circular polarization. In our experiments, the field of view for the scattered beam is limited; e.g., for the wave vectors involved, one sees several peaks at the \mathbf{Q}_j , but their negatives are not visible. The question arises, do the \mathbf{Q}_j change sign on magnetization

reversal, as would be predicted by the picture indicated by Yamasaki *et al.* [4], as discussed in (Appendix II. Spin rotation and domain walls). Eq. (AIII -4) says if that picture is correct, then the intensities of the *observable* peaks should change, from $a+b$ to $a-b$. We actually predicted this before the circular polarization experiment was carried out; and indeed such a change was observed, where a uniform change, i.e. reduction of all the peaks (for which the change was significant), occurred.

Finally, comparing the changes for fixed magnetization across the 14 K transition, we observed that the higher intensities held for both temperatures. Furthermore, the \mathbf{Q}_j are approximately equal vectors, so that a and b will be essentially independent of \mathbf{Q}_j . Thus, despite the fact that the locations of the most intense peaks change across the transition, we conclude that the \mathbf{Q}_j do not change sign across that transition.

4. References

- [1] M. Blume and D. Gibbs, Phys. Rev. B **37**, 1779 (1988) .
- [2] J. P. Hannon *et al.*, Phys. Rev. Lett. **61**, 1245 (1988).
- [3] Actually there is another, added, term, quadratic in the spin direction; this would however give rise to peaks outside our experimental field of view.
- [4] Y. Yamasaki *et al.*, Phys. Rev. Lett. **96**, 207204 (2006).

Appendix III.

Handedness vs. Chirality

The terms of chirality and handedness have been customarily considered as equivalent. However, in our scrutiny of handedness in multiferroic CoCr_2O_4 , we have realized that the term “handedness” comprises two different meanings, both of long-established utility. One dates back to the invention of vector analysis, having to do with the handedness associated with the vector- or cross-product. The other dates back to Pasteur and Lord Kelvin, related to, actually identical to, chirality, the lack of mirror symmetry of an object [1]. The FIG. AI.1 shows the pictorial relationship between handedness, defined with vector cross products, and chirality in terms of two disks that partially overlap to each other. There exist three situations: chiral handedness, non-chiral handedness, and chirality without handedness.

1. Situation-I : handed and chiral

The conventional equivalence of handedness and chirality is attributed to most cases in the handedness usage belonging to this situation. The simple example is the two-types-of-handed screws without head or tail. One of them can be certainly called as right-handed, and the other one left-handed depending on the rotation direction of a screw. Taking the mirror reflection for a handed screw, it should not be superposable to its mirror image. So the simple screw can be seen to be chiral and handed. A chiral molecule forming a chiral or spiral as another example is also handed as well as chiral. There is certainly an absence of mirror symmetry of a chiral molecule. Verifying it to be handed,

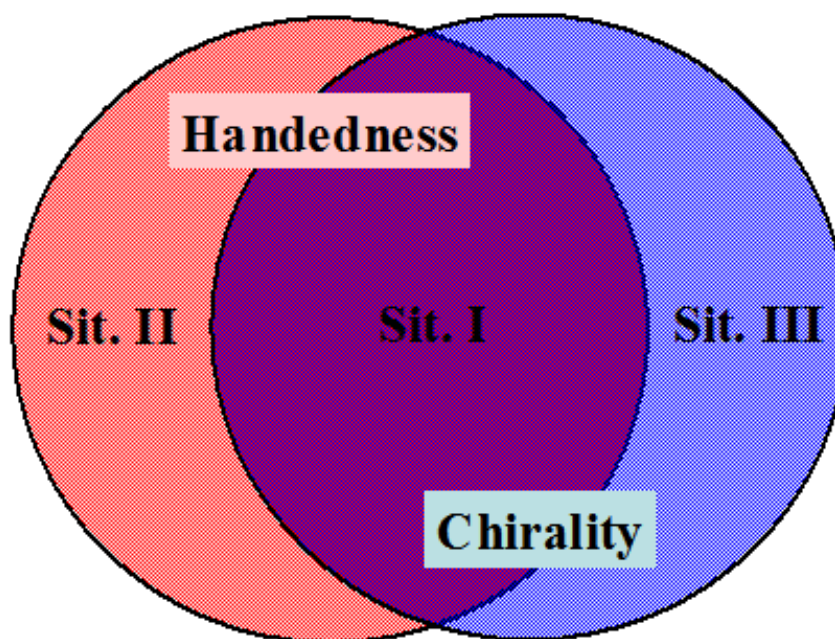


FIG. AI. 1. Pictorial diagram representing the relationship between handedness and chirality. Left (red) and right (blue) circles cover the areas where handedness and chirality are valid, respectively. In the overlapped region (purple), an object is handed as well as chiral.

if one assigns a position vector to each atom, perpendicular to the axis of the molecule, then these vectors rotate uniformly as one moves along the axis. So the vector product of two successive ones will point along either + or – direction, showing a kind of handedness.

2. Situation-II : handed but not chiral

The light propagation among three vector quantities, electric field (E), magnetic field (B) and propagation wave vector (k) can be seen to be achiral - identical to their mirror images, but clearly handed in the sense of the very definition relying on the right-handed rule in the vector-cross-product. For a light plane wave in free space, we can construct $E \times B \cdot k > 0$ which indicates right-handedness found in nature (see FIG. AI.2)[2]. We note that the usual sameness of chirality and handedness must be distinguished when the physical situation involves both polar and axial or pseudovectors.

3. Situation-III : not handed but chiral

The distinct example of this type is an elm tree. This is clearly chiral, not superposable on its mirror image. Showing it not to be handed, consideration of two consecutive position vectors to branches of the tree is comprehensive of randomness in the sign of every vector product, pointing either + or – direction. So the whole sum of the vector products is cancelled out - not handed. A simple realization of this kind is shown in FIG. AI.3.

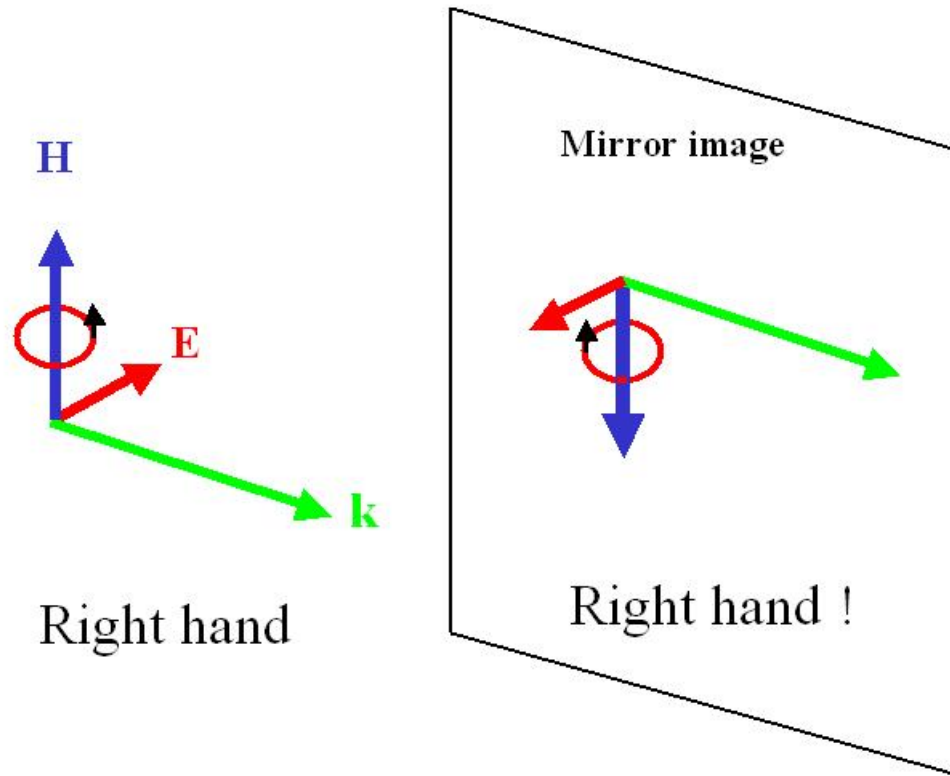


FIG. AI. 2. The handed relationship of three vectors for light propagation, which can be seen as not chiral. This is primarily because of the pseudo-vector nature of magnetic field.

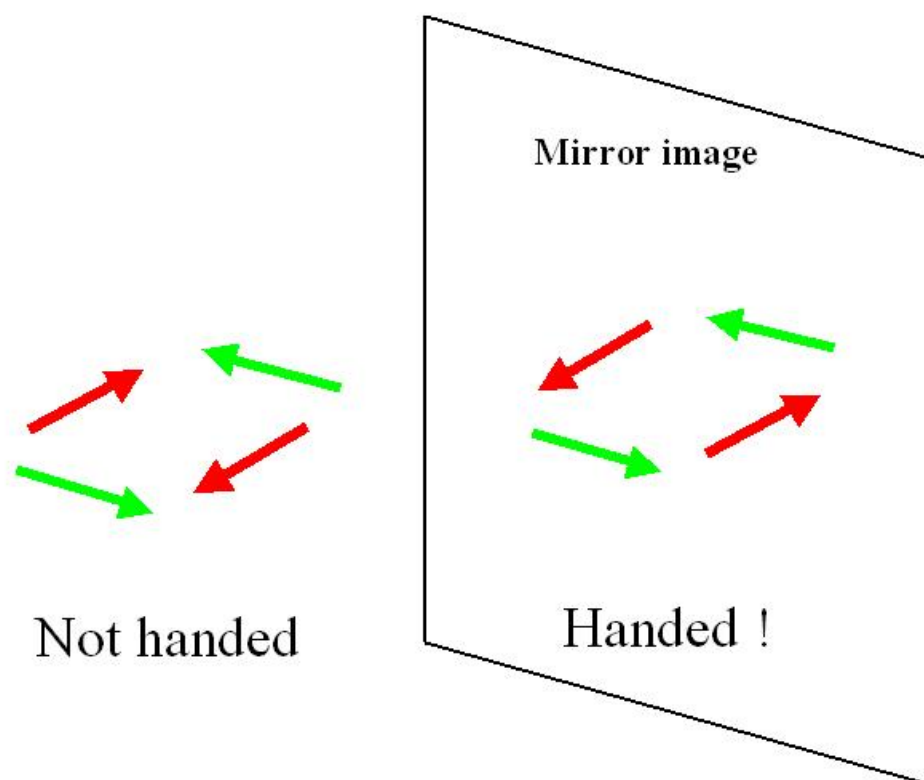


FIG. AI. 3. The mirror image of a not-handed object with polar vectors can be handed, so the object is chiral.

4. REFERENCES

- [1] Harris, A. B., Kamien, R. D. & Lubensky, T. C. Molecular chirality and chiral parameters. *Rev. Mod. Phys.* **71**, 1745-1757 (1999).
- [2] See, for example, Purcell, E. M. *Electricity and Magnetism*, 2nd edition, pg. 209, (McGraw-Hill, NY, 1985).

Appendix IV.

PRL 98, 057601 (2007)

PHYSICAL REVIEW LETTERS

week ending
2 FEBRUARY 2007

Ferroelectricity in an $S = 1/2$ Chain Cuprate

S. Park, Y. J. Choi, C. L. Zhang, and S.-W. Cheong

*Rutgers Center for Emergent Materials & Department of Physics and Astronomy, Rutgers University,
Piscataway, New Jersey 08854, USA*

(Received 19 September 2006; published 31 January 2007)

We report our discovery of ferroelectricity in the spiral-magnetic state in the quantum quasi-one-dimensional (1D) $S = 1/2$ magnet of LiCu_2O_2 . Electric polarization (P) emerges along the c direction below the spiral-magnetic order temperature, but changes from the c to a axis when magnetic fields (H) are applied along the b direction. We also found that P_c increases with H_c , and P_a appears with H_a . LiCu_2O_2 in zero field appears to be the first ferroelectric cuprate and also a prototypical example of the "1D spiral-magnetic ferroelectrics." However, the unexpected behavior in H may demonstrate the complexity of the ordered spin configuration, inherent in the 1D $S = 1/2$ magnet of LiCu_2O_2 .

DOI: 10.1103/PhysRevLett.98.057601

PACS numbers: 77.80.Fm, 75.10.Pq, 75.80.+q, 77.22.Ej

Ferroelectricity is the electronic version of magnetism, associated with the polar arrangement of charges. Ferroelectricity turns out to be mutually exclusive to magnetism because, for example, in the class of transition metal oxides, to which most ferroelectrics belong, the nonzero d electrons, required for the presence of magnetic moments, tend to reduce the energy gain associated with ferroelectric distortion [1,2]. Therefore, only a limited number of compounds, the so-called multiferroics, exhibit the coexistence of magnetism and ferroelectricity. Even in the multiferroics, the interaction between magnetism and ferroelectricity is rather weak. Recent discoveries of spectacular cross-coupling effects in frustrated magnets, such as reversibly flipping ferroelectric polarization or a drastic change of the dielectric constant with applied magnetic fields, offer new opportunities for a thorough scientific understanding of multiferroicity as well as multiferroic applications [3–7].

Multiferroics with enhanced cross-coupling effects exhibit magnetic orders with broken centrosymmetry. It turns out that the lattice relaxation through exchange striction associated with the magnetic orders with noncentrosymmetry is the origin of magnetism-induced ferroelectricity [8–11]. The exchange coupling between spins, where exchange striction is associated, is a tensorial quantity, and has symmetric parts and antisymmetric parts. The symmetric parts seem to be relevant to multiferroicity in systems such as RMn_2O_5 [12], and the antisymmetric parts, which constitute the so-called Dzyaloshinskii-Moriya (DM) interaction, become active when ferroelectricity is induced by spiral-magnetic orders in systems such as TbMnO_3 , $\text{Ni}_3\text{V}_2\text{O}_8$, delafossite CuFeO_2 , hexaferrite $(\text{Ba}, \text{Sr})_2\text{Zn}_2\text{Fe}_{12}\text{O}_{22}$, spinel CoCr_2O_4 , and MnWO_4 [13–19]. Note that TbMnO_3 , CoCr_2O_4 , and MnWO_4 are 3D compounds, and $\text{Ni}_3\text{V}_2\text{O}_8$ and CuFeO_2 are quasi-2D systems.

A prototypical condition for obtaining a spiral-magnetic order is when in a chain magnet the nearest-neighbor (NN) ferromagnetic coupling (J_F) competes with the next-nearest-neighbor (NNN) antiferromagnetic coupling

(J_{AF}). In a classical regime, it is well known that when $|J_{AF}/J_F|$ is larger than $1/4$, a spiral order with $2\pi\xi = \cos^{-1}(1/[4J_{AF}/J_F])$ (pitching angle $= 2\pi\xi$) becomes the ground state [20]. Even though it has been controversial, LiCu_2O_2 appears to be a wonderful example of this 1D spiral magnet with NN $J_F \approx -11 \pm 3$ meV and NNN $J_{AF} \approx +7 \pm 1$ meV [21–24]. In LiCu_2O_2 , 4 planar oxygens among five oxygens coordinating a Cu^{2+} ion form an edge sharing plate extending to the chain b direction, and lead to a $\sim 94^\circ$ NN superexchange route along the b axis as shown in Fig. 1(a). The presence of the magnetic superlattice peak of $(0.5, 0.826, 0)$ was reported, and thus the spiral modulation ξ along the chain direction is 0.174, which corresponds to the pitching angle of 62.6° [21]. These experimental values are in accordance with the estimated ratio of $|J_{AF}/J_F| \approx 0.50$ – 0.65 . From neutron scattering results, it was proposed that the spiral plane is the ab plane [21]. However, our experimental results seem to be inconsistent with the proposition of the ab spiral plane.

Herein, we report our surprising discovery that the quantum $S = 1/2$ chain magnet of LiCu_2O_2 exhibits ferroelectricity when the spiral-magnetic order sets in.

Single crystals of LiCu_2O_2 were grown by the self-flux method using excessive CuO_2 powders as a flux in a Pt crucible. Black platelet crystals with the size of ~ 0.2 cm³ were obtained after slowly cooling from 1250 to 950 °C in air. X-ray powder diffraction results at room temperature indicated a single phase of LiCu_2O_2 with an orthorhombic unit cell [$Pnma$, $a = 5.734(4)$ Å, $b = 2.856(2)$ Å, and $c = 12.415(6)$ Å]. Insulating pieces were collected and cut in a rectangular shape with a cross sectional area of 3–4 mm² and a thickness of 0.2–0.4 mm. The resistances of the specimens are $\sim 10^7$ Ω at room temperature and too large to be measured below ~ 150 K. The dielectric constant (ϵ) was measured by an LCR meter at $f = 28$ kHz with an excitation of 1 V. Pyroelectric and magnetoelectric currents were measured with an electrometer at a rate of 4 K/s and 0.02 T/s, respectively, after cooling specimens in a static poling electric field of $E_{\text{pole}} = 400$ – 1200 kV/m

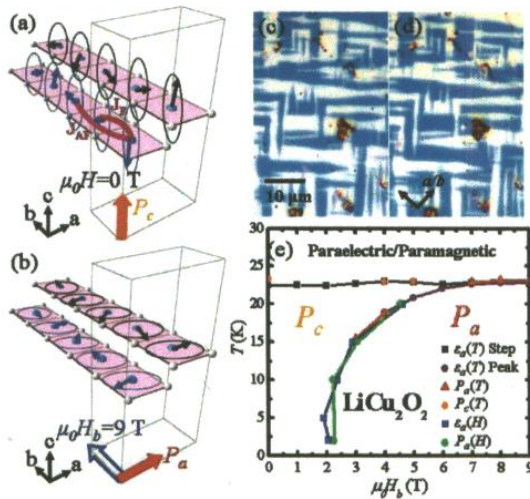


FIG. 1 (color online). (a) Proposed spiral spin structure in zero field, consistent with the presence of a finite electric polarization (P) along the c axis. Cu^{2+} ions (in blue or medium gray) are coordinated by five oxygen atoms (in white) including one apical one. (b) Proposed spiral spin structure in $H = 9$ T along the b axis. In H_b , P switches to the a axis. (c),(d) Polarized optical microscope images of the ab plane of LiCu_2O_2 . The domain boundaries appear with 45° away from the crystallographic a/b axes (in arrows). (e) Phase diagram of LiCu_2O_2 , showing the presence of a paraelectric-paramagnetic state, a FE state with P_c and a FE state with P_a induced by H_b .

(the poling field was removed just before the measurements). A SQUID magnetometer was used for magnetization measurement.

A twin structure was observed in the ab plane of the LiCu_2O_2 crystal under a polarized optical microscope (POM), as shown in Figs. 1(c) and 1(d). Contrast under POM reverses by slightly changing the angle between a polarizer and an analyzer around 90° , confirming that the contrast originates from $\sim 90^\circ$ twins. The twin structure exists because of the similarity in magnitude between the a lattice constant and twice of the b lattice constant [25]. Note that for our macroscopic-size specimens with microscopic twins, we will use the notation of a and b in the way consistent with the concept of spiral-magnetic ferroelectricity. The electric polarization (P) and ϵ along the twinned a/b direction are denoted as P_a and ϵ_a , respectively. When H is applied perpendicular to the electric field for ϵ and P measurements in the ab plane, it is denoted as H_b . When applied parallel, it is denoted as H_a . These notations are used because within the framework of spiral-magnetic ferroelectricity, P is supposedly perpendicular to the spin chain direction, i.e., the b direction. Figure 2(a) shows the temperature (T) dependence of the magnetic susceptibility (χ) and its temperature derivative along the a/b axis. A broad hump of $\chi(T)$ at ~ 40 K is

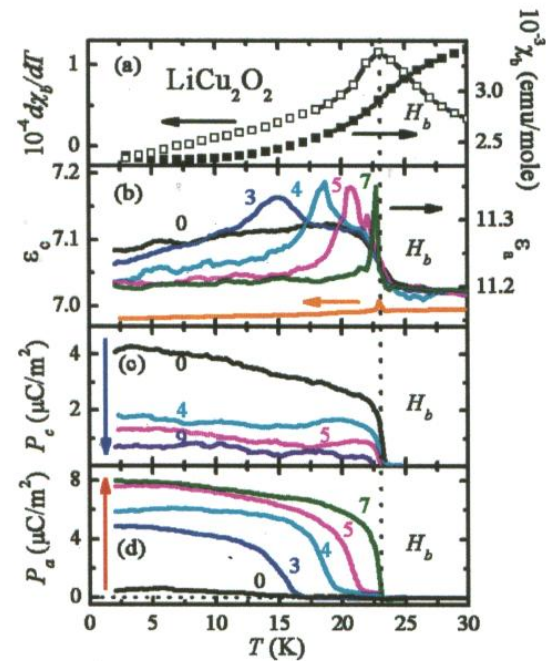


FIG. 2 (color online). (a) Magnetic susceptibility (χ) and $d\chi/dT$ in $H_b = 2$ kOe vs temperature. (b) Dielectric constants (ϵ) along the a and c axes. H_b dependence of ϵ_a is also shown. (c) Temperature dependence of P_c in H_b . All experiments for the H_b dependence were performed in field cooling. (d) Temperature dependence of P_a in H_b .

attributed to the formation of short-range magnetic correlations in the 1D $S = 1/2$ system, and the weak but sharp features in $\chi(T)$ and $d\chi(T)/dT$ at $T_N = 23$ K signify the onset of an antiferromagnetic (AFM) long-range ordering [26]. The T dependence of ϵ along both the a and c directions is displayed in Fig. 2(b). ϵ along the c axis, ϵ_c , reveals a tiny but sharp peak at 23 K, which coincides well with T_N , indicated in $\chi(T)$. Along the a axis, a relatively large steplike increase of ϵ , however, appears below T_N . With applied magnetic fields along the b axis (H_b), $\epsilon_a(T)$ in $H_b = 3$ T shows a broad peak at ~ 15 K, which approaches to T_N in higher H_b , while the steplike anomaly at T_N persists for H_b up to 5 T.

These ϵ features below T_N stem from the emergence of electric polarization in the magnetically ordered state in LiCu_2O_2 . Figures 2(c) and 2(d) exhibit the T dependence of polarization along the c (P_c) and the a (P_a) axes in H_b , measured upon warming after removing E_{pole} at 2 K. First of all, P_c becomes nonzero below T_N , consistent with the presence of a sharp ϵ_c peak at T_N . This polarization is found to reverse when a negative E_{pole} was applied. These behaviors clearly indicate that a ferroelectric state emerges when a magnetic order sets in. With applied H_b , P_c decreases, and becomes negligible in $H_b = 9$ T. On the other

hand, P_a seems to be absent in $H = 0$ T, but appears in $H_b = 3$ T below ~ 15 K. The transition T for P_a moves slowly up to ~ 23 K with increasing $H_b > 3$ T.

This change of the transition T of P_a in H_b is consistent with the behavior of the broad ϵ_a peak in H_b , shown in Fig. 2(b). However, this P_a behavior in H_b is seemingly different from that of P_c , showing a single transition T in various H_b . This is unusual if the appearance of P_a results from the suppression of P_c with increasing H_b . To unveil the origin of this different behavior, we measured the pyroelectric current for P_c in H_b in different ways. For example, the specimen was cooled in a constant E_{pole} to 20 K in 3 T, and the E_{pole} was removed afterwards. Pyroelectric current for P_c was, then, measured while cooling the specimen in 3 T from 20 K to 2 K, and this pyroelectric current shows a distinct feature at 15 K, which appears in a way consistent with the suppression of P_c below 15 K. This observation indicates that the absence of the low- T transition (such as the 15 K transition in 3 T) in $P_c(T)$ in H_b in Fig. 2(c) is due to the loss of poling information below the low- T transition, i.e., the appearance of ferroelectric domains when E_{pole} was removed at 2 K.

The H_b dependence of P_c , P_a , ϵ_a , and M/H at 10 and 20 K, shown in Fig. 3, clearly demonstrates that H_b induces the flipping of P from the c to a direction. While P_c in Fig. 3(a) shows the decrease of its magnitude with increas-

ing H_b , P_a in Fig. 3(b) exhibits an opposite behavior. The corresponding threshold fields are the same for both $P_c(H_b)$ and $P_a(H_b)$, and this transition is also evident in $\epsilon_a(H_b)$ at 10 K shown in Fig. 3(c). This field induced transition occurs at a higher H_b at 20 K, as apparent in $P_a(H_b)$ in Fig. 3(b) and in $\epsilon_a(H_b)$ in Fig. 3(c). Figure 3(b) also demonstrates that repeatedly reversing H_b induces the suppression of P_a upon the magnetic field cycling. This suppression possibly originates from the induction of ferroelectric multidomains when polarization flipping occurs. Figure 3(d) indicates that the small kinks in $H_b \approx 2.4$ T (at 10 K) and ≈ 4.5 T (at 20 K) in $M/H(H_b)$ match with the transitions indicated in $P_c(H_b)$, $P_a(H_b)$, and $\epsilon_a(H_b)$. Both the reversible behavior of the polarization in opposite E_{pole} and the presence of the magnetization anomalies at the consistent threshold H fields support that the polarization results from a bulk effect. For the T and H_b dependence of ϵ_a and P_a , we have constructed a magneto-electric phase diagram of LiCu_2O_2 for H_b , as displayed in Fig. 1(e). The low- H_b state below $T_N \approx 23$ K is a ferroelectric magnetic state with a finite P_c , and high H_b induces the flip of the electric polarization direction from the c to a axis.

In spiral magnets, the DM interaction induces the magnetically driven polarization proportional to $\mathbf{e}_{ij} \times (\mathbf{S}_i \times \mathbf{S}_j)$, where \mathbf{e}_{ij} is the vector connecting the two \mathbf{S}_i and \mathbf{S}_j spins [8]. Our observation of a finite P_c in zero H , combined with the concept of spiral-magnetic ferroelectricity and earlier report of $\mathbf{Q} = (0.5, 1 - \xi, 0)$ with the spin chain along the b axis, indicates that the spiral spins, relevant to the finite P_c , lie on the bc plane; i.e., $\mathbf{S}_i \times \mathbf{S}_j$ is along the a axis. When a magnetic field applied along the b axis, P_c decreases and P_a increases, implying that the Cu^{2+} spin spiral plane flips from the bc to ab plane, resulting the flip of the polarization from the c to a axis as depicted in Figs. 1(a) and 1(b). Note that this picture may be simplified, and represents a projection of the actual configuration of complex spiral spins that is relevant to the presence of the electric polarization [27].

Figure 4(a) shows the T dependence of ϵ along the a axis (ϵ_a) in magnetic fields along the same a axis (H_a): note that the polarization and dielectric constant along the twinned a/b direction are denoted as P_a and ϵ_a as discussed earlier. Unexpectedly, ϵ_a decreases with increasing H_a and a small peak appears at $H_a = 9$ T at 22.2 K, which is slightly lower than $T_N \approx 23$ K. Accordingly, P_a appears and then increases with increasing H_a as shown in Fig. 4(b). Furthermore, as depicted in Fig. 4(b), P_c also increases as H_c increases. The H_a dependent of ϵ_a and P_a is displayed Fig. 4(e), showing the smooth increase of P_a with increasing H_a at 10 K and 20 K without phase transitionlike features.

In general, spins without a net moment (such as antiferromagnetic or spiral spins) tend to orient perpendicular to an applied magnetic field [10]. Thus, it is expected that H_c may flip the spiral plane from the bc to ab plane, so that P may flip from the c to a axis with H_c . However, this is

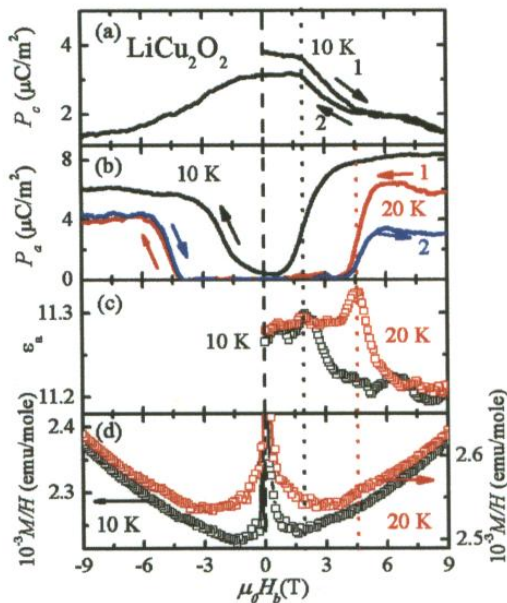


FIG. 3 (color online). H_b dependence of (a) P_c at 10 K and (b) P_a at 10 K and 20 K. H_b reverse-cycling at 20 K shows the reduction of P_a . H_b dependence of (c) ϵ_a and (d) M/H at 10 K and 20 K. The H_b -induced transitions of ϵ at both temperatures are consistent with those of polarizations.

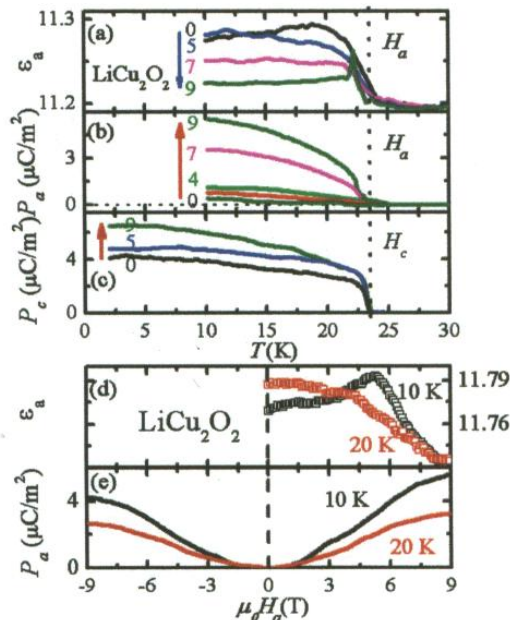


FIG. 4 (color online). (a) Temperature dependence of ϵ_a with H_a . (b) P_a with H_a . (c) P_c with H_c . (d) H_a dependence of ϵ_a at 10 K and 20 K. (e) H_a dependence of P_a at 10 K and 20 K, exhibiting a smooth change of polarization with increasing H_a .

completely in contrast with our observation: H_c enhances P_c and H_b is the one inducing the P flip from the c to a axis. The appearance of P_a with H_a is also counterintuitive within the framework of spiral-magnetic ferroelectricity. These unexpected magnetic field effects may stem from the complexity of the spiral-magnetic order in the 1D $S = 1/2$ magnet. Note that a strong competition between quantum spin fluctuations and the incommensurate helimagnetic state was reported [21]. We also point out that from NMR experiment, Gippius *et al.* suggested that spins rotate on the plane containing the chain while also precessing around the chain [27]. This complex spin configuration may be associated with the quantum and fluctuating nature of LiCu_2O_2 , and the details of this intriguing magnetism remain to be explored. Nevertheless, the behavior of the electric polarization in $H = 0$ can be understood in a simple model based on the framework of spiral-magnetic ferroelectricity as discussed above. We emphasize that as observed in other spiral-magnetic ferroelectrics, the electric polarization is weak, and the appearance of this weak polarization is closely connected to the long-range magnetic ordering. It is evident that the magnitude of ξ is directly related with the ratio of $|J_{AF}/J_F|$, and an applied magnetic field is expected to be of assistance to J_F , so that the magnitude of ξ can be readily modified with magnetic fields [28,29]. The magnetically driven polarization is proportional to $\mathbf{e}_{ij} \times (\mathbf{S}_i \times \mathbf{S}_j)$, where $\mathbf{S}_i \times \mathbf{S}_j$ gives the

connection to the pitching angle [8]. Therefore, the change of the spiral modulation wave length, inversely proportional to the pitching angle, should affect the magnitude of the electric polarization.

In summary, we have discovered the emergence of a ferroelectric polarization in the spiral-magnetic state in the 1D $S = 1/2$ cuprate of LiCu_2O_2 where spiral-magnetic order originates from the competition between NN ferromagnetic and NNN antiferromagnetic couplings. Thus, LiCu_2O_2 is the first example of a ferroelectric cuprate (as far as we are aware of), and appears to be a prototypical example of 1D spiral-magnetic ferroelectrics. Applying magnetic fields can significantly influence the ferroelectric polarization as well as dielectric constants. Understanding the origin of these remarkable magnetic field effects requires further studies on this fascinating ferroelectric cuprate.

We thank L. Mihály and M. Mostovoy for useful discussions. This work was supported by NSF-DMR-0520471.

- [1] N. A. Hill, J. Phys. Chem. B **104**, 6694 (2000).
- [2] D. I. Khomskii, J. Magn. Magn. Mater. **306**, 1 (2006).
- [3] T. Kimura *et al.*, Nature (London) **426**, 55 (2003).
- [4] T. Goto *et al.*, Phys. Rev. Lett. **92**, 257201 (2004).
- [5] N. Hur *et al.*, Nature (London) **429**, 392 (2004).
- [6] N. Hur *et al.*, Phys. Rev. Lett. **93**, 107207 (2004).
- [7] B. Lorenz *et al.*, Phys. Rev. Lett. **92**, 087204 (2004).
- [8] H. Katsura, N. Nagaosa, and A. V. Balatsky, Phys. Rev. Lett. **95**, 057205 (2005).
- [9] I. A. Sergienko, and E. Dagotto, Phys. Rev. B **73**, 094434 (2006).
- [10] Maxim Mostovoy, Phys. Rev. Lett. **96**, 067601 (2006).
- [11] A. B. Harris *et al.*, Phys. Rev. B **73**, 184433 (2006).
- [12] L. C. Chapon *et al.*, Phys. Rev. Lett. **96**, 097601 (2006).
- [13] T. Arima *et al.*, Phys. Rev. Lett. **96**, 097202 (2006).
- [14] M. Kenzelmann *et al.*, Phys. Rev. Lett. **95**, 087206 (2005).
- [15] G. Lawes *et al.*, Phys. Rev. Lett. **95**, 087205 (2005).
- [16] T. Kimura, J. C. Lashley, and A. P. Ramirez, Phys. Rev. B **73**, 220401(R) (2006).
- [17] T. Kimura, G. Lawes, and A. P. Ramirez, Phys. Rev. Lett. **94**, 137201 (2005).
- [18] Y. Yamasaki *et al.*, Phys. Rev. Lett. **96**, 207204 (2006).
- [19] K. Taniguchi *et al.*, Phys. Rev. Lett. **97**, 097203 (2006).
- [20] R. Bursill *et al.*, J. Phys. Condens. Matter **7**, 8605 (1995).
- [21] T. Masuda *et al.*, Phys. Rev. Lett. **92**, 177201 (2004); T. Masuda *et al.*, Phys. Rev. B **72**, 014405 (2005).
- [22] A. A. Gippius *et al.*, Phys. Rev. B **70**, 020406(R) (2004); S.-L. Drechsler *et al.*, Phys. Rev. Lett. **94**, 039705 (2005).
- [23] M. Papagno *et al.*, Phys. Rev. B **73**, 115120 (2006).
- [24] L. Mihály *et al.*, Phys. Rev. Lett. **97**, 067206 (2006).
- [25] R. Berger, P. Önnérud, and R. Tellgren, J. Alloys Compd. **184**, 315 (1992).
- [26] Our susceptibility data up to room temperature are basically identical with the published result in Ref. [21].
- [27] A. A. Gippius *et al.*, J. Magn. Magn. Mater. **300**, e335 (2006).
- [28] V. Kiryukhin, B. Keimer, and D. E. Moncton, Phys. Rev. Lett. **74**, 1669 (1995).
- [29] A. Zheludev *et al.*, Phys. Rev. Lett. **78**, 4857 (1997).

Appendix V.

PRL 100, 047601 (2008)

PHYSICAL REVIEW LETTERS

week ending
1 FEBRUARY 2008

Ferroelectricity in an Ising Chain Magnet

Y. J. Choi,¹ H. T. Yi,¹ S. Lee,¹ Q. Huang,² V. Kiryukhin,¹ and S.-W. Cheong¹¹*Rutgers Center for Emergent Materials and Department of Physics & Astronomy,
136 Frelinghuysen Road, Piscataway, New Jersey, 08854, USA*²*NIST Center for Neutron Research, NIST, Gaithersburg, Maryland 20899, USA*
(Received 13 September 2007; published 29 January 2008)

We report discovery of collinear-magnetism-driven ferroelectricity in the Ising chain magnet $\text{Ca}_3\text{Co}_{2-x}\text{Mn}_x\text{O}_6$ ($x \approx 0.96$). Neutron diffraction shows that Co^{2+} and Mn^{4+} ions alternating along the chains exhibit an up-up-down-down ($\uparrow\uparrow\downarrow\downarrow$) magnetic order. The ferroelectricity results from the inversion symmetry breaking in the $\uparrow\uparrow\downarrow\downarrow$ spin chain with an alternating charge order. Unlike in spiral magnetoelectrics where antisymmetric exchange coupling is active, the symmetry breaking in $\text{Ca}_3(\text{Co}, \text{Mn})_2\text{O}_6$ occurs through exchange striction associated with symmetric superexchange.

DOI: 10.1103/PhysRevLett.100.047601

PACS numbers: 77.80.-e, 75.10.Pq, 75.80.+q, 77.22.Ej

The concept of magnetism-driven ferroelectricity has recently drawn a significant attention [1,2]. In magnetism-driven ferroelectrics, development of inversion-symmetry-breaking magnetic order leads to the loss of the lattice inversion symmetry through exchange striction, thereby leading to the development of ferroelectricity. In these materials, external magnetic field influences the configuration of the magnetic order, naturally leading to changes in ferroelectric or dielectric properties. Spectacular cross-coupling effects, such as reversible flipping of ferroelectric polarization or drastic change of dielectric constant in applied magnetic fields, have been recently observed in magnetism-driven ferroelectrics [3–5]. Spiral magnetic order, resulting from magnetic frustration, is a common way to induce the loss of inversion symmetry, and ferroelectricity has been recently observed in a number of spiral magnets such as TbMnO_3 , $\text{Ni}_3\text{V}_2\text{O}_8$, CuFeO_2 , $(\text{Ba}, \text{Sr})_2\text{Zn}_2\text{Fe}_{12}\text{O}_{22}$, CoCr_2O_4 , MnWO_4 , and LiCu_2O_2 [6–12]. In the spiral magnets, the relevant exchange striction is associated with the antisymmetric part of the exchange coupling, which constitutes the so-called Dzyaloshinski-Moriya (DM) interaction [13–16].

Spiral magnetic order is not the only possible route towards magnetism-induced ferroelectricity. In RMn_2O_5 ($R = \text{Tb-Lu}$), for example, a nearly-collinear acentric magnetic order with broken inversion symmetry was proposed to be responsible for the ferroelectricity [17]. In this mechanism, the ferroelectricity results from lattice relaxation through exchange striction associated with the symmetric superexchange coupling. However, a model where ferroelectricity is induced by a spiral spin configuration along the Mn^{4+} spin chain has been also discussed for RMn_2O_5 [18,19]. Thus, the true origin of multiferroicity in RMn_2O_5 is currently uncertain. Another promising example is the so-called *E*-type magnetic order. This collinear order, combined with alternating oxygen cage rotations, has been suggested as the origin of ferroelectricity in the orthorhombic HoMnO_3 [20]. Polycrystalline HoMnO_3 has been experimentally studied to test this theo-

retical prediction [21], but the induced polarization turned out to be too small to support the proposed theory. Identification of nonspiral magnetism-driven ferroelectrics remains, therefore, an important task. Among those, systems driven by the potentially large symmetric superexchange are, clearly, of special interest.

A simple and conceptually important model in which a collinear spin order induces ferroelectricity through symmetric superexchange can be constructed using an Ising spin chain with competing nearest-neighbor ferromagnetic (J_F) and next-nearest-neighbor antiferromagnetic (J_{AF}) interactions [2]. For $|J_{AF}/J_F| > 1/2$, the ground state mag-

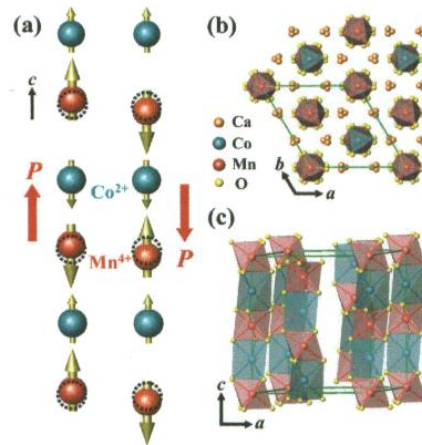


FIG. 1 (color online). (a) Ising chains with the up-up-down-down spin order and alternating ionic order, in which electric polarization is induced through symmetric exchange striction. The two possible magnetic configurations leading to the opposite polarizations are shown. The atomic positions in the undistorted chains are shown with dashed circles. (b,c) The crystal structure of the $\text{Ca}_3\text{CoMnO}_6$ chain magnet. The green boxes represent the crystallographic unit cell.

netic order is of the up-up-down-down ($\uparrow\uparrow\downarrow\downarrow$) type [22]. If the charges of magnetic ions alternate along the chain, this magnetic ordering breaks inversion symmetry on magnetic sites and can induce electric polarization via exchange striction. This mechanism is illustrated in Fig. 1(a). The exchange striction associated with symmetric superexchange shortens the bonds between the parallel spins, while stretching those connecting the antiparallel spins. As a result, electric polarization, P , is induced in the direction of the chain. As shown in Fig. 1(a), there are two ways to combine the $\uparrow\uparrow\downarrow\downarrow$ order with the ionic charge order, giving rise to the opposite electrical polarization vectors. Experimental realization of such a simple model system would be of a significant importance in the field. Herein, we report discovery of a chain magnet in which this model is remarkably realized.

To find the appropriate experimental system, we have identified $\text{Ca}_3\text{Co}_2\text{O}_6$ -derived compounds as possible candidates because $\text{Ca}_3\text{Co}_2\text{O}_6$ is an Ising chain magnet where about a half of Co ions can be replaced by Mn ions [23,24]. The structure of $\text{Ca}_3\text{Co}_{2-x}\text{Mn}_x\text{O}_6$, as depicted in Figs. 1(b) and 1(c), contains spin chains consisting of magnetic ions with alternating oxygen cages of face-shared trigonal prisms and octahedra along the c axis. The spin chains are separated by Ca ions and form a triangular lattice in the ab plane. Mn ions have a strong tendency to avoid the trigonal prismatic oxygen coordination. Thus, for example, for $x = 1$, all the Co ions are located in the trigonal prismatic sites, and all the Mn ions occupy the octahedral sites [24]. We prepared single-phase polycrystalline $\text{Ca}_3\text{Co}_{2-x}\text{Mn}_x\text{O}_6$ with x up to 1 by using standard solid state reaction method [23]. Since single crystals are necessary for conclusive measurements of the ferroelectric properties, we have attempted to grow single crystals of $\text{Ca}_3(\text{Co}, \text{Mn})_2\text{O}_6$ by utilizing the known technique (KCl-K₂CO₃ flux method) for the growth of $\text{Ca}_3\text{Co}_2\text{O}_6$ crystals [25]. With increasing Mn concentration, the crystal growth was found to be increasingly more difficult. However, single crystals with maximum x approaching 0.96 (as determined by comparing x-ray diffraction patterns of crushed crystals with those of polycrystalline samples) were grown successfully.

DC magnetic susceptibility ($\chi = M/H$) was measured in a SQUID magnetometer, specific heat (C) and AC magnetic susceptibility (χ' and χ'') measurements were carried out in the Quantum Design PPMS, and dielectric constant (ϵ) was measured using an LCR meter at $f = 44$ kHz. The temperature (T) dependence of electric polarization (P) was obtained by the integration of pyroelectric current with the T variation of 2 K/min after poling a specimen from 40 to 2 K in a static electric field of $E \approx 6.7$ kV/cm. For ϵ and P measurements, a c -axis needle-shaped crystal was cut and polished with the ab plane cross section of ~ 0.64 mm² and thickness of ~ 0.15 mm, and then annealed at 650 °C for 5 hours to remove strain built

up during polishing. Neutron powder diffraction measurements were performed on polycrystalline $\text{Ca}_3\text{Co}_{2-x}\text{Mn}_x\text{O}_6$ ($x = 0.95$) at the BT-1 beam line at NIST Center for Neutron Research. Monochromatic neutrons ($\lambda = 2.079$ Å) were produced by a Ge(311) monochromator, and the data were collected for $T = 1.4, 8$, and 20 K.

Search for the ferroelectricity was performed in the crystal with the highest Mn concentration, $x = 0.96$, and ferroelectric polarization along the chain direction was indeed found. Figure 2(a) shows that the polarization smoothly emerges below the transition temperature of 16.5 K, increases rapidly below ~ 10 K, and reaches ~ 90 $\mu\text{C}/\text{m}^2$ at 2 K. The appearance of the polarization at 16.5 K coincides with the onset of the magnetic order, which is signified [24] by a broad peak in the magnetic susceptibility, $\chi(T)$, shown in Fig. 2(b). Specific heat also exhibits an upturn at this temperature. The temperature dependence of the dielectric constant along the c axis, $\epsilon_c(T)$, starts deviating from its high-temperature behavior at the onset temperature of the polarization without showing any sharp anomaly, see Fig. 2(c). Instead, $\epsilon_c(T)$ reveals a broad peak at ~ 8 K followed by a sharp decrease at lower temperatures. The electric polarization decreases in a magnetic field applied along the c axis. There is an additional magnetic anomaly at $T \approx 3$ K, which can be seen in the behavior of the derivative $d\chi(T)/dT$ shown in Fig. 2(b); it is discussed in more detail below. The Ising

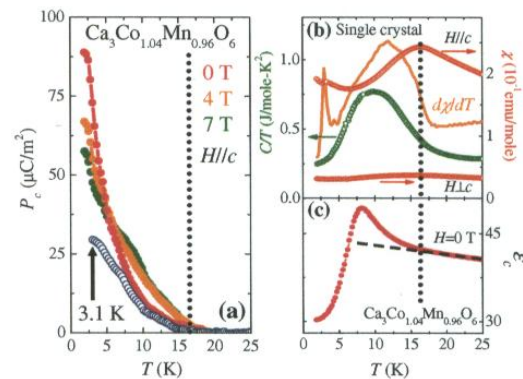


FIG. 2 (color online). (a) Electric polarization of single crystal $\text{Ca}_3\text{Co}_{1-x}\text{Mn}_x\text{O}_6$ ($x = 0.96$) along the chain direction ($P \parallel c$), taken upon warming. The samples were poled upon cooling from 40 K to 2 K (filled circles), and to 3.1 K (open circles) before the measurement. The data for the 2 K poled sample were collected in various applied magnetic fields, as shown. (b) Temperature dependence of magnetic susceptibility, $\chi(T) = M/H$, measured in an applied magnetic field $H = 0.2$ T along and perpendicular to the chain direction. The temperature derivative $d\chi/dT$, and zero-field heat capacity (C/T) are also shown. (c) The c -axis dielectric constant, ϵ_c . Dashed line shows the high-temperature behavior of ϵ_c .

character of this compound is clearly reflected in the large anisotropy of $\chi(T)$.

Studies of $\text{Ca}_3\text{Co}_{2-x}\text{Mn}_x\text{O}_6$ polycrystalline samples suggest that a similar behavior is expected in a wide range of x near $x = 1$. Figures 3(a) and 3(b) display $\chi(T)$ and $\epsilon(T)/\epsilon(T = 20 \text{ K})$ for various Mn concentrations, $x = 0.85, 0.9, 0.95$, and 1.0 . These data exhibit the same features as those of the corresponding quantities of the $x = 0.96$ single crystal, strongly suggesting that the observed properties of the single crystal are representative for large Mn concentrations. The temperatures of the maxima in $\chi(T)$ and $\epsilon(T)$, shown in the insets in Figs. 3(a) and 3(b), decrease with increasing x , indicating the corresponding decrease in the magnetic transition temperature. The corresponding temperatures in the single crystal (dotted lines in the insets) agree well with the Mn concentration $x = 0.96$, corroborating our x-ray results.

The structure of $\text{Ca}_3\text{Co}_{2-x}\text{Mn}_x\text{O}_6$ ($x = 0.95$) was determined using neutron powder diffraction. The possible magnetic structures (including those with ab -plane components) were constructed using the magnetic symmetry analysis, and the diffraction data were refined using the FULLPROF program package [26]. The spins point along the c axis, as indicated by the absence of (003) magnetic peak, and the structure is of the $\uparrow\downarrow\downarrow$ type. The accuracy of the

final refinement result was independently estimated by the Simulated Annealing process, which shows that the deviation of the spins from the c axis cannot exceed 3° . The refinement results for $T = 1.4 \text{ K}$ are shown in Fig. 4: good agreement factors, $\chi^2 = 1.44$, $R_B = 2.4\%$, $R_f = 2.7\%$, and $R_{\text{mag}} = 9.8\%$, are obtained. The obtained three-dimensional magnetic structure is shown in the inset in Fig. 4. In agreement with [24], the Mn ions occupy the octahedral sites. The ordered magnetic moments of Co and Mn ions are $0.66(3)\mu_B$ and $1.93(3)\mu_B$, respectively, and the estimated valences of the cations from Bond-Valence calculation are $1.814(2)$ for Co and $3.997(3)$ for Mn. Thus, the magnetic chains consist of alternating low-spin Co^{2+} and high-spin Mn^{4+} ions. Combined with the $\uparrow\downarrow\downarrow$ spin order, this makes $\text{Ca}_3(\text{Co,Mn})_2\text{O}_6$ an experimental realization of the magnetoelectric model system described above. In the unit cell shown in Fig. 4, all the chains possess the same polarization direction according to this model. We note that the (101) magnetic peak appears to be slightly broadened (see the inset in Fig. 4). This indicates that the magnetic order is not truly long-ranged. Measurements on yet unavailable large single crystals are needed to determine the magnetic correlation length with any adequate precision. On warming to $T = 8 \text{ K}$, no qualitative changes are observed in the magnetic structure, and no magnetic order is present at $T = 20 \text{ K}$.

While the magnetic origin of the ferroelectricity and its description in the framework of the $\uparrow\downarrow\downarrow$ chain with alternating ions are established by the above data, the tempera-

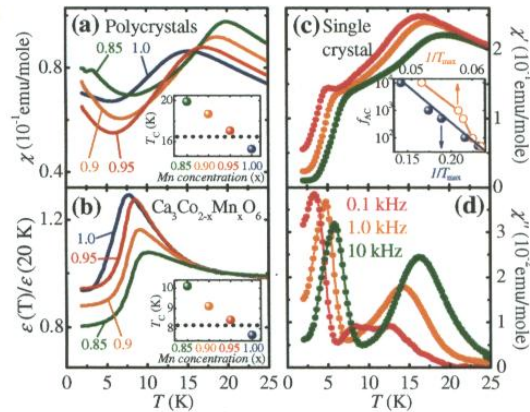


FIG. 3 (color online). (a) $\chi(T)$ of polycrystalline $\text{Ca}_3\text{Co}_{1-x}\text{Mn}_x\text{O}_6$ for $H = 0.2 \text{ T}$. (b) $\epsilon(T)$ of polycrystalline $\text{Ca}_3\text{Co}_{1-x}\text{Mn}_x\text{O}_6$ for $H = 0$, normalized at $T = 20 \text{ K}$. The insets in (a) and (b) show peak positions of $\chi(T)$ and $\epsilon(T)$, respectively, for different Mn concentrations. The dashed lines indicate the corresponding peak positions in the $x = 0.96$ single crystal. (c,d) Real and imaginary parts of the AC susceptibility, $\chi'(T)$, and $\chi''(T)$, of the $x = 0.96$ single crystal. The AC magnetic field is 5 Oe , and the frequencies are $0.1, 1$ and 10 kHz , as shown. The inset in Fig. 3(c) shows $\log[f]$ vs inverse temperature for the peaklike features of χ' . The low-temperature feature is shown with filled circles, and the high-temperature feature with open circles.

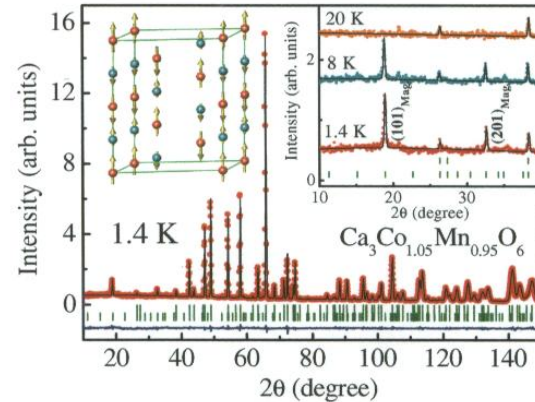


FIG. 4 (color online). Observed (symbols) and calculated (line) powder neutron diffraction patterns for polycrystalline $\text{Ca}_3\text{Co}_{1-x}\text{Mn}_x\text{O}_6$ ($x = 0.95$) for $T = 1.4 \text{ K}$. The first row of bars below the diffraction pattern indicates the positions of the nuclear Bragg peaks, and the second row depicts the locations of the magnetic Bragg peaks. The blue line shows the difference between the observed and calculated diffraction patterns. The insets show the low-angle patterns for $T = 1.4 \text{ K}$, 8 K , and 20 K , and the refined spin structure.

ture dependences of both the electric and the magnetic properties are rather complicated. To gain insight into this complexity, we have measured temperature-dependent AC magnetic susceptibility in the $x = 0.96$ single crystal. Figures 3(c) and 3(d) reveal that both of the magnetic temperature anomalies (peaks) exhibit strong frequency dependence, shifting to higher temperature with increasing frequency. This behavior is indicative of magnetic freezing, which may range from simple superparamagnetism to complex spin-glass transition [27]. As shown in the inset in Fig. 3(c), the lower-temperature peak T_{\max} of $\chi'(T)$ exhibits the Arrhenius behavior, $f = f_0 \exp[-E_a/k_B T_{\max}]$, with physically reasonable values of the activation energy, $E_a/k_B \approx 60$ K, and $f_0 \approx 60$ MHz [27]. This behavior with $E_a/T_{\max} \approx 20$, together with the numerical value of the slope parameter $\Delta T_{\max}/T_{\max} \ln[f]$ of 0.21, signals superparamagnetic blocking (freezing of poorly-correlated magnetic clusters) at low temperatures [27]. The behavior of the higher-temperature anomaly, associated with the magnetic ordering transition, is more complicated. For example, $T_{\max}(>16 \text{ K})$ of $\chi'(T)$ does not exhibit the simple Arrhenius behavior [see the inset of Fig. 3(c)]. The data of Fig. 3, combined with the neutron data, show that only finite-size magnetic domains develop at the magnetic transition and that these domains exhibit an additional freezing at a lower temperature. This behavior deserves further investigation since it is likely related to the one dimensionality of the magnetic chains and the geometrical frustration in the ab -plane triangular lattice.

While complicated, the observed magnetic behavior provides a consistent explanation of the unconventional temperature dependence of the electric polarization in Fig. 2(a). Magnetic disorder and freezing naturally lead to the corresponding phenomena for the ferroelectric properties in our system. Local clusters exhibiting the two different variants of the spin order shown in Fig. 1(a) give rise to the opposite electrical polarization vectors. Thus, on warming from 2 K, the frozen poled magnetoelectric domains should quickly become dynamic, leading to decreased macroscopic polarization. This is consistent with the rapid reduction of the polarization with increasing temperature. An additional confirmation of this scenario is obtained by observation of thermal history effects, which are characteristic to frozen states. As shown in Fig. 2(a), the polarization of the system poled on cooling down to $T = 2$ K (filled circles) significantly exceeds the polarization of the sample poled at $T = 3.1$ K (open circles), when the polarization is subsequently measured on warming in zero field. This is a typical behavior of a frozen system undergoing slow relaxation processes. This scenario is also consistent with the absence of any sharp anomaly of $\epsilon_c(T)$ at the magnetic transition. We conclude, therefore, that in $\text{Ca}_3(\text{Co}, \text{Mn})_2\text{O}_6$, thermal fluctuations of the magnetoelec-

tric clusters tend to suppress the macroscopic polarization, leading to the complex temperature dependences and thermal history effects observed in the experiments.

In summary, we report discovery of an unambiguous example of magnetism-driven ferroelectricity with a collinear magnetic order in the Ising chain magnet $\text{Ca}_3\text{Co}_{2-x}\text{Mn}_x\text{O}_6$ ($x \approx 0.96$). The ferroelectricity originates from the simultaneous presence of the alternating order of Co and Mn ions and the spin order with the $\uparrow\downarrow\downarrow$ configuration. This provides the first experimental realization of theoretically predicted ferroelectricity in a frustrated Ising chain with an ionic order. Unlike in well-known spiral magnetoelectrics, symmetric exchange striction is expected to drive the ferroelectricity in this system.

Work at Rutgers was supported by the DOE under Grant No. DE-FG02-07ER46382. S.L. was partially supported by the Korea Science and Engineering Foundation through the Center for Strongly Correlated Materials Research at Seoul National University.

- [1] D.I. Khomskii, *J. Magn. Magn. Mater.* **306**, 1 (2006).
- [2] S.-W. Cheong and M. Mostovoy, *Nat. Mater.* **6**, 13 (2007).
- [3] N. Hur *et al.*, *Nature (London)* **429**, 392 (2004).
- [4] T. Goto *et al.*, *Phys. Rev. Lett.* **92**, 257201 (2004).
- [5] N. Hur *et al.*, *Phys. Rev. Lett.* **93**, 107207 (2004).
- [6] T. Kimura *et al.*, *Nature (London)* **426**, 55 (2003).
- [7] G. Lawes *et al.*, *Phys. Rev. Lett.* **95**, 087205 (2005).
- [8] T. Kimura *et al.*, *Phys. Rev. B* **73**, 220401(R) (2006).
- [9] T. Kimura *et al.*, *Phys. Rev. Lett.* **94**, 137201 (2005).
- [10] Y. Yamasaki *et al.*, *Phys. Rev. Lett.* **96**, 207204 (2006).
- [11] K. Taniguchi *et al.*, *Phys. Rev. Lett.* **97**, 097203 (2006).
- [12] S. Park *et al.*, *Phys. Rev. Lett.* **98**, 057601 (2007).
- [13] H. Katsura *et al.*, *Phys. Rev. Lett.* **95**, 057205 (2005).
- [14] M. Mostovoy, *Phys. Rev. Lett.* **96**, 067601 (2006).
- [15] I. A. Sergienko and E. Dagotto, *Phys. Rev. B* **73**, 094434 (2006).
- [16] A. B. Harris *et al.*, *Phys. Rev. B* **73**, 184433 (2006).
- [17] L. C. Chapon *et al.*, *Phys. Rev. Lett.* **96**, 097601 (2006).
- [18] Y. Noda *et al.*, *Physica B (Amsterdam)* **385–386**, 119 (2006).
- [19] H. Kimura *et al.*, *J. Phys. Soc. Jpn.* **75**, 113701 (2006).
- [20] I. A. Sergienko *et al.*, *Phys. Rev. Lett.* **97**, 227204 (2006).
- [21] B. Lorentz *et al.*, *Phys. Rev. B* **76**, 104405 (2007).
- [22] M. E. Fisher and W. Selke, *Phys. Rev. Lett.* **44**, 1502 (1980).
- [23] S. Rayaprol *et al.*, *Solid State Commun.* **128**, 79 (2003).
- [24] V. G. Zubkov *et al.*, *Solid State Commun.* **160**, 293 (2001).
- [25] A. Maignan *et al.*, *Eur. Phys. J. B* **15**, 657 (2000).
- [26] J. Rodriguez-Carvajal, *Physica B (Amsterdam)* **192**, 55 (1993).
- [27] J. A. Mydosh, *Spin Glasses. An Experimental Introduction.* (Taylor & Francis, London, 1993).

Appendix VI.

Multiferroicity in the square-lattice antiferromagnet of $\text{Ba}_2\text{CoGe}_2\text{O}_7$

H. T. Yi,^{1,2} Y. J. Choi,¹ S. Lee,¹ and S.-W. Cheong^{1,2,a)}

¹Rutgers Center for Emergent Materials and Department of Physics and Astronomy, Rutgers University, Piscataway, New Jersey 08854, USA

²Department of Electrical and Computer Engineering, Rutgers University, Piscataway, New Jersey 08854, USA

(Received 20 February 2008; accepted 6 May 2008; published online 27 May 2008)

We have discovered the appearance of ferroelectricity below the Neel temperature of 6.7 K in the antiferromagnetic $\text{Ba}_2\text{CoGe}_2\text{O}_7$ with square magnetic lattice. The ferroelectric polarization is rather small in magnitude and aligned along the c axis, but its magnitude increases remarkably and its direction rotates away smoothly from the c axis when magnetic fields are applied along the c axis. The electric polarization's behavior of smooth rotation, rather than a sudden flip, is unique. It also accompanies a linear increase in magnetization and a smooth change of dielectric constant with little hysteresis, which may be important for certain technological applications. © 2008 American Institute of Physics. [DOI: 10.1063/1.2937110]

The recent renaissance of research on multiferroics, where magnetic order and ferroelectricity coexist, has been invigorated by scientific discoveries of significant cross coupling between spin and lattice degrees of freedom as well as potentials for device applications such as ferroelectric memory tunable by magnetic fields or magnetic memory controlled by electric fields.^{1–5} The remarkable cross-coupling effects in multiferroics include reversible flipping of ferroelectric polarization or drastic changes in the dielectric constant with applied magnetic fields.^{4–6} These recently discovered effects have been observed in the so-called “magnetism-driven ferroelectrics.” Magnetic order is developed with the loss of inversion symmetry in the magnetic lattice. Lattice relaxation occurs through exchange striction in the magnetically ordered state and thus the crystallographic lattice naturally loses inversion symmetry. Ferroelectricity is developed by this mechanism in magnetism-driven ferroelectrics. Spiral magnetic order, resulting from magnetic frustration, is a common way to induce the loss of magnetic inversion symmetry and magnetism-driven ferroelectricity has been observed in a number of spiral magnets such as TbMnO_3 , $\text{Ni}_3\text{V}_2\text{O}_8$, MnWO_4 , CuFeO_2 , CoCr_2O_4 , and LiCu_2O_2 .^{4,7–12} Note that the “antisymmetric” part of exchange coupling, known as the Dzyaloshinski–Moriya (DM) interaction, becomes active when ferroelectricity is induced by spiral magnetic order in noncollinear magnets. Alternatively, ferroelectricity can result from lattice relaxation through exchange striction associated with the “symmetric” part of the exchange coupling. This kind of multiferroicity has been found in Ising magnets such as $\text{Ca}_3(\text{Co,Mn})_2\text{O}_6$.¹³

The compound $\text{Ba}_2\text{CoGe}_2\text{O}_7$ crystallizes in a tetragonal structure with a square magnetic lattice. The crystal structure of $\text{Ba}_2\text{CoGe}_2\text{O}_7$ is characterized as a $p4_21m$ crystallographic space group with a unit cell of $a=b=0.8410$ nm and $c=0.5537$ nm at 10 K.¹⁴ However, the magnetic ground state of $\text{Ba}_2\text{CoGe}_2\text{O}_7$ is concluded as an in-planar antiferromagnetic order below the Neel temperature of $T_N=6.7$ K.^{14–16} It has been postulated that the DM vector in $\text{Ba}_2\text{CoGe}_2\text{O}_7$ alternates its direction along [001], resulting in the in-planar

antiferromagnetic order with an in-plane weak ferromagnetic component.¹⁵ Neutron scattering results on $\text{Ba}_2\text{CoGe}_2\text{O}_7$ suggest the presence of commensurate and collinear magnetic order with spins antiferromagnetically pointing along the b axis.¹⁴ The presence of two types of DM vectors in the square-lattice antiferromagnets suggests that the system can be an intriguing candidate for multiferroicity. Indeed, we discovered that ferroelectric polarization develops below T_N of $\text{Ba}_2\text{CoGe}_2\text{O}_7$, and exhibits a remarkable increase in magnitude as well as a smooth rotation of direction with external magnetic fields.

A single crystal of $\text{Ba}_2\text{CoGe}_2\text{O}_7$ (6 mm in diameter and 50 mm in length) was grown using a floating zone method. For the feed rods, a solid-state reaction method was employed in air. dc magnetization was measured using a superconducting quantum interference device magnetometer; the Quantum Design magnetic property measurement system. We measured specific heat using the standard relaxation method with the Quantum Design physical properties measurement system. The experiments for the dielectric constant (ϵ) on polished crystals (4.2×3.5 mm² in the a - b plane by 0.306 mm along the c axis for the c -direction measurement, and 3.2×2.4 mm² in the b - c plane by 0.324 mm along the a axis for the a -direction measurement) were performed using an LCR meter at 44 KHz. The pyroelectric current to obtain polarization was measured with an electrometer during a warming process (at a rate of 4 K/min) after poling samples from 40 to 2 K in the electric field of ~ 7 kV/cm.

Magnetization (M) behavior of our crystal is consistent with the results in literature.¹⁴ Figure 1(a) shows the zero-field-cooled (ZFC) and field-cooled (FC) magnetization curves in $B=0.2$ T (parallel to the c and a axes). A sharp step appears at 6.7 K (T_N) with a significant magnetic anisotropy. The large M/B (magnetization/external magnetic field) along the tetragonal a axis indicates that the system is an easy-planar magnet. The steplike increase in M/B along the a axis, below T_N , is much larger than that along the c axis. This suggests the appearance of a weak ferromagnetic moment, predominantly, in the a - b plane. As shown in Fig. 1(c), magnetization ($\mu_B/\text{f.u.}$) increases linearly with increasing external magnetic field, B . However, the residual magnetization extrapolated to $B=0$ is found to be nonzero; about

^{a)} Author to whom correspondence should be addressed. Electronic mail: sange@physics.rutgers.edu.

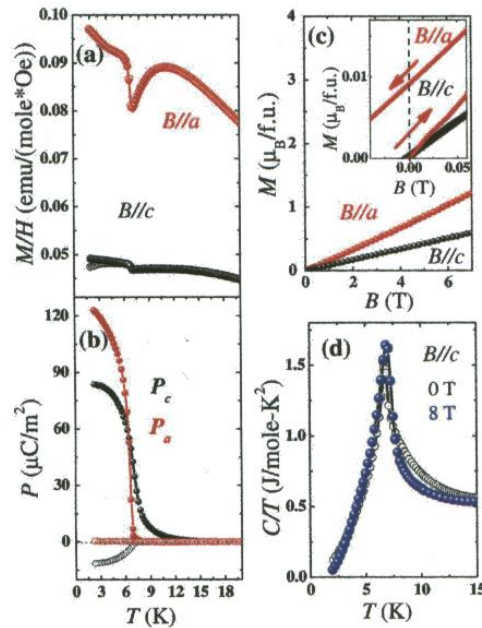


FIG. 1. (Color online) (a) Temperature dependence of magnetic susceptibility measured in 0.2 T applied along the c axis (black) and the a axis (red): open and filled circles represent ZFC and FC data, respectively. (b) Temperature dependence of polarization along the a (red) and c (black) axes in $B=0$ (open circle) and $B=8$ T (filled circle). (c) Magnetization ($\mu_B/f.u.$) at 2 K in fields along the c (black) and a (red) axes: a magnified figure near $B=0$ is shown in the inset. (d) The temperature dependence of specific heat divided by temperature in $B=0$ (black) and 8 T (blue).

0.009 $\mu_B/f.u.$ and 0.0005 $\mu_B/f.u.$ at 2 K along the a and c axes, respectively, as shown in the inset of Fig. 1(c). This result is consistent with the behavior of the steplike M/B increase below T_N in Fig. 1(a). This residual moment, mostly along the a axis, may be consistent with the presence of the [001]-direction DM vector.

We discovered that the magnetic transition accompanies the appearance of electric polarization (P). The temperature (T) dependences of P along the c axis (P_c) and along the a axis (P_a) in $B_c=0$ (open circles) and $B_c=8$ T (filled circles) are shown in Fig. 1(b). The magnitude of P_c is $\sim -11 \mu C/m^2$ in $B_c=0$ and $\sim 80 \mu C/m^2$ in 8 T, while the P_a value changes from ~ 0 to $\sim 120 \mu C/m^2$ in $B_c=0$ and 8 T, respectively. A small electric polarization exists only along the c axis in $B_c=0$. At 8 T, a large polarization appears in both a and c axes. Note that the negative sign of the small polarization in $B_c=0$ may suggest the presence of unusual pinning of ferroelectric domains during the poling process. A sharp peak in specific heat curve (C/T versus T) is observed at T_N and changes little with $B_c=8$ T, as shown in the inset of Fig. 1(d).

The details of the external magnetic field along c axis (B_c)-dependent dielectric properties of $Ba_2CoGe_2O_7$ are shown in Fig. 2. The T dependence of dielectric constants along the c axis, ϵ_c , and along the a axis, ϵ_a , in various B_c is displayed in Figs. 2(a) and 2(b), respectively. With decreasing temperature, ϵ_c in $B_c=0$ increases sharply below T_N , and tends to saturate at low temperatures. The temperature-induced change of ϵ_c decreases with increasing B_c , and be-

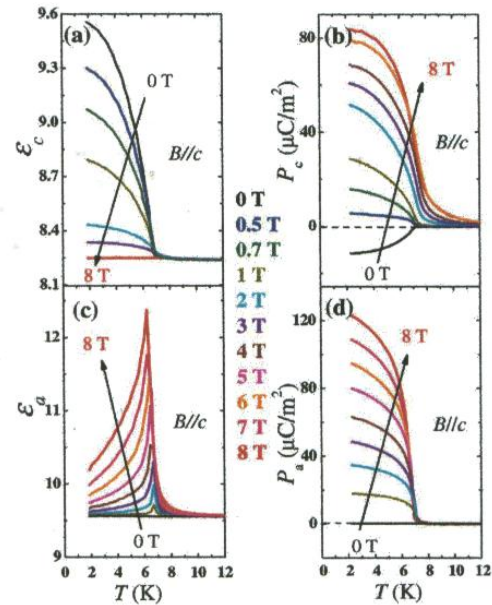


FIG. 2. (Color online) [(a), (b), (c), and (d)] Temperature dependences of the c -direction dielectric constant, the a -direction dielectric constant, the c -direction polarization, and the a -direction polarization in various applied magnetic fields ($B=0$ to 8 T) along the c axis.

comes only $\sim 0.24\%$ in $B_c=8$ T. On the other hand, ϵ_a does not show any anomaly at T_N in $B=0$, but in $B_c > 0$, a sharp ϵ_a peak appears at T_N , and the magnitude of the peak increases with increasing B_c . Consistent with earlier discussion, polarization along c axis in $B_c=0$ shows nonzero, but small value below T_N , and builds smoothly with increasing external magnetic field, Fig. 2(c). Polarization along a axis is zero in $B_c=0$, but increases smoothly with increasing B_c .

Figures 3(b) and 3(d) show the isothermal change of P_a and P_c with varying B_c at 2 K. The measurement was made with three sequential procedures; $B_c=0$ to 8 T (route 1, red), 8 to -8 T (route 2, black), and -8 to 8 T (route 3, blue). The simultaneous presence of nonzero P_a and P_c in finite indicates that the true electric polarization vector lies on the a - c plane, but away from the c axis. The external magnetic field along c axis dependence of the polarization vector for route 1 is displayed in Fig. 3(a). With increasing B_c , polarization value increases and at the same time rotates smoothly away from the c axis. Note that P_a keeps increasing with increasing B_c up to our maximum measuring field of 8 T, while the increasing of P_c tends to saturate for $B_c > \sim 2$ T. This polarization behavior corroborates with the external magnetic field dependence of ϵ_c and ϵ_a , shown in Figs. 3(c) and 3(e): ϵ_c at 2 K changes sharply in low B_c , and saturates for $B_c > \sim 2$ T, but ϵ_a at 2 K keeps changing in the entire range of external magnetic field up to 8 T. Note that we have not observed any significant change in the dielectric properties in $Ba_2CoGe_2O_7$ when magnetic fields were applied along the a or b axis.

We emphasize that the smooth rotation of polarization with external magnetic fields in $Ba_2CoGe_2O_7$, summarized in Fig. 3(a), is rather unique. In other magnetism-driven multiferroics, Electric polarization tends to flip suddenly by 90°

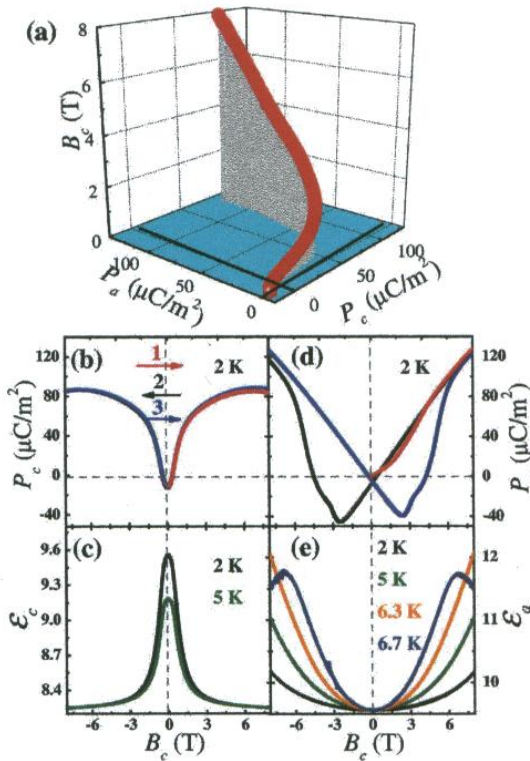


FIG. 3. (Color online) (a) Variation of polarization vector with magnetic fields ($B_c=0-8$ T) along the c axis. This plot is obtained from results in (b) and (d). (b) External magnetic field dependence of the c -direction polarization at 2 K: red, black, and blue lines are obtained from measurements with field sweeps from $B=0$ to 8 T, 8 to -8 T, and -8 to 8 T, respectively. (c) External magnetic field dependence of the c -direction dielectric constants at 2 K (black) and 5 K (green). (d) B_c dependence of the a -direction polarization at 2 K: red, black, and blue lines are obtained from measurements with field sweeps from 0 to 8 T, 8 to -8 T, and -8 to 8 T, respectively. (e) B_c dependence of the a -direction dielectric constants at 2 K (black), 5 K (green), 6.3 K (orange), and 6.7 K (blue). All data in (b)–(e) show the results for the entire B_c sweeps from $0 \rightarrow 8$ T $\rightarrow -8$ T $\rightarrow 8$ T.

(TbMnO_3 , DyMnO_3 , MnWO_4 , and LiCu_2O_2) or 180° (TbMn_2O_5) through first-order phase transitions when sufficiently large magnetic fields are applied.^{3–5,7–9} $M(B)$ curves of $\text{Ba}_2\text{CoGe}_2\text{O}_7$, Fig. 1(c), do not show any hint of an external magnetic field-induced phase transition. In addition, there exists no hint of any first-order phase transition in the external magnetic field dependence of P_c , ϵ_a , and ϵ_c . This unique behavior may be related to the possible presence of two types of the DM vectors in the square-lattice structure of $\text{Ba}_2\text{CoGe}_2\text{O}_7$; one along $[1\bar{1}0]$ and the other along $[001]$. Detailed investigation of the exact magnetic structure in external magnetic field will be needed to unveil the origin of the intriguing multiferroic behavior in $\text{Ba}_2\text{CoGe}_2\text{O}_7$.

It is also noteworthy that there exists little hysteresis in the external magnetic field dependence of P_c , ϵ_a , and ϵ_c

(except P_a : the hysteretic behavior of P_a with external magnetic field may be related to ferroelectric domain pinning, rather than a first-order phase transition) [see Figs. 3(b)–3(e)]. The external magnetic field-induced change of dielectric properties in multiferroics can be of use for technological devices, but a large field hysteresis can be detrimental for many applications. Since the drastic control of polarization and dielectric constant with external magnetic field in many multiferroics occurs through first-order phase transitions, a large field hysteresis is commonly accompanied. However, the field hysteresis of the external magnetic field-induced change of P_c , ϵ_a , and ϵ_c in $\text{Ba}_2\text{CoGe}_2\text{O}_7$ appears to be minimal: the hysteretic variation, defined as the change of polarization or dielectric constant with different field sweeps normalized by the difference of P or ϵ in $B_c=0$ and 8 T, is less than 1.04% for ϵ_a , ($<1.12\%$ for ϵ_c and $<3.7\%$ for P_c).

In summary, we found that ferroelectricity develops below T_N in $\text{Ba}_2\text{CoGe}_2\text{O}_7$, and ferroelectric polarization is along the tetragonal c axis. The polarization increases significantly in magnitude and rotates away from the c axis when magnetic fields are applied along the c axis. This change of polarization and the associated change of dielectric constant with fields are smooth without going through any phase transition, and thus is involved with little field hysteresis. Exploration of this negligible external magnetic field-hysteresis effect will be indispensable toward the practical potential of multiferroics.

This work was supported by the MRSEC NSF-DMR-0520471.

- ¹S.-W. Cheong and M. Mostovoy, *Nat. Mater.* **6**, 13 (2007).
- ²D. I. Khomskii, *J. Magn. Magn. Mater.* **306**, 1 (2006).
- ³T. Goto, T. Kimura, G. Lawes, A. P. Tamiere, and Y. Tokura, *Phys. Rev. Lett.* **92**, 257201 (2004).
- ⁴T. Kimura, T. Goto, H. Shintani, K. Ishizaka, T. Arima, and Y. Tokura, *Nature (London)* **426**, 55 (2003).
- ⁵N. Hur, S. Park, P. A. Sharma, J. S. Ahn, S. Guha, and S.-W. Cheong, *Nature (London)* **429**, 392 (2004).
- ⁶N. Hur, S. Park, P. A. Sharma, S. Guha, and S.-W. Cheong, *Phys. Rev. Lett.* **93**, 107207 (2004).
- ⁷T. Arima, A. Tokunaga, T. Goto, H. Kimura, Y. Noda, and Y. Tokura, *Phys. Rev. Lett.* **96**, 097202 (2006).
- ⁸S. Park, Y. J. Choi, C. L. Zhang, and S.-W. Cheong, *Phys. Rev. Lett.* **98**, 057601 (2007).
- ⁹K. Taniguchi, N. Abe, T. Takenobu, Y. Iwasa, and T. Arima, *Phys. Rev. Lett.* **97**, 097203 (2006).
- ¹⁰G. Lawes, A. B. Harris, T. Kimura, N. Rogado, R. J. Cava, A. Aharony, O. Entin-Wohlman, T. Yildirim, M. Kenzelmann, C. Broholm, and A. P. Ramirez, *Phys. Rev. Lett.* **95**, 087205 (2005).
- ¹¹T. Kimura, J. C. Lashley, and A. P. Ramirez, *Phys. Rev. B* **73**, 220401(R) (2006).
- ¹²Y. Yamasaki, S. Miyasaka, Y. Kaneko, J.-P. He, T. Arima, and Y. Tokura, *Phys. Rev. Lett.* **96**, 207204 (2006).
- ¹³Y. J. Choi, H. T. Yi, S. Lee, Q. Huang, V. Kiryukhin, and S.-W. Cheong, *Phys. Rev. Lett.* **100**, 047601 (2008).
- ¹⁴A. Zheludev, T. Sato, T. Masuda, K. Uchinokura, G. Shirane, and B. Roesli, *Phys. Rev. B* **68**, 024428 (2003).
- ¹⁵T. Sato, T. Masuda, and K. Uchinokura, *Physica B* **329–333**, 880 (2003).
- ¹⁶A. N. Bogdanov, U. K. Rossler, M. Wolf, and K.-H. Muller, *J. Magn. Magn. Mater.* **272–276**, 332 (2004).

Appendix VII.

PRL 102, 067601 (2009)

PHYSICAL REVIEW LETTERS

week ending
13 FEBRUARY 2009

Thermally or Magnetically Induced Polarization Reversal in the Multiferroic CoCr_2O_4

Y. J. Choi,¹ J. Okamoto,² D. J. Huang,^{2,3} K. S. Chao,^{2,4} H. J. Lin,² C. T. Chen,² M. van Veenendaal,⁵
T. A. Kaplan,⁶ and S.-W. Cheong¹¹*Rutgers Center for Emergent Materials and Department of Physics and Astronomy,
136 Frelinghuysen Road, Piscataway, New Jersey 08854, USA*²*National Synchrotron Radiation Research Center, Hsinchu 30076, Taiwan*³*Department of Physics, National Tsing Hua University, Hsinchu 30013, Taiwan*⁴*Department of Electrophysics, National Chiao Tung University, Hsinchu 30010, Taiwan*⁵*Department of Physics, Northern Illinois University, De Kalb, Illinois 60115, USA,**and Advanced Photon Source, Argonne National Laboratory, 9700 South Cass Avenue, Argonne, Illinois 60439, USA*⁶*Department of Physics and Astronomy, Michigan State University, East Lansing, Michigan 48824, USA*

(Received 28 May 2008; published 9 February 2009)

We report the unexpected evolution, with thermal and magnetic-field (H) variations, of the interrelation between the polarization \mathbf{P} , magnetization \mathbf{M} , and spiral wave vector \mathbf{Q} in CoCr_2O_4 , which has a ferrimagnetic conical-spiral magnetic order. For example, \mathbf{P} suddenly jumps and changes its sign at the magnetic lock-in transition (T_L) with thermal variation, or with isothermal variation of H (without changing its direction) at T_L , which surprisingly occurs without change in spiral handedness (i.e., the sign of \mathbf{Q}). The presence of multiple spiral sublattices may be behind this unusual behavior.

DOI: 10.1103/PhysRevLett.102.067601

PACS numbers: 77.80.-e, 77.22.Ej, 75.80.+q, 78.70.Ck

Magnetically driven ferroelectrics where magnetic order with broken inversion symmetry accompanies the occurrence of ferroelectric polarization have been of great recent interest [1,2], the first example of which was reported by Newnham *et al.* [3]. Recently, the high tunability of dielectric properties by applied magnetic fields (H), such as reversibly flipping ferroelectric polarization or a drastic change of dielectric constant, has been found in such materials [4]. Spinel CoCr_2O_4 , which shows a complex conical-spiral ferrimagnetic spin order [5], is unique among such materials [3,6–10] in that it has a spontaneous magnetization \mathbf{M} ; the spiral component induces the observed electric polarization \mathbf{P} [8] in common with the others. In addition to \mathbf{M} and \mathbf{P} , a multiferroic domain is characterized by the spiral wave vector \mathbf{Q} , and single such

domains can be produced by poling. Here we report the first comprehensive study of the switching behavior of these domains under a variation of applied H , and temperature (T). We find that \mathbf{Q} dependence of \mathbf{P} differs from that expected from previous simpler spiral orderings, where a change in $\text{sgn}(\mathbf{P})$ accompanies a change in $\text{sgn}(\mathbf{Q})$.

CoCr_2O_4 crystallizes in a cubic spinel structure, magnetic Co^{2+} and Cr^{3+} ions occupying the tetrahedral (A) and octahedral (B) sites, respectively [Fig. 1(a)]. For nearest-neighbor and isotropic antiferromagnetic A - B and B - B exchange interactions (J_{AB} and J_{BB}), with $J_{BB}/J_{AB} > 2/3$, an approximate, variational solution for the ground state was found, a "ferrimagnetic spiral," where the spins lie on conical surfaces [11–13]: The spins on the 6 fcc sublattices containing the magnetic sites are given by

$$\mathbf{S}_{n\nu} = \sin\theta_\nu [\hat{x} \cos(\mathbf{Q} \cdot \mathbf{r}_{n\nu} + \gamma_\nu) + \hat{y} \sin(\mathbf{Q} \cdot \mathbf{r}_{n\nu} + \gamma_\nu)] + \hat{z} \cos\theta_\nu, \quad 0 \leq \theta_\nu \leq \pi, \nu = 1, \dots, 6. \quad (1)$$

For fixed ν , $\mathbf{r}_{n\nu}$ goes over the sites of sublattice ν , the values of the cone $\frac{1}{2}$ -angle θ_ν and phase γ_ν depend on ν , and the wave vector $\mathbf{Q} \cong 0.6$ [110], in units of $2\pi/\text{lattice constant}$, is along the crystallographic [110]; \hat{x} , \hat{y} , \hat{z} are orthonormal vectors [11–13] [see Fig. 1(a)].

A state approximately of this form was found from neutron diffraction in CoCr_2O_4 [5,14], with \hat{z} the [001] crystal direction when \mathbf{Q} is in the $+$ or $-$ [110] direction, "[110] \mathbf{Q} domains" (with the same relative orientation for the cubically equivalent \mathbf{Q} 's). In [110] domains, the z components produce the magnetization \mathbf{M} (along \pm [001]). According to Yamasaki *et al.* [8], the spiral components give rise to ferroelectricity, where $\mathbf{P} \propto \mathbf{e}_{12} \times (\mathbf{S}_1 \times \mathbf{S}_2)$ for a pair of spins \mathbf{S}_1 and \mathbf{S}_2 with rela-

tive displacement \mathbf{e}_{12} [15–17]. For the spiraling components of the Cr spins lying along the [110] chains, shown in Fig. 1(a), this gives the same contribution for every nearest-neighbor pair, namely $\mathbf{P} \propto \mathbf{Q} \times [001] \propto [\bar{1}10]$, as seen in Fig. 1(a) and as observed [8].

Magnetic measurement was performed in a SQUID magnetometer, specific heat was measured using a Quantum Design PPMS, and the dielectric constant, ϵ , was measured using an LCR meter at $f = 44$ kHz. The $T(H)$ dependence of electric polarization, \mathbf{P} , was obtained by the integration of a pyroelectric (magnetoelectric) current measured using an electrometer with the $T(H)$ variation of 4 K/min (0.01–0.02 T/s). While poling in $E \approx 10$ kV/cm, a small static H ($H = 0.5$ T for Fig. 2)

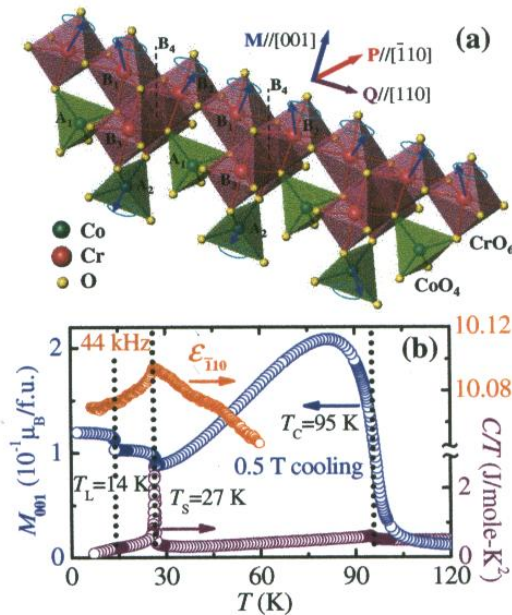


FIG. 1 (color online). (a) Crystallographic and low- T magnetic structure of spinel CoCr_2O_4 . Co^{2+} and Cr^{3+} ions are located at the center of tetrahedral and octahedral O_2^- cages, respectively. Conical-spiral spins of Co^{2+} and Cr^{3+} ions for only 3 of the 6 sublattices (A_2 , B_1 , and B_2) are shown for clarity. Cone angles shown are from [12], which, with [13], should be consulted for more details. Also shown are the directions of \mathbf{M} , \mathbf{P} , and \mathbf{Q} . (b) T dependence of magnetization, \mathbf{M} , along the $[001]$ direction in $H = 0.5 \text{ T}$ upon cooling, specific heat divided by temperature in $H = 0 \text{ T}$ upon cooling, and dielectric constant in $H = 0 \text{ T}$ at 44 kHz upon warming. The existence of three phase transitions is evident, and T_C , T_S , and T_L denote temperatures for ferrimagnetic transition, conical spin ordering, and lock-in transition, respectively.

was also applied along the magnetic easy axis, along $[001]$, so this magnetoelectric cooling procedure with E and H fixes the directions of the possible \mathbf{M} , \mathbf{P} , and \mathbf{Q} ; i.e., the procedure chooses a single $(\mathbf{M}, \mathbf{P}, \mathbf{Q})$ domain.

The T dependence of physical properties of our single-crystalline CoCr_2O_4 , grown with a vapor-transport method [18], exhibits sharp features, indicative of three phase transitions, as displayed in Fig. 1(b). The long-range ferrimagnetic collinear spin order appears below $T_C = 95 \text{ K}$. A sharp but continuous increase of $M(T)$ at $T_S = 27 \text{ K}$ is ascribed to the conical-spiral order of spins, going along with a sharp peak in the specific heat, $C(T)$, and a peaky anomaly in $\epsilon(T)$ along the $[\bar{1}\bar{1}0]$ direction where the electric polarization emerges. A steplike jump of $M(T)$ at $T_L = 14 \text{ K}$ [see also Fig. 2(a)], accompanied by a small feature in $C(T)$ and $\epsilon(T)$, is associated with a small but clear thermal hysteresis (not shown), indicating the 1st order nature of this transition.

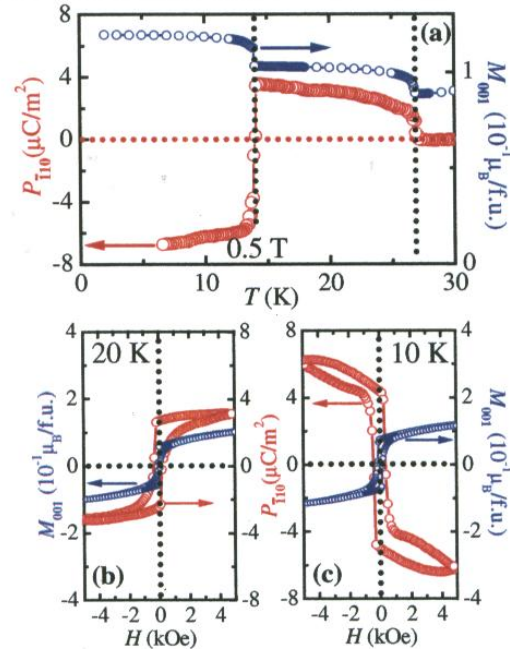


FIG. 2 (color online). (a) T dependence of electric polarization, \mathbf{P} , along the $[\bar{1}\bar{1}0]$ direction, and \mathbf{M} along the $[001]$ direction below 30 K . \mathbf{P} suddenly switches sign when cooling across 14 K without changing the signs of \mathbf{M} and \mathbf{Q} . (b) and (c) H dependence of \mathbf{M} and \mathbf{P} at 20 K and 10 K , respectively. The reversal of all of \mathbf{M} , \mathbf{P} , and \mathbf{Q} is achieved by H reversal.

The onset of ferroelectricity along the $[\bar{1}\bar{1}0]$ direction, matches the spiral magnetic ordering transition at $T_S = 27 \text{ K}$ [Fig. 2(a)]. At the 14 K transition, when \mathbf{M} is kept in one direction with H , \mathbf{P} suddenly flips its direction, in contrast to the previous finding [8]. But in agreement with [8], when H , and therefore \mathbf{M} , is reversed at fixed T , we find \mathbf{P} to be reversed, as seen in Figs. 2(b) and 2(c). This correlation between \mathbf{M} and \mathbf{P} was attributed [8] to Bloch domain wall motion involved in reversing \mathbf{M} . Such an essentially uniform rotation of the spin state characterizing the wall, taking \mathbf{M} to $-\mathbf{M}$, can be seen to take a \mathbf{Q} domain to a $-\mathbf{Q}$ domain [19]. We have observed directly this sign change of \mathbf{Q} upon H reversal by our circularly polarized resonant magnetic x-ray scattering experiment. Thus, \mathbf{M} , \mathbf{P} , and \mathbf{Q} change to $-\mathbf{M}$, $-\mathbf{P}$, $-\mathbf{Q}$ in $-H$, respectively [Fig. 2(b)]. Furthermore, at 10 K (below T_L), H reversal also induces the 180° flipping of \mathbf{M} , $-\mathbf{P}$, and \mathbf{Q} [Fig. 2(c)].

In contrast to this behavior, we find that the sign flip of \mathbf{P} across the 14 K transition is not accompanied by a change of $\text{sgn}(\mathbf{Q})$; rather our results indicate that the sign of \mathbf{Q} (or spiral handedness) is invariant at the 14 K transition (discussed further below). The low-temperature state is asso-

ciated with a slight increase of the magnitude of \mathbf{M} as well as \mathbf{P} , as shown in Fig. 2(a). Note that in a multiferroic with a spiral magnetic order with only one magnetic sublattice, switching of \mathbf{P} results from a sign change of \mathbf{Q} [20]. (This is the usual behavior found in other multiferroics with spiral magnetism.)

Our resonant magnetic soft x-ray scattering experiment was performed with the elliptically polarized-undulator beam line at the National Synchrotron Radiation Research Center in Taiwan. With photon energy tuned at the Co L_3 edge, the scattering results reveal that there is an abrupt change in magnetic modulations at ~ 14 K. Unlike earlier neutron results [5,14,21], we found two incommensurate magnetic modulations \mathbf{Q}_+ and \mathbf{Q}_- at 15 K, a temperature above T_L , while, for T below T_L , there are one commensurate modulation $\mathbf{Q}_C = 2/3[110]$ and two incommensurate ones, \mathbf{Q}'_+ and \mathbf{Q}'_- , with a separation along $[1\bar{1}0]$ much larger than that between \mathbf{Q}_+ and \mathbf{Q}_- , as illustrated in the contour plots [Fig. 3(a)]. The intensities of the \mathbf{Q}' peaks are 1 to 2 orders of magnitude smaller than the \mathbf{Q}_C peak, and the three vectors are approximately equal in direction as well as magnitude; similarly, the vectors \mathbf{Q}_+ , \mathbf{Q}_- are approximately equal [Fig. 3(a)]. The x-ray scattering intensity can distinguish between spirals with wave vector \mathbf{Q} and $-\mathbf{Q}$, if the incident beam is circularly polarized [22]. This is similar to the scattering of polarized neutrons [20,23]. Figures 3(b), 3(d), and 3(e) show that the measured scattering intensities with circularly polarized light indeed change upon the reversal of magnetization along $[001]$, disclosing the expected flip of \mathbf{Q} with H reversal. Figure 3(c) also illustrates conical-spiral spins above and below the 14 K transition where $\pm\mathbf{M}$ correspond to $\pm\mathbf{Q}$, respectively. Strikingly, the scattering results also reveal that the sign of the \mathbf{Q} of the largest peak at each T (\mathbf{Q}_C and \mathbf{Q}_-) remains unchanged as T changes across T_L : The H dependences of the intensities of these peaks do not reverse. Thus, to the extent that we can consider a single-wave-vector spiral as a good approximation to the observed state, this is solid evidence of $\text{sgn}(\mathbf{Q})$ invariance across T_L . In addition, the only one of the smaller peaks (\mathbf{Q}'_+) that has an observable intensity change on H reversal also shows this invariance, and further, the wave vectors of all the peaks are approximately equal. Therefore, even considering the complexity of having multiple Fourier components in the spin configuration, the data strongly suggest that the sign of \mathbf{Q} (for each Fourier component) does not change across the 1st order transition.

A plausible interpretation for the switch in the sign of \mathbf{P} across 14 K without sign change of \mathbf{Q} and \mathbf{M} (despite its impossibility for a single sublattice conical spiral, as noted above) is found in a “ferrielectric”-type scenario. Now, Co^{2+} has a more-than-half-filled d shell, while Cr^{3+} has a less-than-half-filled shell, suggesting that Co-Cr and Cr-Cr bonds have the opposite sign of spin-orbit interaction, resulting in the opposite directions of electric dipole moments, $\mathbf{P}_{\text{Co-Cr}}$ and $\mathbf{P}_{\text{Cr-Cr}}$ from the different bonds of form Eq. (1) [24]. Furthermore, the bond charges that give rise to

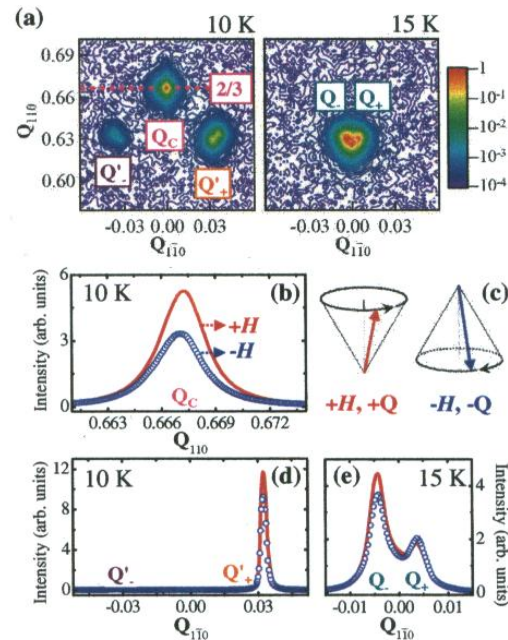


FIG. 3 (color online). (a) Contour plots of the Co L_3 edge magnetic soft x-ray scattering intensity in the plane defined by \mathbf{Q}_{110} and $\mathbf{Q}_{\bar{1}\bar{1}0}$ recorded at temperatures above and below T_L (14 K) with photon energy of 778.4 eV. The \mathbf{E} vector of incident x-rays was parallel to the $[001]$ axis. The contour plots are shown in a logarithmic scale with its order of magnitude expressed by means of color. (b), (d), and (e) Scattering intensity of \mathbf{Q} scans along $[110]$ and $[\bar{1}\bar{1}0]$ under $+\mathbf{M}$ (solid curves) and $-\mathbf{M}$ (open circles) with circularly polarized x-rays. (c) Depiction of conical-spiral spins where $\pm\mathbf{M}$ go with $\pm\mathbf{Q}$ above and below T_L , respectively.

the dipole moments are interionic overlap charge densities [15,16], and are therefore very sensitive to small changes in interionic distances expected to occur through the 1st order phase transition at T_L . Then, it is conceivable that the delicately balanced net polarization can change its sign at T_L without a change in $\text{sgn}(\mathbf{Q})$ (the directions of each contribution $\mathbf{P}_{\text{Co-Cr}}$ and $\mathbf{P}_{\text{Cr-Cr}}$ do not change, but their magnitudes do).

Repeated switching of electric polarization direction is achieved by varying temperature step-linearly with time between 8 K and 20 K as shown in Fig. 4(a). The measurement of the pyroelectric current began at 8 K in the $(+, -, +)$ state defined as $[\text{sgn}(\mathbf{M}), \text{sgn}(\mathbf{P}), \text{sgn}(\mathbf{Q})]$ after poling in $H = 0.1$ T and $E \approx 10$ kV/cm. Upon warming, this state switches to the $(+, +, +)$ state, but the initial state is recovered by cooling back to 8 K. Because of the 1st order nature of the T_L transition, the temperatures at which \mathbf{P} flips differ by ~ 1.6 K between warming and cooling. Figure 4(b) displays how $\mathbf{P}(T)$ depends on large

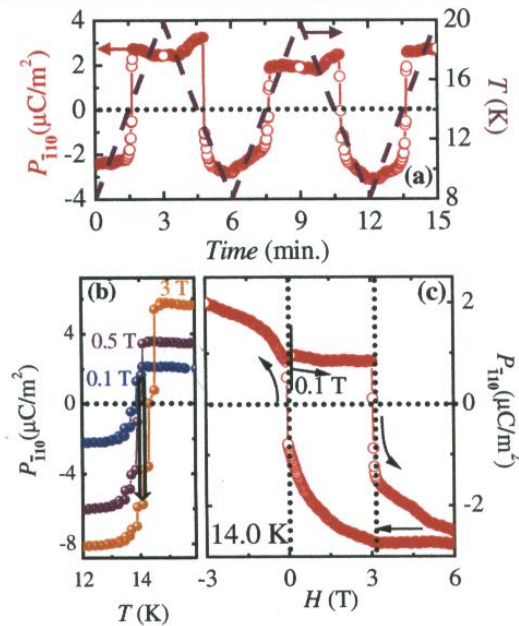


FIG. 4 (color online). (a) Repeating polarization switching with T varied linearly with time between 8 K and 20 K. (b) T dependence of polarization around the T_L transition in different applied H (0.1, 0.5, and 3 T), indicating that T_L increases slightly with increasing H . (c) \mathbf{P} at 14.0 K vs H after poling the specimen in $H = 0.1$ T and $E \approx 10$ kV/cm. The initial $(+, +, +)$ state which is defined as $[\text{sgn}(\mathbf{M}), \text{sgn}(\mathbf{P}), \text{sgn}(\mathbf{Q})]$ changes to the $(+, -, +)$ state in $H \approx 3$ T. Negative H scan, reversing \mathbf{M} , induces switching of \mathbf{P} and \mathbf{Q} , i.e., resulting in the $(-, +, -)$ state.

cooling H , showing a slight increasing tendency of T_L with increasing H . At exactly 14.0 K, the phase cooled in 0.1 T is in the $(+, +, +)$ state, whereas cooling in 3 T puts the phase in the $(+, -, +)$ state. The black downward arrow denotes the possible switching of the physical state with increasing H at 14.0 K. As demonstrated in Fig. 4(c), the isothermal polarization reversal is, indeed, achieved by varying H at 14.0 K. After cooling down to 14.0 K in 0.1 T, the phase is initially in the $(+, +, +)$ state. The isothermal increase of H results in changing the state to $(+, -, +)$ by reversing \mathbf{P} , but keeping the direction of \mathbf{M} and \mathbf{Q} fixed. Because of the 1st order nature of the T_L transition, the $(+, -, +)$ state does not go back to the initial state of $(+, +, +)$ when H is reduced to zero (or the original 0.1 T). When the H direction is reversed, \mathbf{M} flips, so do \mathbf{P} and \mathbf{Q} , and thus the $(+, -, +)$ state becomes the $(-, +, -)$ state.

In summary, the conical-spiral ferroelectricity in CoCr_2O_4 can be described by the interrelationship among

ferroelectric polarization (\mathbf{P}), magnetization (\mathbf{M}), and spiral wave vector (\mathbf{Q}). Our results demonstrate that spontaneous electric polarization induced by the noncollinear spin order shows a discontinuous jump with a change in sign across the magnetic lock-in transition temperature ($T_L = 14$ K); furthermore the sign change occurs while keeping fixed the spin rotation direction, i.e., spiral handedness or $\text{sgn}(\mathbf{Q})$. This differs from the usual behavior wherein for a simple spiral, change in $\text{sgn}(\mathbf{P})$ requires the handedness to change sign, and we give a possible mechanism for such unusual behavior. We also recover the previous finding wherein $\mathbf{P} \rightarrow -\mathbf{P}$ when $\mathbf{M} \rightarrow -\mathbf{M}$ [8], but further show experimentally that this is accompanied by $\mathbf{Q} \rightarrow -\mathbf{Q}$, consistent with the Bloch wall mechanism [8] for switching \mathbf{M} . We further show that \mathbf{P} reverses its direction in ~ 3 T at exactly 14.0 K, due to a slight increasing trend of T_L with increasing H .

We thank S.D. Mahanti for his close following of this work and for many helpful discussions. Work at Rutgers is supported by NSF-DMR-0520471.

- [1] D.I. Khomskii, *J. Magn. Magn. Mater.* **306**, 1 (2006).
- [2] S.-W. Cheong and M. Mostovoy, *Nature Mater.* **6**, 13 (2007).
- [3] R.E. Newnham *et al.*, *J. Appl. Phys.* **49**, 6088 (1978).
- [4] N. Hur *et al.*, *Nature (London)* **429**, 392 (2004); *Phys. Rev. Lett.* **93**, 107207 (2004).
- [5] N. Menyuk *et al.*, *J. Phys. (Orsay, Fr.)* **25**, 528 (1964).
- [6] T. Kimura *et al.*, *Nature (London)* **426**, 55 (2003); *Phys. Rev. Lett.* **94**, 137201 (2005); *Phys. Rev. B* **73**, 220401(R) (2006).
- [7] G. Lawes *et al.*, *Phys. Rev. Lett.* **95**, 087205 (2005); *Phys. Rev. B* **74**, 024413 (2006).
- [8] Y. Yamasaki *et al.*, *Phys. Rev. Lett.* **96**, 207204 (2006).
- [9] K. Taniguchi *et al.*, *Phys. Rev. Lett.* **97**, 097203 (2006).
- [10] S. Park *et al.*, *Phys. Rev. Lett.* **98**, 057601 (2007).
- [11] D.H. Lyons *et al.*, *Phys. Rev.* **126**, 540 (1962).
- [12] A review: N. Menyuk, in *Modern Aspects of Solid State Chemistry*, edited by C.N.R. Rao (Plenum, New York, 1970), p. 1.
- [13] A review: T.A. Kaplan and N. Menyuk, *Philos. Mag.* **87**, No. 25, 3711 (2007); Corrigendum: **88**, No. 2, 279 (2008).
- [14] K. Tomiyasu *et al.*, *Phys. Rev. B* **70**, 214434 (2004).
- [15] H. Katsura *et al.*, *Phys. Rev. Lett.* **95**, 057205 (2005); C. Jia *et al.*, *Phys. Rev. B* **76**, 144424 (2007).
- [16] T.A. Kaplan and S.D. Mahanti, arXiv/cond-mat/0608227.
- [17] M. Mostovoy, *Phys. Rev. Lett.* **96**, 067601 (2006).
- [18] P. Peshev *et al.*, *Mater. Res. Bull.* **17**, 1413 (1982).
- [19] T.A. Kaplan (unpublished).
- [20] Y. Yamasaki *et al.*, *Phys. Rev. Lett.* **98**, 147204 (2007).
- [21] R. Plumier, *J. Appl. Phys.* **39**, 635 (1968).
- [22] M. Blume and D. Gibbs, *Phys. Rev. B* **37**, 1779 (1988); T.A. Kaplan (unpublished).
- [23] M. Blume, *Phys. Rev.* **130**, 1670 (1963).
- [24] T. Arima *et al.*, *J. Phys. Soc. Jpn.* **76**, 023602 (2007).

Appendix VIII.

down the chondrogenic pathway in response to the microenvironment modification (Fig. 3C and fig. S5). To examine cell interaction with this dynamic microenvironment, fixed sections were immunostained for the expression of the $\alpha_v\beta_3$ integrin, one of the cell surface integrins by which cells interact with RGDS. Cells persistently presented with RGDS express the integrin, whereas most cells with RGDS photoreleased cease integrin expression by day 21 (Fig. 4A), indicating that the cells have locally sensed and responded to the chemical change in their environment. Additionally, to determine that the elevated GAG production is associated with chondrogenesis, sections of the cell-hydrogel constructs were immunostained for the hMSC marker CD105 (transforming growth factor- β receptor) and the chondrocyte marker COLII. As hMSCs differentiate into chondrocytes in 3D culture, a decrease in CD105 expression is observed along with onset of COLII production (35). The photolytic removal of RGDS on day 10 is accompanied by a decrease in CD105 expression and elevated COLII production as compared with persistently presented RGDS on day 21 (Fig. 4B), indicating increased chondrogenesis. With this photodegradable tether approach, the dynamic influence of other biomolecules on cell function can be similarly studied, expanding the ability to fabricate material environments that control cell function. Although manipulation of a single signal was examined and used to direct hMSC differentiation herein, this gel system can be readily functionalized with photolabile moieties of different light absorbances and cleavage efficiencies, enabling independent control over multiple signals through selection of irradiation wavelength and intensity.

We have demonstrated the synthesis of photodegradable macromers and their subsequent polymerization to form hydrogels whose physical, chemical, and biological properties can be tuned in situ and in the presence of cells by ultraviolet, visible, or two-photon irradiation. These photo-

degradable hydrogels show promise as in vitro 3D cell culture platforms in which cell-material interactions are dynamically and externally directed to elucidate how cells receive and process information from their environments. Ways to promote or suppress desired cell functions may become possible with temporal and spatial regulation of the 3D culture microenvironment, leading to applications in fields ranging from controlled drug delivery to tissue regeneration.

References and Notes

- D. B. Weibel, W. R. Diluzio, G. M. Whitesides, *Nat. Rev. Microbiol.* **5**, 209 (2007).
- M. P. Lutolf, J. A. Hubbell, *Nat. Biotechnol.* **23**, 47 (2005).
- R. Langer, N. A. Peppas, *AIChE J.* **49**, 2990 (2003).
- M. M. Stevens, J. H. George, *Science* **310**, 1135 (2005).
- G. Chan, D. J. Mooney, *Trends Biotechnol.* **26**, 382 (2008).
- A. J. Engler, S. Sen, H. L. Sweeney, D. E. Discher, *Cell* **126**, 677 (2006).
- A. J. Engler et al., *J. Cell Biol.* **166**, 877 (2004).
- P. A. Kenny, M. J. Bissell, *Int. J. Cancer* **107**, 688 (2003).
- A. Metters, J. Hubbell, *Biomacromolecules* **6**, 290 (2005).
- M. A. Rice, J. Sanchez-Adams, K. S. Anseth, *Biomacromolecules* **7**, 1968 (2006).
- D. Seliktar, A. H. Zisch, M. P. Lutolf, J. L. Wrana, J. A. Hubbell, *J. Biomed. Mater. Res. Part A* **68A**, 704 (2004).
- M. Ehrbar et al., *Circ. Res.* **94**, 1124 (2004).
- G. A. Silva et al., *Science* **303**, 1352 (2004).
- A. Khademhosseini, R. Langer, *Biomaterials* **28**, 5087 (2007).
- R. W. Sands, D. J. Mooney, *Curr. Opin. Biotechnol.* **18**, 448 (2007).
- M. S. Hahn, J. S. Miller, J. L. West, *Adv. Mater.* **18**, 2679 (2006).
- J. H. Wosnick, M. S. Shoichet, *Chem. Mater.* **20**, 55 (2008).
- Y. R. Zhao et al., *J. Am. Chem. Soc.* **126**, 4653 (2004).
- M. Alvarez et al., *Adv. Mater.* **20**, 4563 (2008).
- Y. Luo, M. S. Shoichet, *Nat. Mater.* **3**, 249 (2004).
- S. A. Khan, I. M. Plitz, R. A. Frantz, *Rheol. Acta* **31**, 151 (1992).
- R. J. Young, P. A. Lovell, *Introduction to Polymers* (Chapman & Hall, London, ed. 2, 1991).
- S. J. Bryant, K. S. Anseth, in *Scaffolding in Tissue Engineering*, P. X. Ma, J. Elisseeff, Eds. (Marcel Dekker, New York, 2005), pp. 69–88.
- S. J. Bryant, C. R. Nuttallman, K. S. Anseth, *J. Biomater. Sci. Polym. Ed.* **11**, 439 (2000).
- P. Tayalia, C. R. Mendonca, T. Baldacchini, D. J. Mooney, E. Mazur, *Adv. Mater.* **20**, 4494 (2008).
- G. P. Raeber, M. P. Lutolf, J. A. Hubbell, *Biophys. J.* **89**, 1374 (2005).
- M. J. Mahoney, K. S. Anseth, *Biomaterials* **27**, 2265 (2006).
- E. Ruoslahti, M. D. Pierschbacher, *Science* **238**, 491 (1987).
- T. Boontheekul, D. J. Mooney, *Curr. Opin. Biotechnol.* **14**, 559 (2003).
- G. A. Hudalla, T. S. Eng, W. L. Murphy, *Biomacromolecules* **9**, 842 (2008).
- S. Tavella et al., *J. Cell Sci.* **110**, 2261 (1997).
- C. R. Nuttallman, M. C. Tripodi, K. S. Anseth, *Matrix Biol.* **24**, 208 (2005).
- C. N. Salinas, K. S. Anseth, *Biomaterials* **29**, 2370 (2008).
- A. M. DeLise, L. Fischer, R. S. Tuan, *Osteoarthritis Cartilage* **8**, 309 (2000).
- C. N. Salinas, B. B. Cole, A. M. Kasko, K. S. Anseth, *Tissue Eng.* **13**, 1025 (2007).
- The authors thank C. Bowman, T. Scott, and C. Kloxin for comments on early versions of this manuscript and valuable discussions; A. Aimeetti for peptide synthesis training; J. McCall and S. Anderson for cell culture assistance; M. Schwartz for cell migration discussions; C. Bowman and his laboratory for use of and assistance with the rheometer and profilometer; C. Kloxin for assistance with image analysis; C. DeForest, Carl Zeiss, Inc., and the Howard Hughes Medical Institute Janelia Farms campus for assistance with and use of the Zeiss 710 two-photon confocal LSM; and the Howard Hughes Medical Institute and the NIH (grants DE12998 and DE16523) for research support. A.K. thanks the NASA Graduate Student Researchers Program fellowship and the Department of Education Graduate Assistance in Areas of National Need fellowship for support. A patent related to this work has been submitted (U.S. Patent Application No. 11/374,471).

Supporting Online Material

www.sciencemag.org/cgi/content/full/324/5923/59/DC1

Materials and Methods

SOM Text

Figs. S1 to S5

References

8 December 2008; accepted 3 February 2009
10.1126/science.1169494

Switchable Ferroelectric Diode and Photovoltaic Effect in BiFeO₃

T. Choi, S. Lee,* Y. J. Choi, V. Kiryukhin, S.-W. Cheong†

Unidirectional electric current flow, such as that found in a diode, is essential for modern electronics. It usually occurs at asymmetric interfaces such as p-n junctions or metal/semiconductor interfaces with Schottky barriers. We report on a diode effect associated with the direction of bulk electric polarization in BiFeO₃: a ferroelectric with a small optical gap edge of ~2.2 electron volts. We found that bulk electric conduction in ferroelectric monodomain BiFeO₃ crystals is highly nonlinear and unidirectional. This diode effect switches its direction when the electric polarization is flipped by an external voltage. A substantial visible-light photovoltaic effect is observed in BiFeO₃ diode structures. These results should improve understanding of charge conduction mechanisms in leaky ferroelectrics and advance the design of switchable devices combining ferroelectric, electronic, and optical functionalities.

Ferroelectrics undergo a transition from a high-symmetry structure to a low-symmetry state with a spontaneous electric polariza-

tion below a transition temperature. They usually consist of a complex microstructure of domains with different orientations of the polarization that

can be switched with external electric fields (1). Ferroelectrics are typically highly insulating because of large band gaps (2), and any current leakage has been considered to be a serious problem that deteriorates their functionalities (3, 4). The relationship between electronic transport characteristics and ferroelectric polarization has been little studied. This is partially due to complexity associated with ferroelectric domains. In addition, leakage often occurs through extended crystallographic defects such as grain boundaries or ferroelectric domain boundaries, so the true bulk leakage conduction may not be always dominant.

Rutgers Center for Emergent Materials and Department of Physics and Astronomy, Rutgers University, Piscataway, NJ 08854, USA.

*Present address: Neutron Science Division, Korea Atomic Energy Research Institute, Daejeon 305-353, Korea.

†To whom correspondence should be addressed. E-mail: sangc@physics.rutgers.edu

REPORTS

On the other hand, bulk photocurrent can be induced by high-energy light illumination even in good insulators; and directional photocurrent without external bias [that is, a photovoltaic (PV) effect] has been studied in ferroelectrics (5–13). When a ferroelectric in an open circuit is illuminated by ultraviolet light, for example, a high photovoltage, much larger than the band gap, has been observed in the direction of the electric polarization (5–8). The magnitude of this photovoltage is directly proportional to the crystal length in the polarization direction. In addition, a steady-state photocurrent can be generated in the direction of electric polarization when a ferroelectric under continuous light illumination forms a closed circuit. This PV effect in ferroelectrics is distinctly different from the typical PV effect in semiconductor p-n junctions, and was investigated in Pb-based ferroelectric oxides (9–11) and LiNbO₃ (6, 8). However, the observed photocurrent density turns out to be minuscule—on the order of a few nanoamperes/cm², mainly due to poor bulk dc conduction of the ferroelectrics (8, 9, 11). Utilization of small-optical-gap ferroelectrics with good carrier transport properties and large absorption of visible light extending into the red range is therefore a promising route toward novel optoelectronic applications. It may, for example, lead to increased power conversion efficiency in solar energy applications. The origin of the PV effect in ferroelectrics is controversial and has been discussed in terms of extrinsic effects such as the excitation of electrons from asymmetric impurity potentials (12), interfacial effects due to polarization-dependent band bending at metal-ferroelectric interfaces (9), or intrinsic effects such as asymmetric induced polarization through nonlinear optical processes (13–15).

Ferroelectric BiFeO₃ (BFO) contains transition metal ions with unpaired *d* electrons. The presence of the *d* electrons can result in a relatively small optical gap and give rise to a high concentration of charged impurities and defects (16). BFO becomes ferroelectric at a critical temperature (T_c) \approx 1100 K, below which BFO exhibits a rhombohedral *R3c* structure with a perovskite pseudocubic unit cell ($a \approx 3.96$ Å, $\alpha \approx 89.4^\circ$) elongated along the [111] direction that coincides with the electric polarization vector *P*. Each of our BFO crystals contained a single ferroelectric domain (17, 18). Here we describe the electronic transport properties of three thin platelike BFO crystals placed between symmetric electrodes: BFO1 (~ 70 μm thickness, $\sim 2 \times 2$ mm² in-plane dimension, and ~ 0.6 -mm-diameter circular thick Au electrodes), BFO2 (~ 80 μm thickness, $\sim 2.5 \times 2.5$ mm² in-plane dimension, and $\sim 1.6 \times 1$ mm² semitransparent Au electrodes), and BFO3 (~ 90 μm thickness, $\sim 1 \times 2$ mm² in-plane dimension, and ~ 0.6 -mm-diameter circular thick Ag or Au electrodes). The BFO plates are normal to a principal axis of the pseudocubic cell, and the “in-plane or out-of-plane” component of the polarization is defined with respect to the plate surface.

We found that in all investigated specimens, there existed substantial currents that were nonlinear with applied electric field *E* and also depended strongly on the direction of *E*. The magnitude of *E* here is much less than ferroelectric coercivity (fig. S1), so polarization switching does not occur during the *E* sweep for current density, *J*, versus *E* curves. Figure 1A shows linear-scale *J(E)* curves of BFO1 at 300 and 350 K, which exhibit diodelike behavior. For the typical p-n junction diodes, the forward current density follows an exponential relationship with applied voltage given by $J \propto \exp(qV/(\alpha k_B T))$, where *q* is the electron charge, *V* is voltage, α is a constant called the ideality factor, and k_B is the Boltzmann constant. In the range of 0.05 to 0.15 kV/cm forward bias, α is 6.3 at 300 K and 4.7 at 350 K. This large ideality factor, much larger than the ideal value of 1 in semiconductor p-n junctions, has been observed in perovskite-based oxide p-n junctions, where charge trapping at defects in the bulk seems important for transport properties (19). We also found that *J* increases drastically with increasing temperature from 200 to 350 K as evident in the semi-log plot of *J(E)* curves in the inset of Fig. 1A. In addition, the asymmetry in the *J(E)* curve also increases with increasing *T*. The rectification ratios, defined as the ratios of the positive current divided by the negative one for $E = \pm 1.3$ kV/cm, at

200, 250, 300, and 350 K, are 13, 159, 488, and 495, respectively.

The diode forward and reverse directions switch when ferroelectric polarization is uniformly reversed by large electric voltage pulses. When +150-V (an *E* of +17 kV/cm) pulses are applied to the top electrode of BFO3 shown in Fig. 2A, the ferroelectric polarization points down, as confirmed by piezoresponse force microscopy (PFM; see supporting online materials and methods) (Fig. 2B). The electric current through the specimen is large when the current direction is also downward; that is, the diode forward direction is from top to bottom, and along the polarization direction (Fig. 2C). When –150-V pulses are applied, ferroelectric polarization switches to the upward direction, and the diode forward direction becomes from bottom to top (still along the polarization direction). Application of +150-V pulses restores the original configuration. Therefore, the diode directions switch whenever ferroelectric polarization is reversed by external pulses, and the diode forward direction is always along the ferroelectric polarization direction (Fig. 2C). The application of the second set of +150-V pulses does not completely restore the original *J(E)* curve, and this incomplete restoration may be due to complex factors such as incomplete polarization flipping, the formation of conducting paths, or irreversible changes in the interfacial

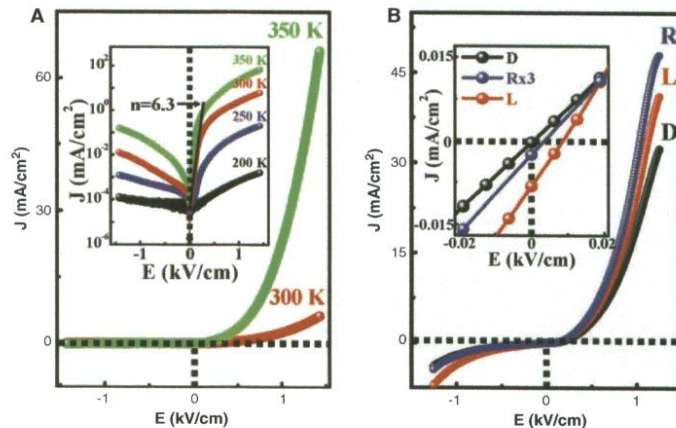


Fig. 1. (A) *J(E)* curve of a symmetric Au/BFO1/Au structure in the dark at 300 and 350 K. A substantial diodelike effect is evident. The inset shows semi-log-scale *J(E)* curves at various temperatures. All *J(E)* measurements were performed by sweeping the voltage from the positive maximum to the negative maximum in vacuum at 200 to 350 K. The applied electric fields are far below the coercive field for polarization switching. (B) *J(E)* curves of the BFO2 sample in the dark (D) and with green-light illumination on right (R) or left (L) semitransparent Au electrodes. Current for either *E* direction (except very near *E* = 0) increases with illumination on either side. The inset shows an expanded view of the *J(E)* curves near zero bias field (*E* = 0). Zero-bias current flows along the reverse direction with illumination from either direction: Left-side illumination works better than right-side illumination for this particular setup, and the *x* and *y* axes for the right-side illumination are expanded by a factor of 3 to clearly show the presence of the reverse-direction current at zero bias.

regions. In the above discussion, we consider only the out-of-plane component of ferroelectric polarization because of the platelike geometry of the Ag/BFO3/Ag structure. We emphasize that even though the simultaneous $J(E)$ and PFM experiments with electric pulses were performed only on BFO3, the switchable $J(E)$ curves were observed in all specimens that we have investigated.

The observed diodelike behavior of dc conduction implies a possibility of zero-bias PV effect in BFO. Because the optical gap edge of BFO is reported to be ~ 2.2 eV (20), visible light is expected to induce substantial photocurrent. We, in fact, found a substantial PV effect in BFO with semitransparent Au electrodes illuminated with visible light [wavelength (λ) = 532-nm green light and λ = 630-nm red light], with the total power density being less than 20 mW/cm².

Figure 1B depicts the $J(E)$ curves of BFO2 with symmetric Au electrodes in green light as well as in the dark. Green light illuminated either left or right semitransparent Au electrodes of BFO2 (see the experimental schematic in the inset of Fig. 3). Illumination on either side induces the increase of conductance with the direction of photocurrent after the direction of the external bias. In other words, measurable photoconduction occurs with illumination. At zero bias, the photocurrent also exists and is always nega-

tive, independent from the illumination direction: negative 0.13 μ A, corresponding to reverse bias direction 8.219 μ A/cm² for the BFO2 configuration with left-side illumination; and 0.013 μ A, corresponding to reverse bias direction 0.849 μ A/cm² for the configuration with right-side illumination (Fig. 1B, inset). This bulk photocurrent in the absence of an external bias indicates that charge carriers induced by light illumination move preferentially along one direction; that is, there is a PV effect in BFO2. Figure 3 shows the time dependence of the photocurrent at zero bias in BFO2 with the turning of a green (top panel) and a red (bottom panel) light on and off. For the first 60 min, the left electrode was illuminated and for the next 60 min the right electrode was illuminated. Photoconductivity was reported in ferroelectric monodomain (111) BFO films, but any PV effect (nonzero photoconductivity at zero bias) was not discussed in the report (27).

In principle, thermal variation induced by visible-light illumination can contribute to the photocurrent increase shown in Fig. 1B, but the decrease of resistance due to a light-induced temperature increase cannot cause the observed negative steady photocurrent at zero bias. On the other hand, a pyroelectric current can be generated by the change of the magnitude of ferroelectric polarization because of the temperature increase caused by light illumination. However,

this is a transient effect that occurs while the temperature is changing, and no steady-state photocurrent is expected from the pyroelectric effect. Thus, although the initial small spikes of photocurrent in Fig. 3 can be attributed to the pyroelectric effect, the steady-state photocurrent in Fig. 3 has a different origin. Consistently, when the light is switched on, the photocurrent increases suddenly to a transient maximum before reaching a steady state. The transient component with green light is $\sim 6\%$ of the steady-state photocurrent, and the time constant associated with the transient component is ~ 15 s. The transient component with red light is $\sim 25\%$ of the steady-state photocurrent and the time constant is ~ 60 s. The steady-state photocurrent density is ~ 7.35 μ A/cm² under green light illumination on the left side. This value is much larger than the 2.6 nA/cm² observed under red light illumination, indicating that the photoexcited charge carriers across the bulk optical gap of ~ 2.5 eV contribute to the PV effect in BFO. Finally, because our BFO crystals are conducting, an equilibrium temperature gradient generated by continuous light illumination on one side of BFO can produce a steady current due to thermoelectric power voltage. However, this effect should produce an opposite-direction current when the light-illumination direction is changed from one side to the other of the BFO crystal. Our zero-bias photocurrent direction is always fixed, independent of the light-illumination conditions, which is inconsistent with the thermoelectric power scenario. On the other hand, the thermoelectric power effect may contribute to the asymmetry in the magnitude of the photocurrent with different-side light illumination, which turns out to be substantial in BFO2. Obviously, any uncontrolled asymmetry in the electrode configuration or light-illumination conditions can also contribute to the left-right asymmetry in the magnitude of the photocurrent.

A linear polarizer was placed between the light source and BFO2 to measure the effect of light polarization on the PV effect (Fig. 4, inset). The angle θ between the in-plane component of ferroelectric polarization (determined by in-plane PFM) and the electric field vector of linearly polarized light was varied by 360°. The change of the photocurrent at zero bias with θ , shown in Fig. 4 with blue circles, closely follows a sinusoidal form with a periodicity of 180°. The maximum of photocurrent was observed when the polarized-light electric field was along the in-plane ferroelectric polarization, and the current was minimal when the light electric field was perpendicular to the in-plane ferroelectric polarization. After the initial rotation experiment, the polarizer was rotated by 90°, and lighting conditions were readjusted for an optimum photocurrent. The change of photocurrent (green circles) with θ after this polarizer rotation is similar to the one before rotating the polarizer, except for a 90° phase shift of θ . This demonstrates that the reproducible angular dependence is not due to any artifact of our optical setup.

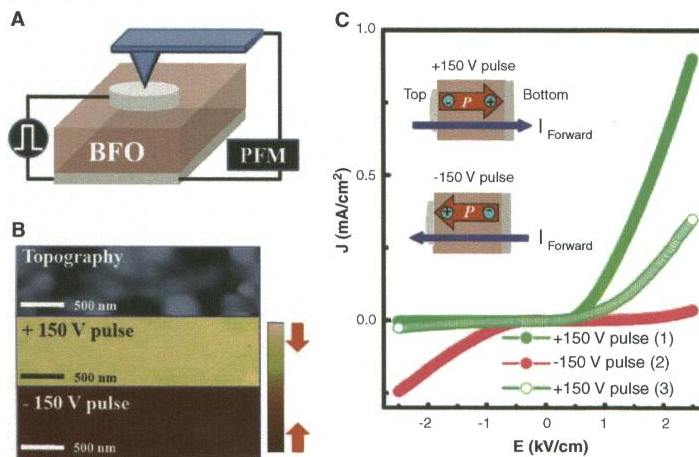


Fig. 2. (A) Sketch of the setup for the simultaneous PFM and $J(E)$ measurements on Ag/BFO3/Ag. One hundred electric pulses with ± 150 V ($E = 17$ kV/cm) and a duration of 0.01 s were used to flip electric polarization. $J(E)$ was measured up to $E = 2.5$ kV/cm, and ac voltage of 1 V_{rms} and 17 kHz was used for PFM. (B) Topography image and out-of-plane PFM images after ± 150 -V pulses. The PFM signal is color-scaled. These images show that +150-V pulses induce a homogeneous state with downward out-of-plane polarization, and -150-V pulses induce a homogeneous state with upward polarization. (C) $J(E)$ curves of BFO3 after +150-V, -150-V, and +150-V pulses, in sequence. The diode forward and reverse directions switch when the direction of out-of-plane polarization (P) is reversed by ± 150 -V pulses. The diode forward direction turns out to be the same as the direction of electric pulses used for polarization flipping.

REPORTS

The above observations shed light on the origin of the PV effect in BFO. The sinusoidal behavior of the photocurrent at zero bias observed in the polarized-light rotation experiment is consistent with a nonlinear optical effect scenario (13). When a ferroelectric is under intense light illumination, the second-order optical response combined with a linear term is well known to induce an asymmetric polarization, which can result in an optical rectification effect (14, 15). It was proposed that the asymmetric induced polarization can also give rise to a dc rectification-like effect such as a PV effect. This effect is supposed to be maximal when the polarized-light electric field is along the ferroelectric polarization and follows a sinusoidal angular dependence. This second-order optical response is an intrinsic bulk effect, and therefore it should not be sample-dependent. However, we found a noticeable variation in the magnitude of the rectification

and PV effects in different samples, suggesting the importance of impurities and defects with respect to the transport mechanism. The space charge-limited conduction suggested in the diode behavior (figs. S2 and S3) is also consistent with the importance of impurities and defects. Any polarization-related asymmetry of impurity potentials can render the photocurrent sensitive to the orientation of light polarization, probably in a sinusoidal manner (12). Simple polarization-dependent band-bending at the metal/BFO interfaces probably does not produce the observed directional dependence. In addition, we found little difference between the effects of Ag and Au electrodes on the diode effect (fig. S4), suggesting no major contribution from the band-bending at the metal/BFO interfaces. On the other hand, the contribution of impurities and defects coupled with the band-bending or the second-order optical response to

photocurrent can be influenced by the orientation of polarization.

We report here that single-ferroelectric-domain BFO crystals exhibit a diodelike effect. The forward direction of the diode is determined by the direction of the electric polarization, and the directionality of the diode can be reproducibly switched by large external electric fields. Associated with the diode effect, a substantial zero-bias PV current is induced by visible light. Further study of these effects, such as experiments involving electrodes with different conductors or controlled doping levels and spectroscopic studies of metal/BFO interfaces, will be necessary to unveil their true origin. The observation of switchable diode and photovoltaic effects in BFO reveals unusual and intriguing charge conduction behavior in leaky ferroelectrics, and should advance studies of BFO-based multifunctional devices.

Fig. 3. The zero-bias photocurrent density as a function of time with (top) green light ($\lambda = 532$ nm) or (bottom) red light ($\lambda = 650$ nm) on or off, shining on the different sides of BFO2 (a sketch is shown in the inset). The total light power was <3 mW, and the short-circuit photocurrent was measured every 100 ms. The current with the light off decreased to <0.1 pA. Illumination from either side results in the same-direction zero-bias photocurrent, unambiguously demonstrating the PV effect in ferroelectric BFO. The large difference in the magnitude of photocurrent between green- and red-light illumination indicates that photoexcited carriers across the bulk optical gap (~ 2.5 eV) dominate the PV effect. The observed right-left asymmetry may result from a thermoelectric power effect and/or uncontrolled asymmetries in the experimental configuration.

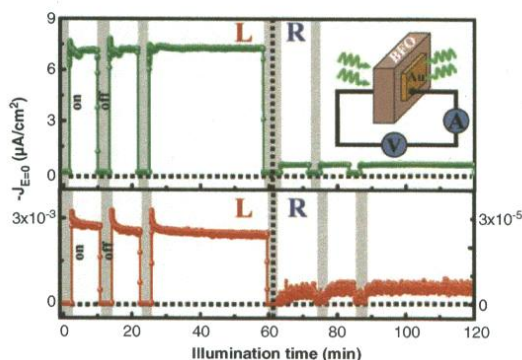
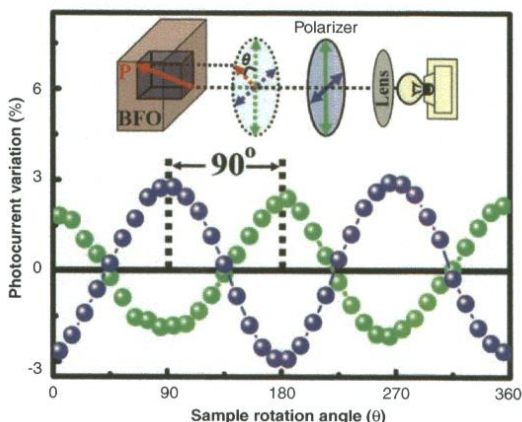


Fig. 4. The variation of photocurrent with sample rotation under illumination with a linearly polarized light. The experimental sketch is shown in the inset. The PV effect becomes maximum when the polarized-light electric field is parallel to the in-plane component of the ferroelectric polarization, and minimum when the field is perpendicular to the in-plane component.



References and Notes

1. J. F. Scott, *Ferroelectric Memories* (Springer, Heidelberg, Germany, 2000).
2. M. Dawber, K. M. Rabe, J. F. Scott, *Rev. Mod. Phys.* **77**, 1083 (2005).
3. J. F. Scott, *J. Phys. Condens. Matter* **20**, 021001 (2008).
4. J. Wang et al., *Science* **299**, 1719 (2003).
5. V. M. Fridkin, B. N. Popov, *Sov. Phys. Usp.* **21**, 981 (1978).
6. A. M. Glass, D. Von der Linde, T. J. Negran, *Appl. Phys. Lett.* **25**, 233 (1974).
7. N. Noginova et al., *J. Opt. Soc. Am. B* **14**, 1390 (1997).
8. G. Dalba, V. Soldo, F. Rocca, V. M. Fridkin, Ph. Saintavit, *Phys. Rev. Lett.* **74**, 988 (1995).
9. Y. S. Yang et al., *Appl. Phys. Lett.* **76**, 774 (2000).
10. P. Poosanaas, A. Dogan, S. Thakoor, K. Uchino, *J. Appl. Phys.* **84**, 1508 (1998).
11. L. Pintilie, I. Vrejoiu, G. L. Rhun, M. Alexe, *J. Appl. Phys.* **101**, 064109 (2007).
12. V. I. Belinicher, B. I. Sturman, *Sov. Phys. Usp.* **23**, 199 (1980).
13. K. Tonooka, P. Poosanaas, K. Uchino, *Proc. SPIE* **3324**, 224 (1998).
14. M. Bass, P. A. Franken, J. F. Ward, G. Weinreich, *Phys. Rev. Lett.* **9**, 446 (1962).
15. A. Rice et al., *Appl. Phys. Lett.* **64**, 1324 (1994).
16. A. J. Hauser et al., *Appl. Phys. Lett.* **92**, 222901 (2008).
17. S. Lee, W. Ratcliff II, S.-W. Cheong, V. Kiryukhin, *Appl. Phys. Lett.* **92**, 192906 (2008).
18. S. Lee et al., *Phys. Rev. B* **78**, 100101 (2008).
19. Y. W. Xie et al., *J. Phys. Condens. Matter* **19**, 196223 (2007).
20. F. Gao et al., *Appl. Phys. Lett.* **89**, 102506 (2006).
21. S. R. Basu et al., *Appl. Phys. Lett.* **92**, 091905 (2008).
22. This work was funded by NSF (grants NSF-DMR-0804109 and 0704487). T.C. was partially supported by a Korea Research Foundation Grant funded by the Korean government (MOEHRD, grant KRF-2007-357-C00023).

Supporting Online Material

www.sciencemag.org/cgi/content/full/1168636/DC1
Materials and Methods
Figs. S1 to S4
References

17 November 2008; accepted 3 February 2009
Published online 19 February 2009;
10.1126/science.1168636
Include this information when citing this paper.

Appendix IX.

Giant Magnetic Coercivity and Ionic Superlattice Nano-domains in $\text{Fe}_{0.25}\text{TaS}_2$

Y. J. Choi¹, S. B. Kim², T. Asada³, S. Park¹, Weida Wu¹, Y. Horibe¹, and S-W. Cheong^{1,2}

¹*Rutgers Center for Emergent Materials and Department of Physics & Astronomy, 136 Frelinghuysen Road, Piscataway, New Jersey, 08854, USA*

²*Laboratory of Pohang Emergent Materials and Department of Physics, Pohang University of Science and Technology, Pohang 790-784, Korea*

³*Research Department, NISSAN ARC, LTD., Yokosuka, Kanagawa 237-0061, Japan*

PACS 75.50. Vv – High coercivity materials

PACS 75.50 Ww – Permanent magnets

PACS 75.30 Gw – Magnetic anisotropy

Abstract – We have explored giant magnetic coercivity ($H_c \approx 7$ tesla) in the highly anisotropic ferromagnet of $\text{Fe}_{0.25}\text{TaS}_2$ through harnessing order of Fe^{2+} ions intercalated in-between TaS_2 layers. Fe ions order well in annealed crystals and form a $(1/2, 0, 0)$ superlattice. However, a $(1/3, 1/3, 0)$ superlattice, in addition to the $(1/2, 0, 0)$ superlattice, can form in quenched crystals. These coexisting superlattices with nano-size domains result in significant change of magnetic domain configurations and huge enhancement of

H_c , probably through efficient magnetic domain wall pinning by nano-size superlattice domains.

Introduction. – The rapid advancement of material science, especially with permanent magnets, is being integrated in a wide spectrum of modern technological applications, including high-efficiency motors and generators, as well as high-density magnetic memory devices. The continuous discovery of new materials and innovative mechanisms for enhanced properties, such as magnetic coercivity (H_c), is crucial for depinning new technologies. The H_c is defined as the external magnetic field value to reduce the magnetization of a fully magnetized material to zero [1]. It is determined by magnetocrystalline anisotropy and the energetics of magnetic domain (MD) nucleation and growth [2]. The former is controlled by the spin-orbit coupling - a relativistic effect which is large in heavy elements [3]. Crystallographic defects can impede the growth and propagation of MD walls, and thus enhance the H_c [4]. Consistently, high coercivity is often found in polycrystalline materials which have a significant amount of defects and grain boundaries. Increase of MD wall pinning has been achieved by a wide range of approaches, such as adding chemical impurities [2], creating lattice defects by various heat treatments [5], and controlling nanoscale structures of mixed materials with matching magnetic properties [6]. Herein, we present a unique method of enhancing H_c in single-crystalline $\text{Fe}_{0.25}\text{TaS}_2$ by controlling ionic order.

Fe_xTaS_2 crystallizes in an Fe-intercalated 2H-TaS₂-type hexagonal structure [7,8]. In each TaS₂ layer in the structure, Ta ions are coordinated by trigonal-prismatic S²⁻ cages. It has

been reported that Fe ions intercalated into between TaS₂ layers can order, and form ionic superlattices. Superlattice for $x \approx 0.25$ has the periodicity of $2 a_0$ (i.e., (1/2,0,0)-type) where a_0 is the in-plane lattice constant of the hexagonal TaS₂, while $\sqrt{3} a_0$ (i.e., (1/3,1/3,0)-type) becomes the periodicity of the superlattice for $x \approx 0.33$ [9,10]. Fe_{0.25}TaS₂ and Fe_{0.33}TaS₂ are ferromagnetic below ~ 160 K and ~ 35 K [11], respectively, but the H_c of $x \approx 0.25$ is found to be significantly larger than that of $x \approx 0.33$ [7].

Experimental. – Single crystals of Fe_{0.25}TaS₂ were grown by a chemical vapor transport method [7,11]. Thin plate-like crystals with large hexagonal surfaces perpendicular to the c axis were obtained. Three types of specimens were prepared; as-grown (AG, cooled in a furnace after its power was turned off after growth), slowly-cooled (SC, cooled with the cooling rate of 2 °C/hr from 700 °C) and quenched (Q, quickly removed from 700 °C and then soaked in ice water). Magnetic measurements were performed with the Quantum Design MPMS (magnetic field, $H \leq 7$ T) and PPMS ($H \leq 9$ T). TEM (Transmission Electron Microscopy) observations were carried out at room temperature with a JEOL-2000FX TEM, and electron diffraction (ED) patterns and dark-field (DF) images were recorded on imaging plates. MFM (Magnetic Force Microscopy) experiments were performed with a homemade variable temperature MFM interfaced with a Nanoscope IIIa controller from the Veeco Digital Instruments. The MFM images were taken in a frequency-modulated lift mode, in which the topography and MFM scan lines are interleaved. The lift height was regulated from 15 to 35 nm.

Results and discussion. – The temperature dependent magnetization, M/H , of the three types of specimens, shown in Fig. 1(a), was measured along the c -axis upon warming in $H=0.2$ T after field cooling (FC, open circles) and zero-field cooling (ZFC, solid lines). Ferromagnetic order for the SC and AG sets in at similar temperatures - $T_c=159$ and 156 K, respectively, while T_c of the Q is a much lower temperature (104 K). The temperatures at which the FC and ZFC $M(T)$ curves start to split were observed, indicative of the onset of magnetic irreversibility [12]. Below these temperatures, ZFC $M(T)$ curves drop precipitously and merge together at low temperatures whereas FC curves maintain their flatness in logarithmic scale. $M(H)$ hysteresis curves at 2 K for the three-types of specimens are shown in Fig 1(b). The saturation moment, depending little on the type of specimen, is $\sim 4 \mu_B$, which is consistent with the full saturation of the high-spin Fe^{2+} moment. The extremely sharp jumps in the hysteresis curves indicate the flipping of a nearly single MD through an avalanche-like magnetization reversal process with the variation of H [13,14]. The magnetic field where the jump occurs can be defined as the coercivity field, H_c , and this H_c is unusually large in all three types of specimens, even though the specimens are in the form of single crystals. This large H_c is certainly related with large magnetic anisotropy, which is reflected in the anisotropic $M(H)$ curves of the SC with H along and perpendicular to the c axis (Fig. 1(b)). The estimated anisotropy field is ~ 59 T, consistent with a recent report [15]. In any case, the intriguing characteristic of the $M(H)$ curves is the significant increase of H_c , with the increasing cooling rate from 700°C : H_c for the Q is ~ 7 T, while H_c 's of the SC and AG are ~ 2.7 and ~ 4.0 T, respectively.

In order to reveal the origin of the large change of H_c with varying thermal treatment, we have carefully investigated the structural evolution with thermal annealing by using the TEM. Indeed, we found interesting variations of the nature of Fe-ionic order in $\text{Fe}_{0.25}\text{TaS}_2$ with different cooling rate. Figures 2 (a) and (b) show the [011] ED pattern of the Q and the [001] ED pattern of the SC, respectively, and their intensity profiles in $\text{Fe}_{0.25}\text{TaS}_2$ (Fig. 2 (a') and (b')). Note that the ED pattern of the AG is basically identical to that of the SC, and the reflection spots are indexed using a simple hexagonal notation. Clear $(1/2,0,0)$ superlattice spots, in addition to the fundamental spots of the hexagonal structure, in the SC (and AG) are indicative of the formation of a 2×2 superlattice due to order of Fe ions between TaS_2 layers, consistent with the results in the previous work [11]. However, the Q exhibits a honeycomb ED pattern with weak diffusive spots (DS) at $(1/3,1/3,0)$ -type positions (arrow A) as well as DS at $(1/2,0,0)$ -type positions (arrow B). Thus, $\sqrt{3} \times \sqrt{3}$ and 2×2 superlattices coexist in the Q [9,10]. Figure 2(c) shows the schematics of the 2×2 and $\sqrt{3} \times \sqrt{3}$ superlattices in a single Fe layer. The large (small) circles and solid (dashed) lines denote the 2×2 ($\sqrt{3} \times \sqrt{3}$) superlattice, and the hatched region represents the unit cell of the simple hexagonal structure. The 2×2 and $\sqrt{3} \times \sqrt{3}$ superlattices correspond to the 25% and 33.3% concentrations of Fe ions per chemical formula, respectively. Thus, the long-range ordered $(1/2,0,0)$ superlattice spots indicate that the stoichiometry of the SC and AG is equal to $x \approx 0.25$, consistent with the magnitude of measured saturation magnetic moment. Furthermore, it is expected that the Q consists of inhomogeneous Fe-ionic distribution and likely contains Fe vacancies in the $\sqrt{3} \times \sqrt{3}$ superlattice. Note that regardless of the inhomogeneous Fe order and the decrease of T_c in the Q (Fig. 1(a)), the saturated magnetic

moment in high fields remains intact in the Q, indicating that the stoichiometry of the Q is still $x \approx 0.25$.

Upon changing the sample cooling rate from 700 °C, the superlattice domain structure as well as MD structure of $\text{Fe}_{0.25}\text{TaS}_2$ evolves in a remarkable manner. Our TEM DF images taken at room temperature and MFM images obtained at low temperatures after ZFC are summarized in Fig. 3. Fig. 3 (a) displays a DF image obtained by using a $(1/3, 1/3, 0)$ -type superlattice DS of the Q. The bright speckled regions with the typical size of ~ 2 nm are clearly visible in the figure, and the regions indicate the existence of ~ 2 nm-size superlattice domains with $\sqrt{3} \times \sqrt{3}$ -type Fe order. Our DF images taken by using $(1/2, 0, 0)$ -type DS also show similar speckled regions, suggesting that the domains with 2×2 -type order are comparable with the $\sqrt{3} \times \sqrt{3}$ -type domains in size. Figs. 3 (b) and (c) exhibit the DF images obtained by using $(1/2, 0, 0)$ -type superlattice spots in the AG and SC, respectively. The grainy patterns of the figures are due to the presence of anti-phase domains, and indicate that as the sample cooling rate decreases, the density of the anti-phase boundaries is reduced and the size of anti-phase domains becomes large. The average sizes of structural domains estimated from the TEM DF images of the Q, AG and SC (Fig. 3 (a)-(c)) are approximately 2, 30, and 100 nm, respectively. Similarly to the structural domains, the MD pattern also changes remarkably with the sample cooling rate (Fig. 3 (d)-(f)). The estimated widths of MDs are about 0.1 μm (Q), 0.2 μm (AG) and 1 μm (SC). Note that in each specimen, there exists little temperature dependence of the ZFC MD pattern below T_c . The systematic evolution of the ionic superlattice domains with varying the sample cooling rate suggests that the superlattice domains, existing at all

temperatures below room temperatures, affect strongly the morphology of ferromagnetic domains below T_c . Naturally, the superlattice domains or their boundaries can act as defects for nucleation and also pinning of MDs and boundaries [16,17].

Detailed magnetic properties associated with the large coercivity in the Q were investigated. The temperature variation of H_c of the Q can be estimated from magnetic hysteresis loops in Fig. 4(a), which were obtained after FC in 9 T (for the 2 K loop) or 7 T (for the other loops). The fully saturated magnetization ($M_s \approx 4 \mu_B/\text{Fe}$) in 9 T at 2 K varies little with decreasing H until the magnetization switches suddenly from M_s to $-M_s$ at around -7 T within a narrow H range (<0.01 T). This sharp switch from M_s to $-M_s$ broadens slowly, and the H_c decreases as the temperature is increased. H_c vs. $(T/T_c)^{1/2}$ for the Q (closed circles) is plotted in the inset of Fig. 4(b). Note that the negligible H -dependence of magnetization until H approaches close to the negative H_c remains intact at high temperatures. The H_c of the Q (7 T) at 2 K significantly exceeds that of the SC (2.7 T) (Fig. 1(b)), probably because superlattice nano-domains and domain boundaries in the Q provide efficient pinning centers of MD walls [18]. The T -dependent H_c for ferromagnets with high uniaxial anisotropy follows an empirical formula: $H_c(T)/H_c(0) = -V_T T + [1 + (V_T T)^2]^{1/2}$, where V_T is a parameter indicating the degree of easiness for thermally activated depinning of domain walls [19-21]. The fitting curve with the above function for the Q is in good accord with the experimental data in a wide T range, shown in the inset of Fig. 4(b), indicating that thermal activation over the energy barrier associated with domain wall pinning dominates the T dependence of H_c . The fitted V_T value for the Q is $\sim 0.25 \text{ K}^{-1}$, and is much larger than typical values of highly-anisotropic

magnets with highly-defective morphology, suggesting that the individual magnetic pinning strength of a superlattice nano-domain or domain boundary is relatively weak [19,20]. However, a high density of pinning centers, which is inversely proportional to the superlattice nano-domain volume, can result in considerable pinning strength of a MD wall through multiple/collective pinning. In a simple model, the average pinning potential E_p of pinning centers can be estimated to be $E_p \approx k_B \ln \frac{\nu_0}{\nu} / V_T \approx 10^{-21} \text{ J}$, where $\nu_0 \approx 10^{10} \text{ Hz}$ is the typical domain wall eigenfrequency and $\nu \approx 0.1 \text{ Hz}$ is the measurement frequency [20]. With the superlattice domain size of $\xi \approx 10^{-9} \text{ m}$, the density of pinning centers is $\rho_p \approx 1/\xi^3 \approx 10^{27} \text{ m}^{-3}$, and thus the zero-temperature coercivity is $H_c(0) \approx \rho_p E_p / 2M_s \approx 5 \text{ T}$ with the saturated magnetization of $M_s \approx 10^5 \text{ A/m}$ by simply equating the pinning energy density to the Zeeman energy density. The estimated zero-temperature coercivity is comparable with the observed value of 7 T, qualitatively supporting the scenario of superlattice nano-domains as dominant pinning centers for MD walls.

The T -dependent magnetization of the Q in various magnetic fields ($H^*=0.02, 0.2, 2$ and 7 T) applied after ZFC, is shown in Fig. 4(b). Magnetization in 7 T is tiny in magnitude at 2 K, indicating an almost fully demagnetized state even in 7 T. However, it increases drastically above 2 K, reaches the maximum value at $\sim 5 \text{ K}$ (corresponding to the fully saturated moment), and then decreases slowly with further increase of T . This sharp feature at 2-5 K in 7 T, comparable to the sharp change found in $M(H)$, shifts to a high T and becomes broad when H is reduced. For each H^* , T^* is defined as the temperature for the

maximum slope of the $M(T)$ curve in the H^* , and the T^* vs. H^* plot is shown in the inset of Fig. 4(b) (open squares). This plot coincides more-or-less with the T -dependent H_c (closed circles), but for each temperature, H^* tends to be slightly smaller than H_c . Since H^* corresponds to T -induced switching from a demagnetized state to a fully-saturated state while H_c represents H -induced switching from one fully-saturated state to the other-direction fully-saturated state, H^* is naturally smaller than H_c . However, their temperature dependences, as well as their sharp features, are similar, suggesting that a similar avalanche-like depinning of MD walls is responsible for the both phenomena.

Conclusion. – In summary, we have discovered an intriguing interplay between ionic order and magnetism in $\text{Fe}_{0.25}\text{TaS}_2$ crystals with high magnetic anisotropy. A long-range ionic order with a 2×2 superlattice occurs in well-annealed specimens, but in quenched specimen, nano-size domains with a $\sqrt{3} \times \sqrt{3}$ -type ionic order mix with 2×2 superlattice nano-domains. We found a systematic change of H_c in thermally-treated crystals of $\text{Fe}_{0.25}\text{TaS}_2$, which is accompanied by significant changes of the pattern and size of MDs. Nano-scale mixture of 2×2 and $\sqrt{3} \times \sqrt{3}$ superlattice domains is responsible for the large coercivity of ~ 7 T in the quenched specimen, which is attributed to the efficient pinning of MD walls by the mixed nano-size superlattice domains.

We acknowledge B. I. Min for the suggestion of the system and Ryan Mich for reading manuscript. Work at Rutgers was supported by NSF-DMR-0804109.

Figure Captions

Fig. 1: (Colour on-line) (a) Temperature dependence of magnetization divided by magnetic field, M/H , in logarithmic scale for the SC (slowly-cooled), AG (as-grown), and Q (quenched) crystals, measured upon warming ($H=0.2$ T// c) after cooling in $H=0$ T (solid lines) and $H=0.2$ T (open circles). Ferromagnetic ordering temperatures, T_c 's, of 159, 156, and 104 K for the SC, AG, and Q specimens, respectively, were estimated by fitting $M(T)$ to the Curie-Weiss law. (b) Hysteresis loops at 2 K for three types of $\text{Fe}_{0.25}\text{TaS}_2$ crystals, showing high coercivities of 2.7 T (SC), 4.0 T (AG), and 7 T (Q). $M(H)$ curves in H along and perpendicular to the c axis indicate a high magnetic anisotropy in $\text{Fe}_{0.25}\text{TaS}_2$.

Fig. 2: (Colour on-line) Electron diffraction patterns in reciprocal space and their intensity profiles at room temperature in the Q (a, a') and SC (b, b') specimens, respectively. The electron incidence is parallel to $[011]$ (a) and $[001]$ (b) zone axes, respectively. The profiles of (a') and (b') were scanned along $01\bar{1}-1\bar{1}1$ line in (a) and $010-1\bar{1}0$ line in (b), respectively. (c) Schematics of Fe ionic order in real space. Large circles and lines denote the 2×2 superlattice, and small circles and dashed lines represent the $\sqrt{3} \times \sqrt{3}$ superlattice.

Fig. 3: (Colour on-line) Dark-field TEM images taken with superlattice peaks for the Q (a), AG (b) and SC (c) specimens. For (a), a $(1/3, 1/3, 0)$ diffusive superlattice peak with electron incidence along $[011]$ is used, and a $(1/2, 0, 0)$ superlattice peak with the beam incidence direction of $[001]$ is used for (b) and (c). MFM images of the (d) Q [77.5 K, 0 T, and 2 Hz], (e) AG [6 K, 0 T, and 3 Hz], and (f) SC [60 K, 0.03 T, and 59 Hz] specimens.

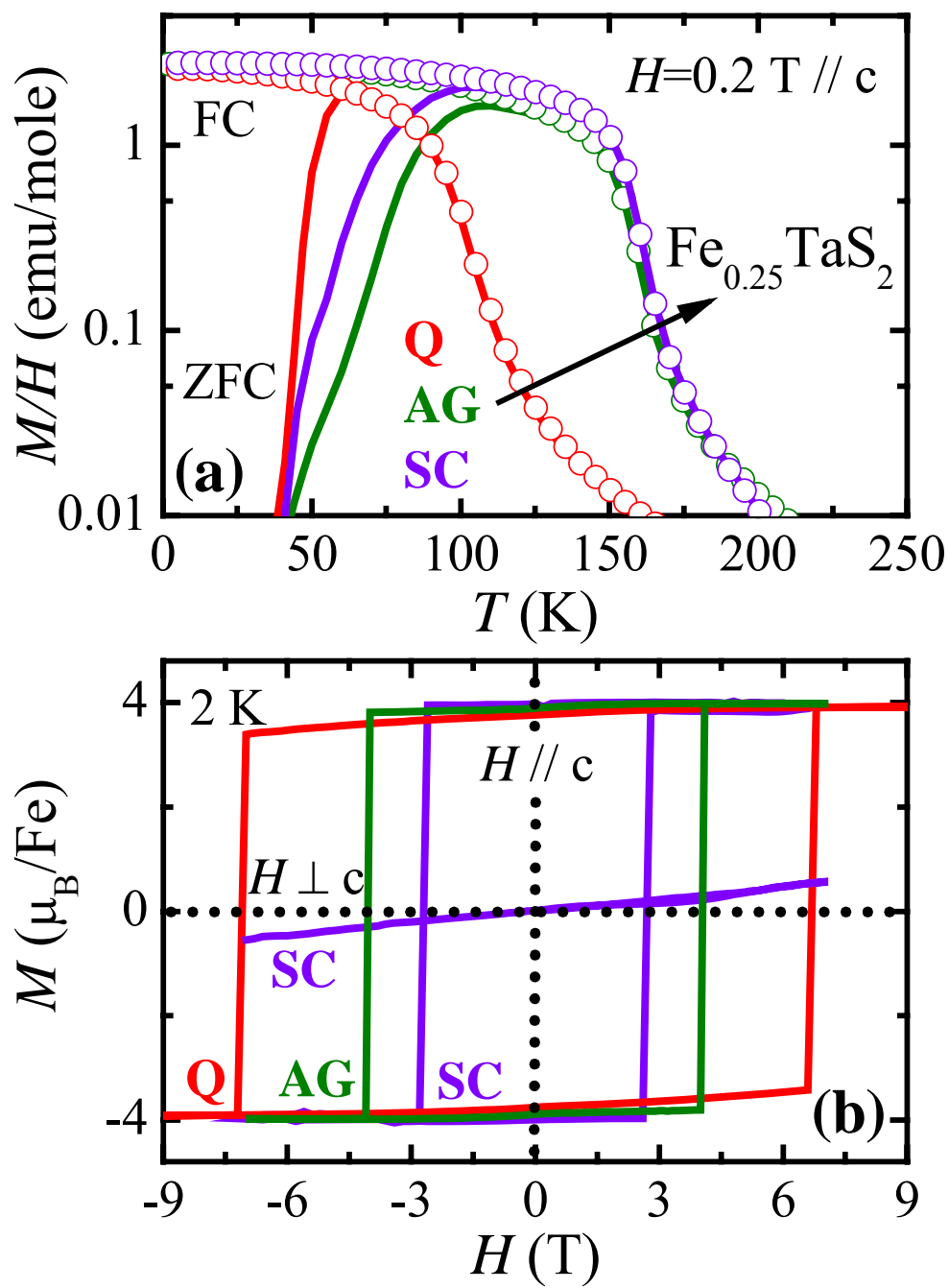
Ferromagnetic domain size increases systematically when superlattice domains are enlarged by thermal treatment.

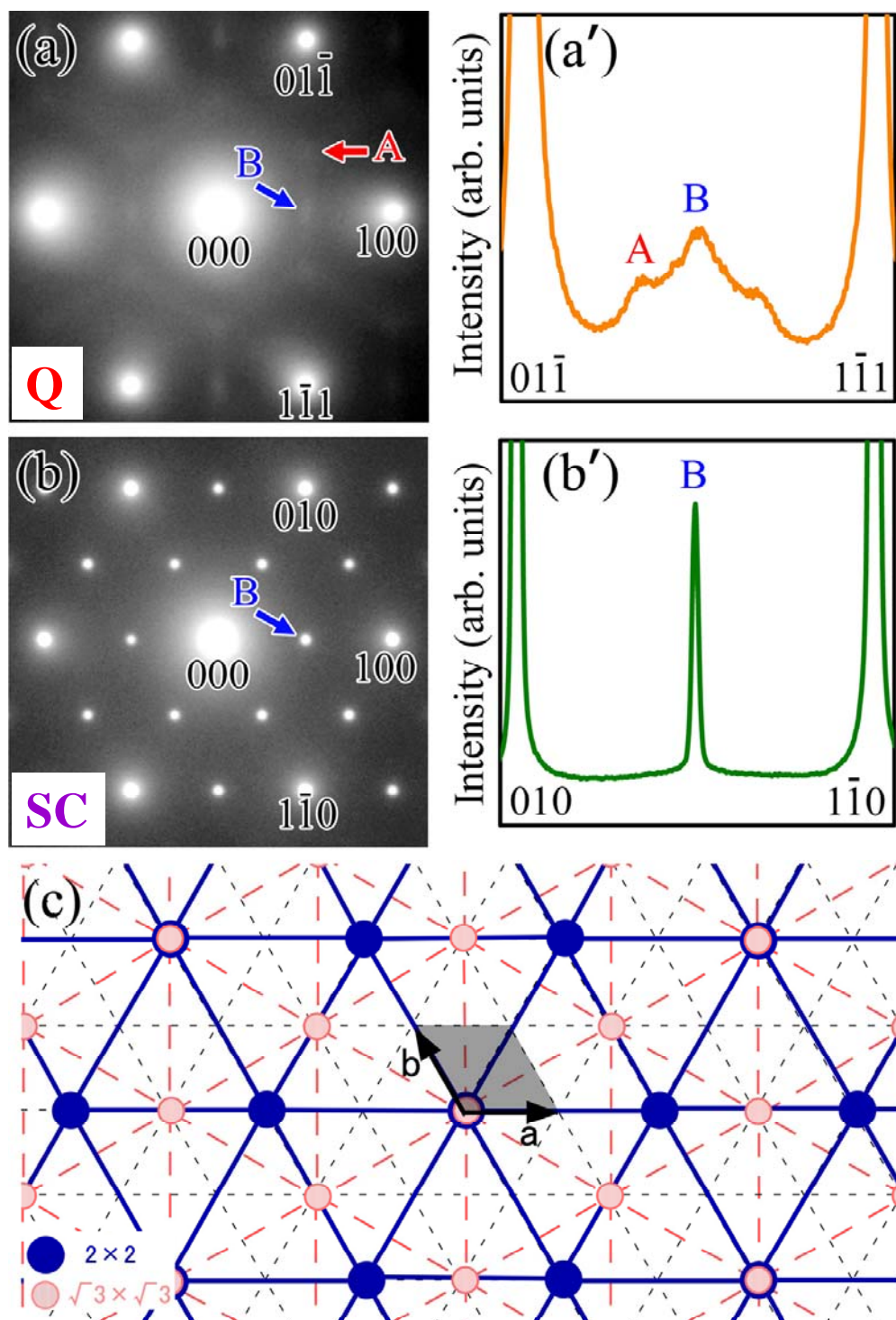
Fig. 4: (Colour on-line) (a) Magnetization vs. magnetic field (H/c) for the Q crystal at various temperatures (2-150 K). (b) T dependence of magnetization measured upon warming in various magnetic fields ($H^*=0.02, 0.2, 2$ and 7 T) after zero-field cooling in linear scale. Inset: T -dependent magnetic coercivity (closed circles) and H^* vs. T^* (open squares, T^* defined as T for the maximum slope of $M(T)$ in each H^*) for the Q crystal.

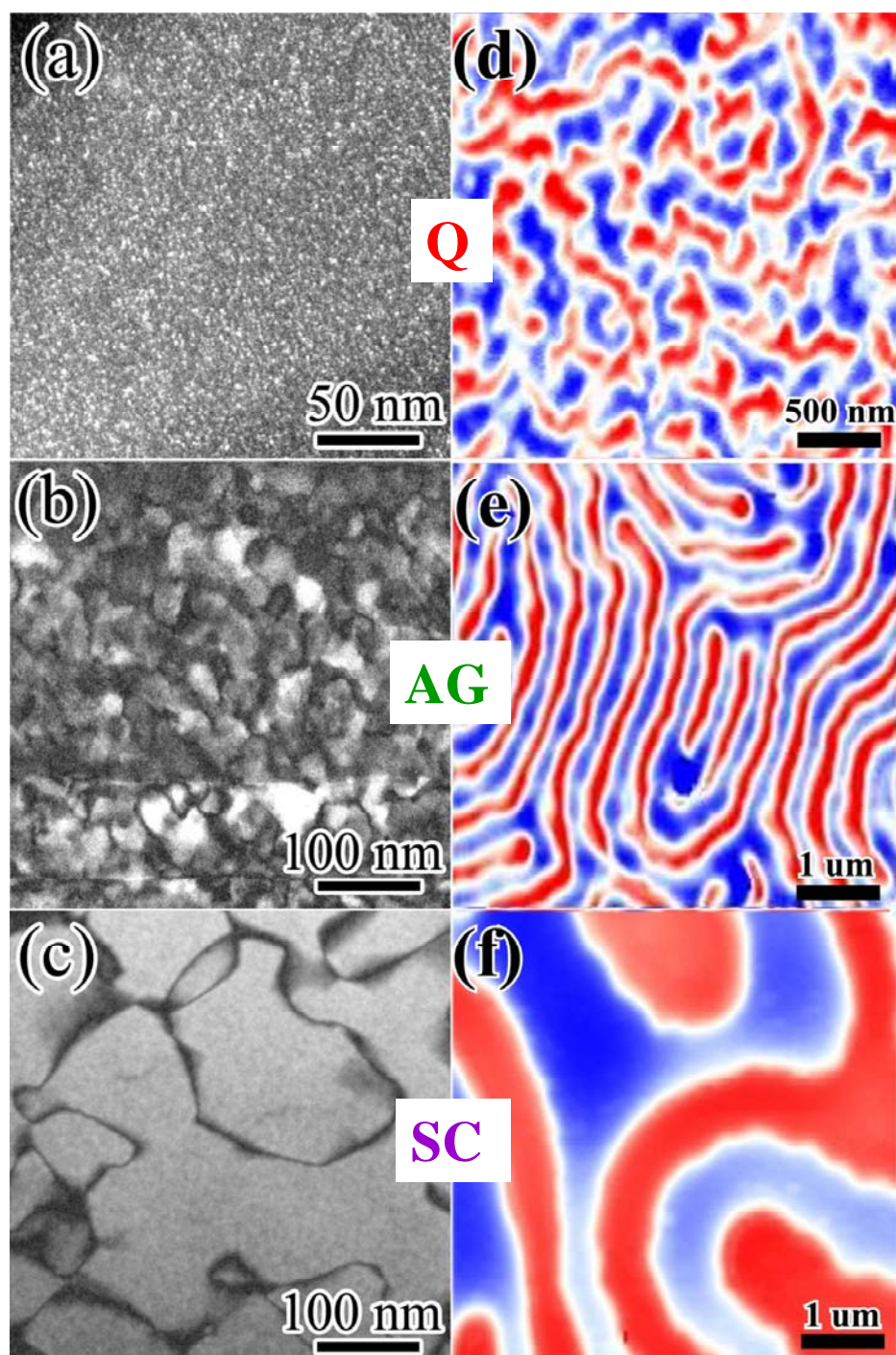
REFERENCES

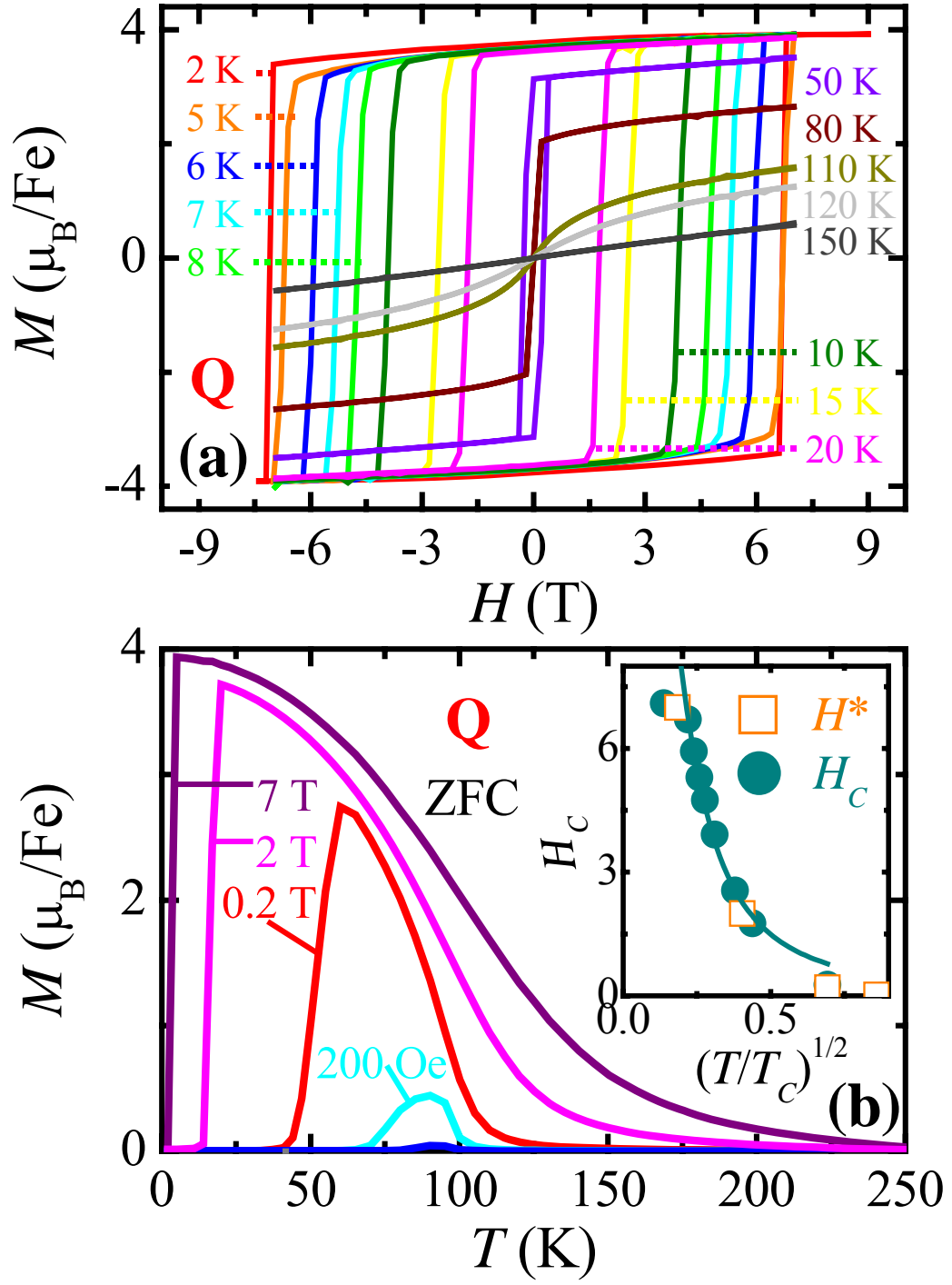
- [1] Chikazumi S., *Physics of Ferromagnetism*, (Oxford University Press, New York) 1997.
- [2] Livingston J. D., *J. Appl. Phys.*, **52** (1981) 2544.
- [3] Darby N. and Issac E., *IEEE Trans. Magn.*, **MAG-10** (1974) 259.
- [4] McCurrie R. A., *Ferromagnetic Materials*, (Academic Press, New York) 1994.
- [5] De Campos M. F., Landgraf F. J. G., Saito N. H., Romero S. A., Neiva A. C. and Missel F. P., *J. Appl. Phys.* **84** (1998) 368.
- [6] Zeng H., Li J., Liu J. P., Wang Z. L. and Sun S., *Nature* **420** (2002) 395.
- [7] Eibschütz M., Mahajan S., DiSalvo F. J., Hull G. W. and Waszczak J. V., *J. Appl. Phys.* **52**, (1981) 2098.
- [8] Narita H., Ikuta H., Hinode H., Uchida T., Ohtani T. and Wakihara M. J., *Solid State Chem.* **108** (1994) 148.

- [9] Le Blanc-Soreau A., Rouxel J., Gardette M.-F. and Gorochov O., *Mater. Res. Bull.* **11**, (1976) 1061.
- [10] Dai Z., Xue Q., Gong Y., Slough C. G. and Coleman R. V., *Phys. Rev. B* **48** (1993) 14 543.
- [11] Morosan E., Zandbergen H. W., Li L., Lee M., Checkelsky J. G., Heinrich M., Siegrist T., Ong N. P. and Cava R. J., *Phys. Rev. B* **75** (2007) 144401.
- [12] Senchuk A., Kunkel H. P., Roshko R. M., Viddal C., Wei L., Williams G. and Zhou X. Z., *Eur. Phys. J. B* **37** (2004) 285.
- [13] Davies J. E., Hellwig O., Fullerton E. E., Denbeaux G., Kortright J. B. and Liu K., *Phys. Rev. B* **70** (2004) 224434.
- [14] Suzuki Y., Sarachik M. P., Chudnovsky E. M., McHugh S., Gonzalez-Rubio R., Avraham N., Myasoedov Y., Zeldov E., Shtrikman H., Chakov N. E. and Christou G., *Phys. Rev. Lett.* **95** (2005) 147201.
- [15] Checkelsky J. G., Lee M., Morosan E., Cava R. J. and Ong N. P., *Phys. Rev. B* **77** (2008) 014433.
- [16] Hilzinger H. R., *Appl. Phys. A* **12** (1977) 253.
- [17] Zijlstra H. and Haanstra H. B., *J. Appl. Phys.* **37** (1966) 2853.
- [18] Asaka T., Yu X. Z., Tomioka Y., Kaneko Y., Nagai T., Kimoto K., Ishizuka K., Tokura Y. and Matsui Y., *Phys. Rev. B* **75** (2007) 184440.
- [19] Egami T., *Phys. Status Solidi A* **19** (1973) 747: **20** (1973) 157.
- [20] Oesterreicher H., Parker F. T. and Misroch M., *Phys. Rev. B* **18** (1978) 480.
- [21] Parker F. T. and Oesterreicher H., *Phys. Status Solidi A* **75** (1983) 273.

FIG. 1 Y. J. Choi *et al.*

FIG. 2 Y. J. Choi *et al.*

FIG. 3 Y. J. Choi *et al.*

FIG. 4 Y. J. Choi *et al.*

Curriculum Vitae

YOUNG JAI CHOI

Education

- 2002-2009 Ph.D. Condensed Matter Physics
Rutgers, the State University of New Jersey, New Brunswick, NJ
- 1999-2001 M.S. Physics
Yonsei University, Seoul, Korea
- 1993-1999 B.S. Physics
Yonsei University, Seoul, Korea

Positions Held

- 2005-2009 Graduate Assistant
Rutgers University Physics Department
- 2002-2005 Teaching Assistant
Rutgers University Physics Department
- 1999-2001 Teaching Assistant
Yonsei University Physics Department

Award

Iris Ovshinsky Student Travel Award for Material Physics (APS), 2009

Invited Talk

Ferroelectric Magnets: a Conical Spiral and an Ising Chain.
American Physical Society March meeting, Pittsburgh PA, March 2009.

Publications

1. Order by Disorder in the Ising Chain Magnet $\text{Ca}_3\text{Co}_{2-x}\text{Mn}_x\text{O}_6$.
V. Kiryukhin, S. Lee, W. Ratcliff II, H. T. Yi, Y. J. Choi, and S-W. Cheong,
In preparation.
2. Ising Pancake Domains and Memory Effect in LuFe_2O_4 .
S. Park, Y. J. Choi, C. L. Zhang, S-W. Cheong, and Weida Wu,
In preparation.

3. Electric Reversal of Spin Handedness in CoCr_2O_4 Observed by Soft X-ray Scattering.
J. Okamoto, D. J. Huang, C.-Y. Mou, H. H. Wu, K. S. Chao, S. L. Cheng, H.- J. Lin,
Y. J. Choi, S-W. Cheong, M. van Veenendaal, T. A. Kaplan, and C. T. Chen,
In preparation.
4. Giant Magnetic Coercivity and Ionic Superlattice Nano-domains in $\text{Fe}_{0.25}\text{TaS}_2$.
Y. J. Choi, S.B. Kim, T. Asada, S. Park, Weida Wu, Y. Horibe and S-W. Cheong,
Submitted to *Europhysics Letters* (2009).
5. Switchable Ferroelectric Diode and Photovoltaic Effect in BiFeO_3 .
T. Choi, S. Lee, Y. J. Choi, V. Kiryukhin, and S-W. Cheong,
Science **324**, 63 (2009).
6. Thermally or Magnetically induced Polarization Reversal in the Multiferroic CoCr_2O_4 .
Y. J. Choi, J. Okamoto, D. J. Huang, K.S. Chao, H. J. Lin, C. T. Chen,
M. van Veenendaal, T. A. Kaplan, and S-W. Cheong,
Phys. Rev. Lett. **102**(6), 067601 (2009).
7. 3:1 Magnetization Plateau and Suppression of Ferroelectric Polarization in an Ising
Chain Multiferroic.
Y. J. Jo, S. Lee, E. S. Choi, H.T. Yi, W. Ratcliff II, Y. J. Choi, V. Kiryukhin,
S-W. Cheong, and L. Balicas,
Phys. Rev. B **79**(1), 012407 (2009).
8. Origin of Electromagnon Excitations in RMnO_3 .
R. Valdés Aguilar, M. Mostovoy, A. B. Sushkov, C. L. Zhang, Y. J. Choi,
S-W. Cheong , and H. D. Drew, ,
Phys. Rev. Lett. **102**(4), 047203 (2009).
9. Pancakelike Ising Domains and Giant Magnetic Coercivity in Ferrimagnetic
 LuFe_2O_4 .
Weida Wu, V. Kiryukhin, H.-J. Noh, K.-T. Ko, J.-H. Park, W. Ratcliff II,
P.A. Sharma, N. Harrison, Y. J. Choi, Y. Horibe, S. Lee, C. L. Zhang, and
S-W. Cheong,
Phys. Rev. Lett. **101**(13), 137203 (2008).
10. Multiferroicity in the Spin-1/2 Quantum matter of LiCu_2O_2 .
A. Rusydi, I. Mahns, S. Müller, M. Rübhausen, S. Park, Y. J. Choi, C .L. Zhang,
S-W. Cheong, S.Smadici, P. Abbamonte, M.V. Zimmermann, and G.A. Sawatzky,
Appl. Phys. Lett. **92**(26), 262506 (2008).
11. Multiferroicity in the Square-Lattice Antiferromagnet of $\text{Ba}_2\text{CoGe}_2\text{O}_7$.
H. T. Yi, Y. J. Choi, S. Lee, and S-W. Cheong,
Appl. Phys. Lett. **92**(21), 212904 (2008).
12. Spin Phonon Coupling in Frustrated Magnet CdCr_2O_4 .
R. Valdés Aguilar, A. B. Sushkov, Y. J. Choi , S-W. Cheong, and H. D. Drew,

- Phys. Rev. B* **77**, 092412 (2008).
13. Ferroelectricity in an Ising Chain Magnet.
Y. J. Choi, H. T. Yi, S. Lee, Q. Huang, V. Kiryukhin, and S-W. Cheong,
Phys. Rev. Lett. **100**, 047601 (2008)
 14. Magnetic Nanocheckerboards with Tunable Sizes in the Mn-doped CoFe_2O_4 .
 C. L. Zhang, C.M. Tseng, C.H. Chen, S. Yeo, Y. J. Choi, and S-W. Cheong,
Appl. Phys. Lett. **91**(23), 233110 (2007).
 15. Colossal Magnon-phonon Coupling in Multiferroic $\text{Eu}_{0.75}\text{Y}_{0.25}\text{MnO}_3$.
 R. Valdés Aguilar, A. B. Sushkov, C. L. Zhang, Y. J. Choi, S-W. Cheong,
 and H. D. Drew,
Phys. Rev. B **76**, 060404(R) (2007).
 16. Coercivity and Nanostructure in Magnetic Spinel $\text{Mg}(\text{Mn,Fe})_2\text{O}_4$.
 C. L. Zhang, S. Yeo, Y. Horibe, Y. J. Choi, S. Guha, M. Croft, and S-W. Cheong,
Appl. Phys. Lett. **90**(13), 133123 (2007).
 17. Ferroelectricity in an $S=1/2$ Chain Cuprate.
 S. Park, Y. J. Choi, C. L. Zhang, and S-W. Cheong,
Phys. Rev. Lett. **98**, 057601 (2007).
 18. Enhanced Superconducting T_C in the Immiscible Mixture of $\text{La}_{1.85}\text{Sr}_{0.15}\text{CuO}_4$ and
 Antiferromagnetic-Insulating $\text{Lu}_2\text{Cu}_2\text{O}_5$.
 S. Park, C. L. Zhang, N. Lee, Y. J. Choi, S. Guha, and S-W. Cheong,
 Submitted to *Phys. Rev. Lett.*